

Particle-size segregation and rheology coupling in dense granular flows.

Présentée le 25 mars 2021

Faculté de l'environnement naturel, architectural et construit
Laboratoire d'hydraulique environnementale
Programme doctoral en mécanique

pour l'obtention du grade de Docteur ès Sciences

par

Tomás Alfredo TREWHELA PALACIOS

Acceptée sur proposition du jury

Prof. F. Gallaire, président du jury
Prof. C. Ancey, directeur de thèse
Prof. J. M. N. T. Gray, rapporteur
Dr N. Vriend, rapporteuse
Prof. B. Lecampion, rapporteur

INSTRUCCIONES PARA LEER UNA TESIS

Tome aire, respire, camine hacia el estante, saque la tesis. Piense en lo que hizo el autor para terminarla, póngase gafas, en caso de requerirlas, busque un sillón verde y tome asiento.

Deje la tesis a un costado, párese y apague la radio, la televisión, y piense de nuevo en el autor. ¿Quién era? ¿Cómo vestía? ¿Le gustaba el café o la cerveza?

Prepárese un café y vuelva a la silla reclinable, esa que le gusta, apoye sus pies y deje a un costado las alpargatas.

Hace calor, ¿cierto? Aún tiene que bajar las escaleras para lavar la ropa, pero

deje eso para más rato, tome la tesis. Lea el nombre del autor y el título, piense sobre quién decidió el título y quién decidió ese nombre para el autor, reflexione que no es de su gusto, pero reconozca que su nombre tampoco es trascendente, y usted ni siquiera tiene título.

Sostenga la tesis por el lomo, firme, y ábrala, sienta el olor a nuevo, ¿le agrada? ¿A quién no?

Observe el número de página, avance y vea el total de páginas, ¿valdrá su tiempo? Retroceda rápidamente al resumen, léalo. Para eso, atraviese la página verticalmente, de arriba a abajo, ¿o al revés? No importa, con tal que lo repita un par de veces, capturando las palabras que considere relevantes, o mejor aún, los tecnicismos. Así al menos puede aparentar ser interesante en su próxima tertulia, ¿no le parece?

Cierre la tesis, déjela sobre la silla, póngase las alpargatas, párese y baje las escaleras, lave la ropa en agua fría, ¿con centrifugado o en programa delicado? Vea la hora.

Suba las escaleras, levante la tesis de la silla, recuéstese en el sillón verde, no se saque las alpargatas. Ojee la tesis y repita el proceso del resumen, ¿lo recuerda? Bien, hágalo, pero esta vez en páginas aleatorias, ¿no entiende? Busque en específico donde se explica eso que no logra entender. Salte de página en página buscando el sentido, como en esa novela, ¿cómo se llamaba esa novela? Esa en la que dedican un capítulo entero a divagar sobre jazz.

Cierre la tesis, párese, deje la tesis sobre la silla y camine hacia la radio, préndala y busque una estación de jazz. ¿Recuerda las palabras que leyó en la tesis?

Piense que son papeles desparramados en el piso, ¿eso le recuerda un urinario? Vaya al baño.

¿Será la hora? Baje las escaleras y retire la ropa de la lavadora, cuélguela en el colgador del cuarto, que le de el sol de la ventana.

Es todavía temprano para salir a caminar.

Suba las escaleras, tome la tesis y vuélvala a meter en el estante.

Duración media de la lectura de una tesis: lo que toma un tren entre París y Marsella.

“Andábamos sin buscarnos, pero sabiendo que andábamos para encontrarnos”
— Julio Cortázar

Para Lucía

Acknowledgements

First and foremost, I have to thank my wife and partner Lucía. Not only was she willing to join and support me in this journey, but also made a journey of her own. She was also able to chase her dreams and do what she wanted here in Switzerland, and for that inner strength, I admire her. No matter the odds, the faults or mistakes, the sweet and sour, we have always been there for each other. Lucía, this work is yours as well, and these four years have been ours to keep. I love you.

Nothing would have been possible without the constant trust and support of *El Jefe*, Christophe Ancey. To think that everything started from a naive mail where I asked him for data, speaks a lot about on the bet he took with me. From the very beginning, he taught me the importance of writing, teaching and critical-thinking in the role of a researcher. Christophe, thanks to the occasional extra work or additional responsibilities, you have prepared me to become an independent researcher, and our discussions have made me a more realistic and insightful person. For all that and the opportunity to do a PhD in the LHE, I'll be grateful for life. Hasta la victoria, siempre.

An important part, and the most relevant contribution of this thesis was done in collaboration with Nico Gray. Nico, I very much enjoyed your visits, the scientific discussions and the after-lunch coffee. I really admire the dedication you put into your craft. Thank you very much for all the support and time you dedicated to me during these four years. I truly hope we can continue to collaborate together.

This thesis would have never been finished without the vital help of Michel Teuscher and Joël Stoudmann. Thank you both for the perseverance on the conveyor belt and the patience with our crazy ideas. Joël, good luck in your new project.

Certainly, the fact that I enjoyed so much my stay at LHE is due to Barbara, Bertil, Bernard, Blaise, Bob, Daniel, Étienne, Gauthier, Ivan, Kasper and Zhenzhu. Barbara thank you for your support and all the help with the bureaucracy, but most important, for all the lunch conversations we shared. Bertil, thanks to you I could not finish this thesis earlier. It's a joke, you are a great friend and your weekly or daily (?) visits were a needed distraction. Bernard, thanks for the laughs and oversimplified discussions. Blaise, I really appreciated those coffee conversations with Pan Pam, you made me feel welcomed to the lab. Bob, LHE's phoenix

Acknowledgements

mecano, without you nothing works in LHE and not only the experiments. Thank you for believing in the CODEV project and in me, I hope that helped you to value the importance of your work. I will always remember the baby-foot, the ping pong games and of course, the fieldwork in Zinal (spécialement la raclette d'après) ¡Ánda a la cancha Gordo! Gracias a D10S que estabas en el laboratorio, no sabes cuanto me ayudó tener a alguien que hablara español al principio. Perdón por no dejarte terminar a tiempo la tesis. Étienne, I will fondly remember our eternal discussions on science and life. Gato, the joy of the lab. For a long time I felt you were the only I could discuss my thesis with. Despite the PIV cold war, you know I'll remember you for your other 'side' projects and your persistence. Ivanello, il buono fratello, thank you for being a great peer and collaborator, for doing better, your pragmatism, and for setting the pace of our cordata. Kasper, thank you so much for your help throughout these four years, without your work I would have never been able to do mine. Z, the other joy of the lab. Thank you for who you are, the laughs and your positive energy, despite the fact I was sometimes harsh at you, I'm sorry for that. Gracias a todos por tanto, perdón por tan poco. Merci à tous pour tout, désolé pour si peu. Thank you for everything, sorry for so little.

Not everything at EPFL was work, or at least I want to think it was not. EPFL gave me the opportunity to meet many wonderful people, and some of them gave me the gift of their friendship. To my friends, Anh Chi, Arnaud, Åsa, Conny, Dani, Edu, Hugo, Lupi, Mapi, Marta, Matt, Mauricio, Nela, Niels, Oscar, Robert, Solenne and Xime: your friendship has been invaluable for me and Lucía, and my stay here has been awesome because of you guys, I'll cherish every laugh and moment spent together. I hope you can count on me as much as I have counted on you through these years. To the climbers, thank you as well for many relaxed evenings, flash bros. An acknowledgement to Poulet Express and the Pouletiers for our monthly Poupoupoulet tradition, we all know it's the sauce.

Ana María, muchas gracias por tu amistad, tu ayuda y apoyo. Más que una amiga, eres nuestra familia en Suiza y por eso estamos muy agradecidos. Te queremos mucho.

Quiero agradecer a mi familia y a mis amigos en Chile, especialmente a quienes nos visitaron. A mis padres, suegros, hermanas, sobrinos y cuñados, muchas gracias por el apoyo constante, el cariño y la preocupación. A la distancia, les mando un abrazo, los quiero mucho y más temprano que tarde nos volveremos a ver.

For an important part of these four years I suffered from non-work related anxiety and panic attacks. Even if they created a crippling effect in my life for several months, I had the support of many people around me, EPFL, Christophe, my family and friends. I only learnt to deal with it once I spoke about it. You never know who will read these pages so if you are dealing with mental issues, please look for support and help. As somber as it may look like, life can be better. As desperate you may feel, there is always a solution.

There are plenty of people that helped me during these four years, perhaps without real-

izing. The Federal Commission for Scholarships for Foreign Students, the Swiss National Science Foundation, and Conicyt, now ANID, financed this thesis and my stay in Switzerland. In particular, I am deeply grateful to Karin Juillerat, Sylvie Clavel and the Swiss scholars of 2016. The fact I did not suffer a cultural shock, is in part, thanks to them. Thanks to the Language Center of EPFL I had the opportunity to learn French and German, an experience that has deeply enriched me in a personal level. Probably they will not read these pages but, Bernarda, Corinne, Emmanuel, Marido and Vincent, merci pour votre patience et dévouement, Danke schön.

Finally, thanks to François Gallaire, Nathalie Vriend, Brice Lecampion and Nico Gray for examining this thesis and being part of the jury. Your comments were very valuable to me. In particular, thanks François for always showing interest in my work and doctoral well being.

Lausanne, November 6, 2020

Tomás Trehwela, T. T.

Abstract

Dense granular flows —debris or pyroclastic flows, avalanches, granular flows in heaps, silos or rotating drums—are ubiquitous to many natural and industrial processes. Their grain composition is often polydisperse, with particles differing in shape, size or density. In a phenomenon called particle-size segregation, grains of different sizes are rearranged by the very same mechanical forcing that generates the granular flow in the first place. If the flow's rheology is determined by grain characteristics and grain-grain interactions, a grain rearrangement should change the flow's rheology. Although recent constitutive relations for dense granular flows and size segregation models are able to describe well their respective processes, the interplay between rheology and particle-size segregation remains poorly understood. In this dissertation, I present an experimental study that aims to describe the coupling between rheology and particle-size segregation in dense granular flows. To address this objective, experiments in three experimental setups were carried out: (i) a two-dimensional oscillating shear cell, (ii) a three-dimensional oscillating shear box, and (iii) a three-dimensional conveyor belt flume. In these three configurations, I focused on the experimental determination of bulk species composition, segregation rates, velocity fields and the strain-rate tensor invariants. For that, the Refractive Index Matching (RIM) and Particle Tracking Velocimetry (PTV) techniques were intensively applied. In the two-dimensional shear cell, the rate and mechanism by which a large particle (intruder) segregated were found to be determined by the particles' size ratio, its rotation, and the strain rate around it. A scaling law for the segregation flux function was determined from the three-dimensional shear box single-intruder experiments. Four key observations were made: the segregation rate scaled; (i) linearly to the shear rate, for small and large intruders; (ii) linearly to the size ratio for a large intruder; and (iii) quadratically to size ratio for a small intruder. Finally, (iv) all the intruders' trajectories were well-fitted by a quadratic law, a sign of a pressure-dependent segregation rate. For the mono- and bidisperse stationary granular avalanches in the conveyor belt, I found two flow regions: a bulged-convective front and a well-arranged layered tail. Independently of concentration, the time-averaged velocity profiles were found to be Bagnold-like and segregation rate was found to be highest at the front, where dilation and shear rate values were also high. All these experimental results described a strong coupling between rheology and particle-size segregation, and ultimately provided a segregation rate dependence on normal stresses, shear rate and size ratio.

Zusammenfassung

Dichte körnige Strömungen —Trümmer oder pyroklastische Strömungen, Lawinen, körnige Strömungen in Haufen, Silos oder rotierenden Fässern—sind in vielen natürlichen und industriellen Prozessen allgegenwärtig. Ihre Kornzusammensetzung ist oft polydispers, mit unterschiedlicher Form, Größe oder Dichte der Partikel. In einem Phänomen, bezeichnet als Partikelgrößentrennung, werden Körner unterschiedlicher Größe durch denselben mechanischen Antrieb neu angeordnet, der vor allem den körnigen Fluss erzeugt. Wenn die Rheologie durch Kornmerkmale und Korn-Korn-Wechselwirkungen bestimmt wird, sollte eine Kornumlagerung die Rheologie ändern. Obwohl die jüngsten Materialmodelle für dichte körnige Strömungen und Größentrennungsmodelle ihre jeweiligen Prozesse gut beschreiben können, ist es noch wenig bekannt, wie Rheologie und Partikelgrößentrennung zusammen wirken. In dieser Dissertation stelle ich eine experimentelle Studie vor, die die Kopplung zwischen Rheologie und Partikelgrössentrennung in dichten körnigen Strömungen beschreibt. Dazu, wurden drei verschiedene Experimente durchgeführt: (i) eine zweidimensionale oszillierende Scherzelle, (ii) eine dreidimensionale oszillierende Scherbox und (iii) ein dreidimensionaler Förderbandkanal. Diese drei Versuchen konzentrierten sich auf die experimentelle Bestimmung der Zusammensetzung von Massenarten, der Trennungsraten, der Geschwindigkeitsfelder und der Invarianten der Dehnungsrate. Hierfür wurden die Refractive Index Matching (RIM) und Particle Tracking Velocimetry (PTV) angewendet. In der zweidimensionalen Scherzelle wurde die Geschwindigkeit und der Mechanismus, durch die sich ein großes Teilchen (Eindringling) trennte, durch das Größenverhältnis der Teilchen, seine Rotation und die Dehnungsgeschwindigkeit um sie herum bestimmt. Ein Skalierungsgesetz für die Trennungsflussfunktion wurde aus den dreidimensionalen Scherbox-Einzeleindringling-Experimenten bestimmt. Es wurden vier wichtige Beobachtungen gemacht, die Trennungsrate normierte: (i) linear zur Schergeschwindigkeit für kleine und große Eindringlinge; (ii) linear zum Größenverhältnis für einen großen Eindringling; und (iii) quadratisches Verhältnis zur Größe für einen kleinen Eindringling. Schließlich (iv) waren alle Flugbahnen der Eindringlinge durch ein quadratisches Gesetz gut beschrieben, ein Zeichen für eine druckabhängige Entmischungsrate. Für die stationären körnigen Lawinen im Förderband fanden wir zwei Strömungsbereiche: eine gewölbte-konvektive Front und einen übersichtlichen Schichtschwanz. Unabhängig von der Konzentration waren die zeitlich gemittelten Geschwindigkeitsprofile Bagnold-ähnlich und die Entmischungsrate an der Vorderseite am höchsten, wo auch die Werte für Dilatanz und Schergeschwindigkeit hoch waren. Alle Resultate beschreiben eine starke Kopplung zwischen Rheologie und Partikelgrößentrennung und zeigen letztendlich

Zusammenfassung

eine Abhängigkeit der Trennungsrate von normalen Spannungen, Schergeschwindigkeit und Größenverhältnissen.

Résumé

Les écoulements granulaires denses —laves torrentielles ou pyroclastiques, les avalanches, les écoulements granulaires en tas, silos ou tambours—se retrouvent dans de nombreux processus naturels et industriels. Ils sont composés de particules qui diffèrent par la forme, la taille ou la masse volumique. Le phénomène appelé ségrégation granulaire correspond à une situation où des grains de différentes tailles se séparent, et ceux de taille similaire se regroupent. Parmi les questions ouvertes sur la rhéologie des écoulements granulaires, il y a l'interaction entre dynamique des écoulements et ségrégation granulaire. Dans ma thèse, je présente une étude expérimentale pour comprendre la relation entre rhéologie et ségrégation granulaire dans des écoulements granulaires denses. Pour cela, j'ai mené des expériences dans trois configurations expérimentales : (i) une cellule de cisaillement oscillatoire bidimensionnelle, (ii) une cellule de cisaillement oscillatoire tridimensionnelle, et (iii) un tapis roulant tridimensionnel. Dans ces trois dispositifs, je me suis concentré sur la détermination expérimentale de la composition de l'écoulement, des taux de ségrégation, des champs de vitesse et des invariants du tenseur des taux de déformation. Pour les expériences, j'ai utilisé de manière intensive les méthodes dites « Refractive Index Matching » (RIM) et « Particle Tracking Velocimetry » (PTV). Dans la cellule de cisaillement bidimensionnelle, j'ai étudié comment une grosse particule (intrus) se déplaçait dans un milieu composé de petites particules de même taille. J'ai montré que la vitesse de ségrégation dépendait du rapport de taille des particules, leur rotation et la déformation autour d'elles. J'ai développé une fonction empirique qui détermine la vitesse de ségrégation d'un intrus dans la boîte de cisaillement tridimensionnelle. Quatre observations clés en ont été tirées : (i) la vitesse de ségrégation est directement proportionnelle au taux de cisaillement (que l'intrus soit grand ou petit) ; (ii) elle dépendait du rapport de tailles entre intrus et milieu environnant ; (iii) elle se présentait comme une fonction quadratique du rapport de tailles lorsque les intrus étaient de petit diamètre ; et (iv) toutes les trajectoires des intrus sont cohérentes avec une loi quadratique de ségrégation. Ce résultat est important parce que cela montre que la ségrégation dépend de la pression locale. Pour les avalanches granulaires stationnaires générées sur le tapis roulant, on a trouvé deux régions d'écoulement : un front d'écoulement, présentant une forte courbure de la surface libre et qui est dominé par un transport convectif, et une queue d'écoulement, qui se caractérise par des couches compactes. Quelle que soit la concentration, les profils de vitesses moyennées dans le temps sont de type Bagnold, et la vitesse de ségrégation est la plus élevée au niveau du front, où la dilatance et le cisaillement de l'écoulement sont également élevés. Tous ces résultats expérimentaux décrivent un couplage fort entre rhéologie et ségrégation granulaire, et fournissent finalement

Résumé

une fonction de la vitesse de ségrégation qui dépend des contraintes normales, du taux de cisaillement, et du rapport de tailles des particules.

Riassunto

Flussi granulari densi —flussi detritici o piroclastici, valanghe, flussi granulari in pile, silos o fusti—si trovano in molti processi naturali e industriali. La loro matrice granulare è spesso polidispersa, con particelle che differiscono per forma, dimensione o densità. In un fenomeno chiamato segregazione granulare, grani di diverse dimensioni vengono riorganizzati dalla stessa sollecitazione che genera il flusso in prima istanza. Sebbene i recenti progressi nella reologia e nella segregazione abbiano descritto con successo i rispettivi processi, l'interazione tra i due rimane scarsamente compresa. Questa tesi presenta uno studio sperimentale volto a descrivere la relazione tra reologia e segregazione granulare in flussi granulari densi. Per raggiungere questo obiettivo, si sono condotti esperimenti utilizzando tre diverse attrezzature: (i) una cella di taglio oscillatoria bidimensionale, (ii) una cella di taglio oscillatoria tridimensionale e (iii) un nastro trasportatore tridimensionale. In queste tre installazioni, lo studio è stato focalizzato sulla determinazione sperimentale della composizione del flusso, velocità di segregazione, campi di velocità e invarianti del tensore di deformazione. Per gli esperimenti, sono stati utilizzati i metodi Refractive Index Matching (RIM) e Particle Tracking Velocimetry (PTV). Gli esperimenti nella cella di taglio bidimensionale hanno evidenziato che la velocità e il meccanismo con cui viene segregata una singola grande particella grande (intruso) sono determinati dal rapporto tra i diametri delle particelle, dalla loro rotazione e dalla deformazione nel loro intorno. Una funzione per il tasso di segregazione è stata determinata studiando la segregazione dei singoli intrusi nella cella di taglio tridimensionale. Sono state fatte quattro osservazioni, il tasso di segregazione è direttamente proporzionale: (i) al tasso di cutoff, per piccoli e grandi intrusi; (ii) al rapporto tra i diametri (particellari) per grandi intrusi; e (iii) al quadrato il rapporto tra i diametri (particellari) per piccoli intrusi. Infine, (iv) tutte le traiettorie degli intrusi si adattano bene a una legge quadratica, un'indicazione che la segregazione dipende dalla pressione locale. Per le valanghe granulari stazionarie generate sul nastro trasportatore, abbiamo identificato due regioni di flusso: un fronte convettivo sorgente e un retro compatto e stratificato. Indipendentemente dalla concentrazione, i profili di velocità mediati nel tempo sono risultati di tipo Bagnoldiano e il tasso di segregazione è risultato essere il più elevato nella parte anteriore, dove anche la dilatanza del flusso e il taglio sono alti. Tutti questi risultati sperimentali hanno testimoniato una forte interazione tra reologia e segregazione granulare, e infine hanno fornito una funzione per la velocità di segregazione che dipende dalle sollecitazioni normali, dalla tasso di deformazione angolare e dal rapporto tra i diametri (particellari).

Resumen

Los flujos granulares densos —flujos detríticos o piroclásticos, avalanchas, flujos granulares en pilas, silos o tambores —se encuentran en muchos procesos naturales e industriales. Su matriz granular es a menudo polidispersa, con partículas que difieren en forma, tamaño o densidad. En un fenómeno llamado segregación granular, los granos de diferentes tamaños son reordenados por el mismo forzante que genera el flujo en primera instancia. Aun cuando avances recientes en reología y segregación han logrado describir exitosamente sus respectivos procesos, la interacción entre ambos sigue poco comprendida. En esta tesis, presento un estudio experimental que tiene como objetivo describir la relación entre reología y la segregación granular en flujos granulares densos. Para abordar este objetivo, llevé a cabo experimentos en tres configuraciones experimentales: (i) una celda bidimensional de cizalle oscilatorio, (ii) una celda tridimensional de cizalle oscilatorio y (iii) una cinta transportadora tridimensional. En estas tres instalaciones, me centré en la determinación experimental de la composición del flujo, las tasas de segregación, los campos de velocidad y los invariantes del tensor deformación. Para los experimentos, utilicé intensivamente los métodos Refractive Index Matching (RIM) y Particle Tracking Velocimetry (PTV). En la celda de cizalle bidimensional, determiné que la velocidad y el mecanismo con el cual una partícula grande (intruso) es segregada, estaban determinados por la razón de tamaño de las partículas, su rotación y la deformación a su alrededor. Se definió una función para la tasa de segregación a partir de intrusos segregando en la caja de cizalle tridimensional. Se hicieron cuatro observaciones, la tasa de segregación es directamente proporcional: (i) a la tasa de corte, para intrusos pequeños y grandes; (ii) a la razón de tamaño entre partículas para los intrusos grandes; y (iii) al cuadrado de la razón de tamaño para los intrusos pequeños. Finalmente, (iv) todas las trayectorias de los intrusos se ajustaron bien a una ley cuadrática, una indicación de que la segregación depende de la presión local. Para las avalanchas granulares estacionarias generadas en la cinta transportadora, observé dos claras regiones en el flujo: un frente abultado y convectivo, y una parte posterior compacta y ordenada en capas de partículas. Independientemente de la concentración, se determinó que los perfiles de velocidad promediados en el tiempo eran del tipo Bagnold y se encontró que la tasa de segregación era más elevada en el frente, donde la dilatación y el cizallamiento del flujo eran también altos. Todos estos resultados experimentales permitieron describir una fuerte interacción entre reología y segregación granular, y finalmente proporcionaron una función para la tasa de segregación que depende de los esfuerzos normales, la tasa de deformación angular y la razón de tamaño entre las partículas.

Contents

Acknowledgements	i
Abstract (English/Français/Deutsch/Italiano/Español)	v
List of Figures	xix
List of Tables	xxiii
1 Introduction	1
1.1 Motivation	1
1.2 The rheology of dense granular flows	4
1.3 Particle-size segregation	8
1.4 Experimental techniques and methods	12
1.5 Objectives and research contributions	14
1.6 Dissertation outline	16
2 Large particle segregation in sheared dense granular flows	17
2.1 Introduction	19
2.2 Methods	20
2.2.1 Image acquisition and particle tracking	22
2.2.2 Intruder rotation	22
2.2.3 Strain rate tensor invariants	23
2.3 Results	23
2.3.1 Vertical positions	23
2.3.2 Intruder rotation	26
2.3.3 Strain rate tensor invariants	29
2.3.4 Segregation mechanism	30
2.4 Conclusions	31
3 Scaling law for particle-size segregation in dense granular flows	37
3.1 Introduction	38
3.2 Bidisperse particle-size segregation	41
3.2.1 Governing equations	41
3.2.2 Segregation fluxes and velocities	42
3.3 Refractive index matched shear box experiments	44
	xv

3.3.1	Experimental apparatus	44
3.3.2	Refractive index matching, image acquisition and particle tracking . . .	46
3.3.3	Experimental data sets	48
3.4	Preliminary interpretation of the data	49
3.4.1	Dimensional analysis	49
3.4.2	Fundamental observations and resulting hypothesis	50
3.4.3	Effect of the interstitial fluid	52
3.4.4	Intruder trajectories	52
3.4.5	The role of particle diffusion	53
3.5	Large intruder experiments	54
3.5.1	Variable shear rate for the large intruders	54
3.5.2	Variable size ratio for the large intruders	56
3.5.3	Collapse of all the large intruder experiments	57
3.6	Small intruder experiments	58
3.6.1	Variable shear rate for the small intruders	58
3.6.2	Variable size ratio for the small intruders	61
3.6.3	Collapse of all the small intruder experiments	62
3.7	Simulation of van der Vaart <i>et al.</i> 's (2015) experiment	63
3.7.1	Summary of the equations and coefficients	63
3.7.2	Non-dimensionalization and numerical method	64
3.7.3	Asymmetric segregation flux functions	65
3.7.4	Large and small particle segregation velocities	66
3.7.5	Comparison to van der Vaart's (2015) experimental data	67
3.7.6	Properties of the steady-state solution	68
3.7.7	Exact steady-state solution for the case $\mathcal{C} = 0$	69
3.7.8	Steady-state comparison to van der Vaart's (2015) experiment	69
3.8	Conclusions	71
4	A conveyor belt setup to study granular avalanches	75
4.1	Introduction	76
4.2	Theoretical framework	78
4.2.1	Granular flow equations	78
4.2.2	Size segregation equations	79
4.2.3	Strain-rate tensor invariants	81
4.3	Materials and techniques	81
4.3.1	Refractive index match	81
4.3.2	Image acquisition	83
4.3.3	Particle tracking and coarse-graining	83
4.4	The conveyor belt experimental setup	83
4.5	Experimental dataset	85
4.5.1	Belt velocity	87
4.6	Results	88

4.6.1	Monodisperse experiments	88
4.6.2	Bidisperse experiments	90
4.7	Conclusions	93
5	Conclusions and outlook	97
5.1	Summary of this thesis	97
5.2	Future perspectives	99
5.2.1	Outcomes	99
5.2.2	Open challenges	100
A	Notes on experiments with restrained particle-size segregation	103
A.1	Absence of the kinetic sieving mechanism in two-dimensional experiments . .	103
A.2	Poly(methyl methacrylate) (PMMA) - Triton X-100 experiments	104
B	Annular shear cell setup	107
B.1	Conception	107
B.2	Construction	108
	Bibliography	111
	Curriculum Vitae	125

List of Figures

1.1	Examples of natural granular flows.	2
1.2	Segregation mechanisms: kinetic sieving and squeeze expulsion.	9
1.3	Asymmetric segregation flux functions and velocities.	11
1.4	Examples of the RIM technique usage.	13
2.1	Schematic diagram of the 2D shear cell setup.	21
2.2	Vertical position z as a function of time t for the intruders of $d_i = 10, 12, 18$ and 20 mm in the $d_m = 6$ mm medium experiments.	25
2.3	Normalized vertical position z/h as a function of normalized time t/t_f for all experiments and average vertical velocity $\bar{w}_i = h/t_f$ as a function of size ratio $1 - d_m/d_i$	26
2.4	Dot positions relative to the intruder's position.	27
2.5	Intruders' angular velocity Ω_i , vertical velocities w_i as a function of time t and probability of w_i given that Ω_i , $P(w_i \Omega_i)$	28
2.6	Time-averaged strain rate-tensor invariants: dilation I_{D_i} and shear rate II_{D_i} around the intruder's circumference ϕ_i	30
2.7	Schematic diagram of the segregation of a single large intruder.	32
2.8	Image sequence for the dilation mechanism.	34
2.9	Image sequence for the rotation mechanism.	35
3.1	Segregation flux functions, and large and small particle segregation velocities as a function of the small particle concentration ϕ^s	43
3.2	Photograph of the experimental apparatus and image sequence of a large red intruder segregating.	45
3.3	Image showing the contrast between dry and wet conditions using the RIM technique, and semi-opaque red intruder identified with the image analysis code.	47
3.4	Space-time plot of a large intruder segregating upwards in a medium of small particles and space time plot of a small intruder particle percolating down through a matrix of large particles.	48
3.5	Experimentally measured position of a 19 mm large intruder segregating through a 6 mm matrix of small particles as a function of time, for four different imposed shear rates.	55

List of Figures

3.6	Experimentally measured position of a large intruder of size $d_l = 10, 12, 19$ and 25 mm in a matrix of 6 mm small particles as a function of time, and at the same imposed shear-rate.	56
3.7	Large intruder trajectories for varying shear rate and size ratio collapsed onto an identity line by plotting the scaled height \mathcal{Z}^l against the scaled time $\mathcal{B}\dot{\gamma}_m d_s^2 (R-1)t$	57
3.8	Measured position of a 8 mm small intruder segregating through a 14 mm matrix of large particles as a function of time for three different imposed shear rates. .	59
3.9	Measured position of a 6 mm small intruder segregating through a 14 mm matrix of large particles as a function of time for three different imposed shear rates. .	60
3.10	Experimentally measured position of a small intruder of size $d_l = 12, 10, 8, 6$ and 4 mm in a matrix of 14 mm large particles as a function of time, and at the same imposed shear-rate.	61
3.11	Small intruder trajectories for varying shear rate and size ratio collapsed onto an identity line by plotting the scaled height \mathcal{Z}^s against the scaled time $\mathcal{B}\dot{\gamma}_m d_l^2 ((R-1) + \mathcal{E}(R-1)^2)t$	62
3.12	The non-dimensional segregation flux $S_r \phi^s \phi^l$, and non-dimensional large and small particle segregation velocities, \tilde{w}^l and \tilde{w}^s , as a function of ϕ	66
3.13	Contour plot of van der Vaart et al.'s (2015) small particle concentration data as a function of the non-dimensional depth $\tilde{z} = z/h$ and non-dimensional time $\tilde{t} = t/T$. Contour plot of the corresponding numerical results using the non-dimensional coefficients summarized in table 3.3.	68
3.14	Computed ϕ^s at $\tilde{t} = 221$ as a function of the non-dimensional depth, for $h = 87$ mm, $T = 13$ s, $\theta_{\max} = 30^\circ$, $d_s = 4$ mm, $d_l = 8$ mm and using the non-dimensional coefficients summarized in table 3.3.	70
4.1	Diagram of the conveyor belt setup.	84
4.2	Bulk volumetric concentration Φ , longitudinal velocity u and vertical velocity w fields at $t = 229.25$ s for Exp. 1 (see Tab. 4.2).	86
4.3	Normalized velocity profiles u^{*b} for 6 mm and 8 mm monodisperse experiments (Exps. 1 and 6 in Tab. 4.2).	88
4.4	Strain-rate tensor invariants fields: dilation I_D and shear rate II_D	90
4.5	Small particle concentration ϕ^s fields for Exps. 2-5 and Exps. 7-10.	91
4.6	Segregation flux f_{sl} for the $\Phi = 90\%$ experiment (Exp. 2, Tab. 4.2).	91
4.7	Normalized velocity profiles u^* for 6 mm and 8 mm bidisperse experiments at different Φ^s	92
4.8	Measurements of relative dilation at different fluid-exposure times for identical POM and PVC belt pieces.	95
A.1	PMMA and Triton X-100 experimental results - Vertical positions of small intruders of diameter $d_i = \{3.2, 4.8, 6.3\}$ mm segregating through a matrix of large particles.	105

- B.1 Diagram of the annular shear cell setup (rheometer). Idealized view from the rheometer lateral windows. Top and cross-section views of the annular cell. . . 109

List of Tables

3.1	Refractive indexes n_r , densities ρ , viscosities η and suppliers for the materials used in the 3D shear cell RIM experiments.	46
3.2	Diameters of the large particles d_l , small particles d_s , the size-ratio $R = d_l/d_s$ and average shear rates $\dot{\gamma}_m$ for each experimental set 1–5.	49
3.3	Non-dimensional coefficients \mathcal{B} , \mathcal{C} , \mathcal{E} determined from the refractive index matched shear cell experiments.	64
4.1	Refractive indexes n_r , intrinsic densities ρ_* and suppliers of the materials used for the conveyor belt RIM experiments.	82
4.2	Parameters of the experimental dataset: overall small particle concentration over the bulk Φ^s , the slope θ and the measured speed of the conveyor belt u_b . .	85
A.1	Refractive indexes n_r , densities ρ , viscosities η and suppliers for the PMMA - Triton X-100 experiments.	104
A.2	Experimental parameters for PMMA - Triton X-100 experiments. Intruder d_i and media d_m diameters, size ratios R , external shear rates $\dot{\gamma}_m$ and image acquisition frame rate per second (fps).	104

1 Introduction

“For it is natural for like to be affected by like and for things of the same kind to move towards one another and for each of the shapes to be reorganized into a different complex and so make another state.”

— DEMOCRITUS (SIMPLICIUS commentary on Physics)

1.1 Motivation

Grains and their movement have captured human curiosity and imagination for millennia. Since antiquity, the observation of grains and their dynamics have prompted, arguably, some of the most important scientific theories. A notable example is the one of Leucippus’ pupil Democritus, who gave origin to atomism when he famously elucidated that matter was formed by solid indivisible grains. Matter had to be granular.

The ubiquity of granular materials could explain the origin of Democritus’ statements. From clay and gravel to rice and salt, grains are present in a variety of natural environments and industrial processes. A striking feature of granular materials is that a single grain behaves differently than a group of them. While a single grain may generally behave as a solid, a collection of grains exhibit various, even simultaneous, behaviors (e.g., Jaeger et al., 1996; Ancy, 2007). Such behaviors are the result of mechanical forcings being transmitted, from the bulk- to grain-scale, from macro to microscale. Therefore, not only global bulk properties come into play, individual grain properties are also preponderant to characterize the eventual response of the granular material to the forcing.

Democritus also affirmed that atoms moved and collided in a vacuum space, giving shape to matter by rearranging according to their shape, order and posture (Leucippus and Democritus, 1999). Despite the fact that his statement aims to explain how the different types of matter are formed, a grain-sorting mechanism seems instrumental to explain his reasoning. In fact, polydisperse granular materials naturally segregate by their sizes, shapes or densities when

Chapter 1. Introduction

they flow (Ottino and Khakhar, 2000; Gray, 2018). If grains are fundamentally different, it is to be expected that an arrangement of one type of them is different than another of a different type. Therefore, grain rearrangement transforms the original material, modifying its characteristics, ergo, the way it responds to mechanical forcings.



(a) 2018 mudslide in Chamoson, Valais, Switzerland. (b) 2017 debris flow in Villa Santa Lucía, Aysén, Chile. ©La Tercera.
©Maxime Schmid/Keystone.



(c) 2008 pyroclastic and debris flow in Chaitén, Aysén, Chile. Modified from Gobierno de Chile CC BY 3.0 CL. (d) 2019 debris flow in Fully, Valais, Switzerland. ©Bob de Graffenried/LHE-EPFL.

Figure 1.1 – Examples of natural granular flows. The flows in the pictures are characterized by a rapid mass movement that alters natural environments and may devastate entire villages, as shown in (a)-(c). The commune of Chamoson has been affected by two debris flows in a year, in (a): the debris flow of 2018 that displaced 700 m^3 of material causing ~ 1 MCHF in damages. In (b) we distinguish two types of materials, easily identifiable by color, which indicate some sort of polydispersity (Sernageomin, in *Spanish*). In (c) the Chaitén pyroclastic flow was channelized by the Yelcho River and flooded the city, formed a beach and relocated the outlet of the Yelcho River. In (d) I show one of the two small debris flows that happened during August 2019 close to Fully. We see the flow spread in three separate currents (fingers) characterized by larger blocks at the front and the sides.

Besides these philosophical thoughts, the study of granular flows is also motivated by natural processes. The occurrence of gravity-driven granular flows in nature has great consequences

on ecosystems and human activities (e.g., Ancey, 2007; Delannay et al., 2017). Debris flows, avalanches and pyroclastic flows are important for sediment balance and geological processes, but may also produce human casualties and heavy economic loss. Due to climate change, we could expect an increment of debris flow and mudslide events, produced by more frequent and intense sudden storms over erodible dry-soils (Stoffel et al., 2014). In the past decade, mountain regions have been particularly affected by almost yearly events. In Chamoson, Switzerland, two debris flows have happened in a timespan of 370 days (see Fig. 1.1a). According to the authorities, “a villager could witness 3 to 4 events in his life”, in two years many have already fulfilled the quota¹. With estimated damages of 20 MCHF and two casualties, resilience to such devastating flows has become a priority for Swiss authorities in the face of climate change². In Chile, another mountainous country, debris flows also happen on a yearly basis. Surprisingly, nowadays in that country you are more likely to die or lose your house in a debris flow than in an earthquake. The Villa Santa Lucía town in southern Chile suffered an earthquake and a debris flow in less than a year. While the earthquake produced no casualties and the damage was minor, the debris flow razed the village and killed 21 people³. Clearly, efforts to better understand granular flows must be made so that risk area identification, mass movement determination and structural design are improved.

Size segregation plays an important role on the run-out of gravity-driven granular flows (Kokelaar et al., 2014). Granular currents are likely to form blunt bulky fronts (Johnson et al., 2012; Denissen et al., 2019), fingering instabilities (Pouliquen et al., 1997; Woodhouse et al., 2012) and levees (Mangeney et al., 2007; Rocha et al., 2019) that determine final run-out distance, velocity or channelization. Some of these phenomena have been found to be influenced by grain-sorting, which redistributes particles locally (Gray, 2018). At a relatively smaller scale, industrial granular mixing processes are particularly disturbed by particle segregation. For instance, pharmaceutical and agroindustrial activities are known to report economic losses due to inefficient mixing and reduced quality of their produce (Muzzio et al., 2003; Furukawa et al., 2016). Contrarily to these industries, the mining industry profits from size segregation to produce more stable and area-efficient stockpiles. The understanding of size segregation phenomena could reduce industrial costs and improve debris flow resilience.

From kinetic theory to mixture-theory models, the dynamics of granular flows and particle-size segregation have been intensively studied in the past decades. In recent years, the local $\mu(I)$ rheology appears to characterize a wide-range of flow configurations and materials under a single parameter, the non-dimensional inertial number I (Ancey et al., 1999; MiDi, 2004; Jop et al., 2006), similar to the Savage number $S I^2$ (Savage, 1984) or Coulomb number Co (Ancey and Evesque, 2000). In similar fashion, the mixture-theory based convection-diffusion equations of Gray and Thornton (2005) have been intensively used to describe size segregation in various flow configurations and conditions (e.g., Thornton and Gray, 2008; Gray and Ancey,

¹Lave torrentielle de Chamoson: décryptage d'un drame, *L'illustré*, August 23, 2019. *in French*

²New research centre to explore climate change and natural hazards in the Alpine region, Joint press release by the Canton of Grisons, ETH Zurich and WSL. June 12, 2020.

³Aluvión Villa Santa Lucía, Servicio Nacional de Geología y Minería. *in Spanish*

2011; Wiederseiner et al., 2011b; van der Vaart et al., 2015). Yet, a clear and quantifiable relation between rheology and size segregation in granular flows remains unclear.

Even though no mathematical or physical description was given by Democritus, many of his thoughts still serve as motivation for contemporary granular flow studies. The present thesis is no exception. Based on experimental observations, I want to address some of the questions that arise from the citation at the heading: what drives particles of the same kind to move towards one another? how does this segregation movement affect the state of the granular material or its rheology?

1.2 The rheology of dense granular flows

Governing equations

Consider a bulk of monodisperse grains flowing down an incline. For a bulk of density ρ , the mass and momentum equations can be written as

$$\frac{\partial \rho}{\partial t} + \nabla \cdot (\rho \mathbf{u}) = 0, \quad (1.1)$$

$$\rho \frac{d\mathbf{u}}{dt} = \nabla \cdot \boldsymbol{\sigma} + \rho \mathbf{g}, \quad (1.2)$$

where \mathbf{u} is the bulk velocity field, $\boldsymbol{\sigma} = -p\mathbf{1} + \boldsymbol{\tau}$ is the Cauchy stress tensor, and \mathbf{g} is the gravity. p is the pressure, $\mathbf{1}$ is the identity tensor and $\boldsymbol{\tau}$ is the deviatoric stress tensor. Note that if we consider a constant solids volume fraction Φ and a grains intrinsic density ρ_* , so that $\Phi = \rho/\rho_*$, Eq. 1.1 is reduced to an incompressible velocity field $\nabla \cdot \mathbf{u} = 0$ (Savage and Hutter, 1989; Gray, 2018).

To understand the origin and validity of the constitutive relations that determine the rheology of granular flows, I must first refer to the different flow regimes encountered for these flows.

Flow regimes

Dense granular flows can occur in a variety of flow configurations (e.g., silos, chutes, inclines, drums, etc.) and frictional conditions (Gray, 2001; Bertho et al., 2003; MiDi, 2004; Forterre and Pouliquen, 2008). Furthermore, granular flows are known to show different mechanical responses to stress. A bulk of grains will behave as a solid if it is at rest, whereas the very same bulk will behave as a fluid if sheared enough or as a gas if agitated strongly (Campbell, 1990; Jaeger et al., 1996). In some cases, these differing behaviors can even be encountered simultaneously (Ancy and Evesque, 2000; Gray and Ancy, 2011; Russell et al., 2019). Hence, the determination of a constitutive relation for granular flows, valid for all granular materials

and flow regimes, remains a challenging task.

As said, a dense bulk of cohesionless particles can exhibit various responses when subjected to a mechanical forcing. Mainly, the response is determined by grain inertia and grain-grain interactions, ranging from strong-frictional enduring contacts to highly-energetic instantaneous collisions (Campbell, 2006; Ancey, 2007). While some authors associate flow regimes to state-like characteristics (Jaeger et al., 1996), other authors prefer to associate elastic or plastic regimes to describe granular flows (Campbell, 1990; Goldhirsch, 2003). In this thesis I focused on the former regime classification.

Three regimes have been primarily identified by several authors: (i) collisional or grain-inertia regime, (ii) frictional or quasi-static regime, and (iii) frictional-collisional or transitional regime (Savage, 1984; Ancey et al., 1999; Ancey, 2007).

In the collisional regime, also called rapid-flow or grain-inertia regime, the flow can be described as very agitated or highly-sheared, with particle interactions dominated by instantaneous collisions (Bagnold, 1954; Savage, 1984; Campbell, 2006; Ancey, 2007). Since particle movement is subjected to interparticle collisions, its movement is highly random and it resembles molecular gas dynamics. Following that similarity, flows in this regime are usually modeled using kinetic theory models (e.g., Lun et al., 1984; Jenkins and Richman, 1985; Goldhirsch, 2003; Mitarai and Nakanishi, 2005; Berzi et al., 2020). These models are based on the concept of velocity fluctuations and granular temperature (Ogawa, 1978; Azanza et al., 1999), and are heavily based on statistical mechanics. Despite recent efforts to extend the application of kinetic theory models (Chialvo and Sundaresan, 2013; Berzi, 2014), usually this theory struggles to model flows under strong frictional contacts or jamming, i.e., where collisions are not the predominant grain-grain interaction.

The frictional, or quasi-static, regime is characterized by packed bulks that flow under very low shear rates, where frictional contacts are predominant and jamming is frequently observed (e.g., Savage, 1998; To et al., 2001; Silbert et al., 2002). In this regime, soil mechanics laws apply to the plastic flowing behavior of the bulk, such as Coulomb's law (Coulomb, 1773)

$$T = P \tan \zeta, \quad (1.3)$$

where ζ is the friction angle of the granular material, P is the normal stress and T the shear stress applied on the grains. This equation is an application of Mohr-Coulomb theory on a group of cohesionless grains flowing past their failure (Bagnold, 1954; Savage, 1984) and its usage has been translated to empirical constitutive laws for the transition between the frictional and collisional regime (MiDi, 2004).

Between the previous two regimes, lies the frictional-collisional regime (Ancey and Evesque, 2000; Ancey, 2007) or transitional regime (Savage, 1984). In this regime, grain inertia is dissipated through friction and collisions altogether, meaning that contact between particles

may be initiated by a collision but it endures enough to create friction between grains. The enduring contacts form stress networks at a rate that scales inversely to the bulk's shear-rate, $\dot{\gamma}^{-1}$. Despite being a transitional regime, arguably most of the dense granular flows mentioned in §1.1 can be considered to lie in the frictional-collisional regime.

For the past few decades, the regime classification for dense granular flows has relied heavily on dimensional analysis. Alongside the mentioned Coulomb's law (Eq. 1.3), other non-dimensional groups and empirical relationships have been keystones to determine constitutive relations for dense granular flows in the frictional-collisional regime (examples on other non-dimensional groups can be found in, Bagnold, 1954; Savage, 1984; Pouliquen, 1999; Ancey and Evesque, 2000; MiDi, 2004; Andreotti et al., 2013).

In this work I focused on granular flows in the frictional-collisional regime (Ancey and Evesque, 2000; Ancey, 2007), which is in the transition of Savage's (1984) regimes. This condition situates my approach far from kinetic theory models and close to empirically-based constitutive relations such as the $\mu(I)$ rheology, to be detailed in the next subsection.

$\mu(I)$ rheology

A large dataset of experiments and numerical simulations showed that dense granular flows in various configurations could be described via the inertial number (MiDi, 2004)

$$I = \frac{\dot{\gamma}d}{\sqrt{p/\rho_*}}, \quad (1.4)$$

where $\dot{\gamma}$ is the shear-rate and d is the grains' diameter. According to Ancey and Evesque (2000), the frictional-collisional regime can be characterized by a non-dimensional ratio of two time scales $t_p \sim \sqrt{\rho_* d^2 / p}$ and $t_n \sim \dot{\gamma}^{-1}$. The relaxation time t_p represents the time a particle requires to travel its radius r due to the action of normal stresses. The other time scale t_n is given by the time a contact network endures. Therefore the time-scales' ratio results in the non-dimensional number $Co = (t_p / t_n)^2 = \rho_* r^2 \dot{\gamma}^2 / p$, which is a precursor of I and also similar to one of Savage's (1984) non-dimensional parameters.

For uniform steady flows, as encountered in simple-shear flows, the friction coefficient μ can only be a function of I , so Eq. 1.3 can be reduced to (Jop et al., 2006)

$$T = \mu(I)P, \quad (1.5)$$

for which $\mu(I)$ can be determined empirically using the function suggested by Jop et al. (2006)

$$\mu(I) = \mu_s + \frac{\mu_2 - \mu_s}{I_0/I + 1}, \quad (1.6)$$

where $\mu_s = \tan \theta_1$ and $\mu_2 = \tan \theta_2$ are limiting values that set μ minimum and maximum values at $I \rightarrow 0$ and $I \rightarrow \infty$, respectively. I_0 is a constant determined by the granular material properties. Jop et al. (2006) also proposed a generalization of the $\mu(I)$ rheology for three-dimensional granular flows, for which the bulk stress tensor was defined as

$$\boldsymbol{\sigma} = -p\mathbf{1} + \mu(I)p \frac{\mathbf{D}}{II_{\mathbf{D}}}, \quad (1.7)$$

where $\mathbf{1}$ is the identity tensor, \mathbf{D} is the strain-rate tensor and $II_{\mathbf{D}}$ its second invariant, or the shear-rate. The strain-rate tensor was considered as (e.g., Timošenko and Goodier, 1988; Andreotti et al., 2013)

$$\mathbf{D} = \frac{1}{2} (\nabla \mathbf{u} + (\nabla \mathbf{u})^T), \quad (1.8)$$

where $\nabla \mathbf{u}$ is the gradient of the velocity and T is the transpose. An effective viscosity can be introduced as $\eta = \mu(I)p/(2II_{\mathbf{D}})$. With this generalization, the inertial number is redefined as

$$I = \frac{2II_{\mathbf{D}}d}{\sqrt{p/\rho_*}}. \quad (1.9)$$

An important result can be obtained for a uniform and steady flow of height h down a slope θ incline using the inertial number definition. The Bagnold-like velocity profile, $u \sim h^{3/2}$, can be retrieved from Eq. 1.2 by considering a hydrostatic pressure distribution $p = \rho g(h - z) \cos \theta$ and Eq. 1.5 (MiDi, 2004)

$$u(z) = \frac{2}{3} \frac{I(\theta) \sqrt{g \cos \theta} h^{3/2}}{d} \left(1 - (1 - z/h)^{3/2}\right), \quad (1.10)$$

where $I(\theta)$ can be calculated using Eq. 1.6

$$I(\theta) = I_0 \frac{\tan \theta - \tan \theta_1}{\tan \theta_2 - \tan \theta}. \quad (1.11)$$

Despite the success of the $\mu(I)$ rheology to capture a wide range of flow configurations, its formulation is far from being definitive or complete. For instance, a couple of regularizations for the $\mu(I)$ function have been proposed to address its ill-posedness (Barker et al., 2015; Barker and Gray, 2017; Heyman et al., 2017). In another aspect, most relevant for this thesis, I was initially defined for a flow of monodisperse grains, i.e., $I \sim d$ (see Eq. 1.4). Dense granular flows are known to be polydisperse in nature, composed by grains of a wide range of sizes,

shapes or densities. The $\mu(I)$ rheology does not include any polydispersity effects in d (Eq. 1.9). To my knowledge, only the works of Rognon et al. (2007) and Tripathi and Khakhar (2011) have extended the $\mu(I)$ rheology to include grains of different sizes, by considering a volume or area averaged diameter of two grain species. Yet, and as I am about to discuss in the next subsection, the role of polydispersity on the rheology of granular flows is far from understood.

1.3 Particle-size segregation

Whether it is their size, shape, composition or density, natural grains are different to each other. This polydispersity, so inherent to granular materials, gives origin to grain-segregation phenomena in granular flows. Even the slightest size difference can result in internal grain movement that rearranges the bulk by its species. Grain sorting is usually produced by a mechanical action that creates spacing or voids, which facilitates grain rearrangement that fills the created volume gaps. While there are many mechanical forcings that lead to particle-size segregation, shearing is an efficient forcing that is commonly produced by friction in natural and industrial processes. In particular, particle-size segregation is frequently observed in dense granular flows, which in counterpart sort them efficiently.

Shear-driven segregation mechanisms

Several size segregation mechanisms have been identified to affect granular materials, yet most of them do not bear a significant effect for gravity-driven dense granular flows (Williams, 1976; McCarthy, 2009). Only two shear-driven segregation mechanisms have been identified as crucial for these flows' dynamics, the (i) kinetic sieving (Middleton, 1970), and (ii) squeeze expulsion (Savage and Lun, 1988) mechanisms.

The kinetic sieving mechanism is yielded by the shear-induced relative movement of particle layers. Large particle movement creates gaps through which smaller grains fall, thus sieved by large particle movement.

The squeeze expulsion mechanism was initially described as a particle being squeezed out of its own layer by surrounding grains (Savage and Lun, 1988). It is possible to see this mechanism as a counterpart of kinetic sieving, whereas kinetic sieving produces a flux of small particles towards the base of the flow, squeeze expulsion produces a flux of large particles towards the bulk's surface as a result of force imbalances.

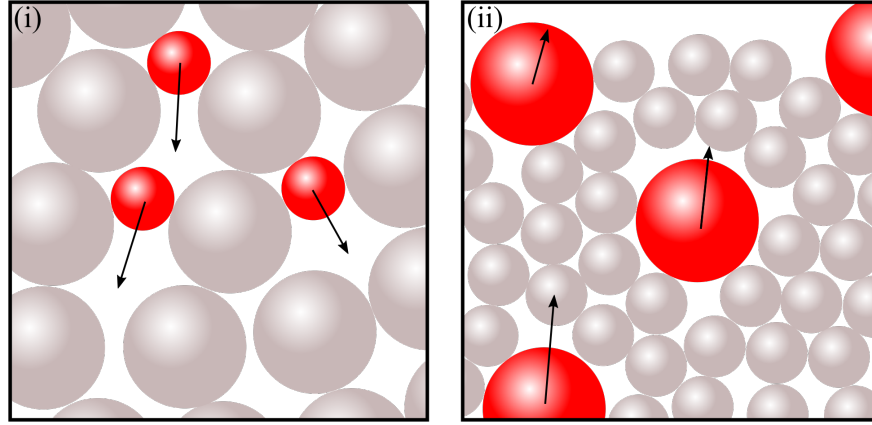


Figure 1.2 – Sketches illustrating the shear-driven size-segregation mechanisms: (i) kinetic sieving (Middleton, 1970), and (ii) squeeze expulsion (Savage and Lun, 1988). In (i), the smaller red grains fall through gaps left beneath them by the large particles' movement. In (ii), the larger red particles are squeezed to the upper layers by the surrounding smaller particles.

These mechanisms are somehow tied, arguably through mass or net-flux continuity (Hill and Fan, 2016; Jones et al., 2018; Gray, 2018), but their connection is still not clear. The uncertainties come primarily from the squeeze expulsion mechanism. Its origin or the nature of the forces that produce the mechanism are not well understood. Stress partitioning (Gray and Thornton, 2005; Hill and Tan, 2014), force or pressure fluctuations (Staron, 2018), viscous drag (van der Vaart et al., 2018b) or buoyancy-like forces (Guillard et al., 2016; Jing et al., 2020) have been raised as plausible explanations for the occurrence of squeeze expulsion without major consensus.

Convection-diffusion segregation model

For a bidisperse grain mixture of different species $v = \{s, l\}$, representing small and large particles, the species' relative volume fractions ϕ^v must satisfy

$$\sum_v \phi^v = 1. \quad (1.12)$$

This equation is sustained by a quasi-invariant Φ , which also meant $\nabla \cdot \mathbf{u} = 0$ in Eq. 1.1 (Gray, 2018). Equation 1.1 sets the base for the mixture-theory of Gray and Thornton (2005), who presented a set of mass and momentum equations for each v species that derived a convective-diffusion model for a bidisperse grain mixture. Gray and Anczyk (2011) extended these equations to a polydisperse granular bulk using multicomponent mixture-theory to model polydisperse particle-size segregation.

Chapter 1. Introduction

Returning to a bidisperse case, Gray and Ancey's (2011) equation for each v species is written as

$$\frac{\partial \phi^v}{\partial t} + \nabla \cdot (\phi^v \mathbf{u}) + \nabla \cdot \mathbf{F}^v = \nabla \cdot (\mathcal{D} \nabla \phi^v), \quad (1.13)$$

where \mathbf{F}^v are the segregation fluxes and \mathcal{D} is the diffusion coefficient. The segregation fluxes are gravity oriented and satisfy $\mathbf{F}^s = -\mathbf{F}^l = F^s \mathbf{g}/|\mathbf{g}|$ (Gray, 2018).

Segregation flux functions and asymmetric behavior

The properties and functional form of F^s are decisive for the correct characterization of the segregation processes. Bridgwater et al. (1985) proposed that segregation fluxes in a bidisperse mixture were a cubic function of ϕ^v , which for F^s would mean

$$F^s = -q\phi^s(1 - \phi^s)^2, \quad (1.14)$$

where q is the segregation rate. This cubic functional form satisfies $F^s = 0$ for $\phi^s = \{0, 1\}$, a condition first observed by Bridgwater et al. (1985) that satisfies a no-flux condition when the bulk is monodisperse. Alternatively, Dolgunin and Ukolov (1995) proposed a quadratic function for the segregation flux, expressed as

$$F^s = -q\phi^s(1 - \phi^s), \quad (1.15)$$

which satisfies the condition already mentioned and noted by Bridgwater et al. (1985).

However, the segregation fluxes have an underlying asymmetric behavior. First observed experimentally by van der Vaart et al. (2015), small and large particles have fundamentally different segregation time-scales. In an attempt to describe this size-segregation asymmetry, Gajjar and Gray (2014) suggested the following cubic function

$$F^s = -qA_\chi\phi^s(1 - \phi^s)(1 - \chi\phi^s), \quad (1.16)$$

where $\chi \in [0, 1]$ is a coefficient that determines the flux function skewness or asymmetry. A_χ is a normalization factor to give this function the same segregation magnitude as that of the quadratic flux function when $\chi = 0$. The flux function of Gajjar and Gray (2014), and the segregation velocities for small and large particles are plotted in Fig. 1.3. The asymmetry can be seen in Fig. 1.3(b-c), the segregation velocity for a single small particle, represented by $\phi^s = 0^+$ in (c), and a single large particle, represented by $\phi^s = 1^-$ in (b), become different as χ

(red \rightarrow blue) increases. Gajjar and Gray's (2014) function has the particularity that it recovers the functions of Bridgwater et al. (1985) and Dolgunin and Ukolov (1995) for $\chi = 0$ and $\chi = 1$, respectively.

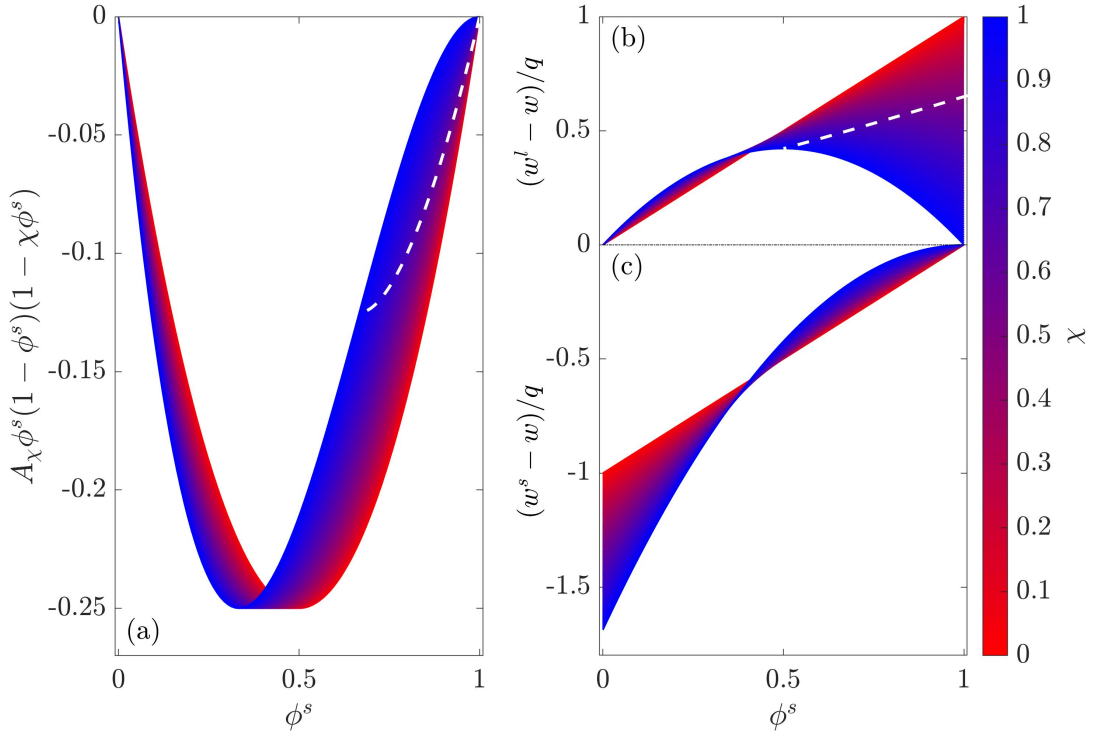


Figure 1.3 – (a) Segregation flux function of Gajjar and Gray (2014), and (b) the large $(w^l - w)$ and (c) small $(w^s - w)$ particle segregation velocities as functions of ϕ^s and the asymmetry parameter χ . For $\chi = 0$ and $\chi = 1$, Dolgunin and Ukolov's (1995) quadratic and Bridgwater et al.'s (1985) cubic functions are respectively recovered. All the functions have the same segregation flux amplitude due to the normalization factor A_χ . The flux functions have an inflection point $\phi_{inf}^s = (1 + \chi)/(3\chi)$ for $\chi = [1/2, 1]$ (dashed white line in a) and large particles segregate faster at $\phi_{max}^s = 1/(2\chi)$ (dashed white line in b). Adapted from Gray (2018) with permission of Prof. Nico Gray.

Despite the particularity of Gajjar and Gray's (2014) function and the discovery of the segregation asymmetry, all the presented flux functions depend solely on ϕ^s as their main physical variable. So far, no clear role has been attributed to other physical parameters that have been found to determine faster or slower segregation rates. Important parameters, like the particles' size ratio, or physical forcings, like pressure or shear are still absent in the definitions of q or F^s .

1.4 Experimental techniques and methods

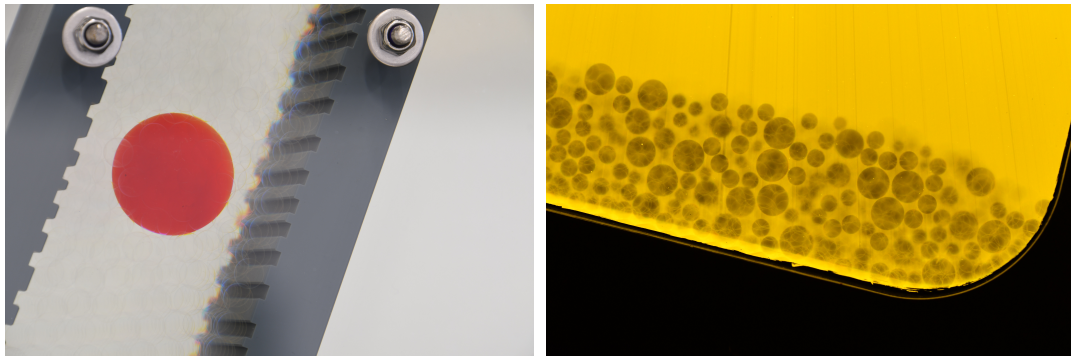
For this work, the main approach to study dense granular flows was experimental. Thus, I provide an introduction to the techniques and methods that were most used for this thesis. To avoid further redundancy with the main chapters of this thesis, the specific experimental facilities and setups are presented and described in them.

Refractive index matching

Most granular materials are opaque, so the experimental observation of their flow dynamics can pose several obstacles. Even if surface or wall measurements can already provide substantial information about velocity or concentration fields, the suppositions to obtain such fields are often strong and particular to the analyzed case (Sarno et al., 2016). Wall effects, singularities and the unclear relation between stress and strain makes internal direct measurements a valuable asset.

Several high-end technologies –namely, electrical capacitance tomography, radiography, magnetic resonance imaging –have been used to obtain internal granular flow images or concentration fields (for examples or reviews on these techniques, see Zhu et al., 2003; Elkins and Alley, 2007; Guillard et al., 2017). Despite the increasing precision and usage of these technologies, their costs and implementation risks are still considerably higher than those of simpler techniques, such as the Refractive Index Matching (RIM) technique (Dijksman et al., 2012).

The RIM technique is based on a very basic principle: matching the refractive index n_r of the granular material to that of an interstitial fluid. In Fig. 1.4 we can see examples of the RIM technique usage. The addition of a fluorescent agent allows the observation of dark shapes when the mixture is exposed to a laser that excites the agent accordingly. As a result, the observer visualizes the glass beads as dark circles that can be identified and traced (Fig. 1.4(b)).



(a) RIM in a shear cell to visualize an opaque red intruder. (b) RIM in a conveyor-belt flume with laser-induced fluorescence.

Figure 1.4 – Refractive index match applied in: (a) a shear cell and (b) a flume. The left image profits from the RIM technique to visualize an opaque bead immersed in a RIM bath of transparent glass beads, ethanol and benzyl-alcohol. The right image uses laser-induced fluorescence to observe the index-matched granular particles as dark circles that can be identified and traced afterwards.

While straightforward, the technique is not free of difficulties. Possible matches are few, and they often involve complex fluids with undesirable characteristics (Dijksman et al., 2012). Another major difficulty to apply the technique successfully is the required precision. Differences of $2 \cdot 10^{-4}$ between the grains and fluid indexes have been reported to significantly affect image quality (Wiederseiner et al., 2011a). Therefore, enclosed and controlled environments are highly recommended, since variations in temperature or humidity may increment the n_r differences above the mentioned threshold value.

The detailed reviews of Wiederseiner et al. (2011a) and Dijksman et al. (2012) explored many combinations of materials that could be used for the RIM technique at a laboratory-scale. A variety of plastics and glasses are presented as suitable candidates for a low refractive-index match, among which glass has been used in recent studies on granular flows and size segregation (van der Vaart et al., 2015; Sanvitale and Bowman, 2016; van der Vaart et al., 2018a). To match the particles' n_r , Wiederseiner et al. (2011a) present various articles that used different fluids or mixtures. Most of these studies use high viscosity or high density fluids, such as glycerol, Triton X-100 or sodium iodide (e.g., Park et al., 1989; Chen and Fan, 1992; Kapoor and Acrivos, 1995).

Despite the good results in terms of the refractive index match, viscous or dense fluids create conditions that are not desirable for a flow that should resemble a dry granular flow. Viscous fluids reduce interparticle friction and dense fluids increase buoyancy, which set the dynamics far from the frictional-collisional regime (Ancy and Evesque, 2000; Ancy, 2007). To set a negatively buoyant match with a low viscosity fluid that could reproduce the dynamics of granular flows, van der Vaart et al.'s (2015) used a mixture of ethanol ($n_r = 1.3656$) and benzyl-

alcohol ($n_r = 1.5396$). A wide range of refractive index value can be achieved with mixtures at different concentrations a feature that, combined with a viscosity and density close to that of water, makes them suitable candidates (Chen et al., 2012). Recently, Rousseau and Ancey (2020) used this RIM mixture successfully to study turbulent flow through porous media.

Particle tracking velocimetry

Particle-imaging methods are low-cost and widely-used techniques in experimental fluid mechanics (Adrian, 1991). Among these methods, the Particle Tracking Velocimetry (PTV) technique, which is based on a Lagrangian approach, is broadly used to track particles in dense granular flows (Jesuthasan et al., 2006). Even if these flows do have a high solid concentration, the number of particles is comparatively lower than those observed in seeded flows for Particle Imaging Velocimetry (PIV) measurements. More recently, PTV has been the default method to obtain data from granular flows (Gollin et al., 2017).

Usually, PTV algorithms have two stages: identification of particles and tracing their trajectories. The particle identification process can be done using a wide range of techniques: binary detection, pattern or feature tracer, functional convolution, Voronoï diagrams, among others (e.g., Ohmi and Li, 2000; Capart et al., 2002; Gollin et al., 2017). Particle trajectories are then calculated from the detected particles' positions and radius. Similarly to the identification techniques, there are plenty of tracking methods (e.g., Baek and Lee, 1996; Crocker and Grier, 1996; Capart et al., 2002).

Recent implementation of circle identification algorithms in Matlab made possible the access to robust and proven spherical particle identification algorithms (MAT, 2019)¹. This routine uses a circular Hough transform to determine different phases (phase-coding) or radial histograms centered at the different spatial image points (Atherton and Kerbyson, 1999; Davies, 2004). The open-source code of Crocker and Grier's (1996), available on the internet for Matlab and Python², presents a robust and simple way to correlate particle positions and has proven to give good results for granular flows (e.g., Hill et al., 2003; Windows-Yule et al., 2020).

1.5 Objectives and research contributions

The main objective of this dissertation is to characterize experimentally the coupling between size segregation and rheology in dense bidisperse granular flows.

From this broad objective, specific goals were drawn to address it:

- To characterize the relation between strain-rate and size segregation in dense granular flows.

¹Find circles using circular Hough transform - MATLAB `imfindcircles`

²Particle tracking using IDL, John C. Crocker and Eric R. Weeks

- To understand the role of size ratio on the underlying asymmetry in size segregation fluxes.
- To find a clear functional form for the segregation flux function, which depends on physical parameters or flux variables.
- To model how flow and segregation affect each other in uniform and steady flow conditions.

To achieve these goals, I present briefly three main contributions.

Dilation and shear rate roles in large particle segregation

A two-dimensional shear cell was used to study the segregation of a single large intruder. Experiments with various intruder sizes were compared in terms of the measured strain-rate around the intruder, its segregation rate, and its rotation velocity. The results showed that size segregation depended on the strain-rate around the intruder, and for small size differences, on the intruder rotation. Despite being a very specific technical contribution, the observed differences in the way large particles segregate indicate a tight relation between segregation rate and size differences. An implication of this contribution is that segregation could be inhibited for small size differences if friction between grains is reduced so no rotation is produced.

A scaling law for particle-size segregation

To determine the functional form for the segregation flux function F , we profited from the boundary conditions of the flux function (Fig. 1.3). When $\phi_s = 0^+$ and $\phi_s = 1^-$, a single particle characterizes its whole species. Moreover, the velocity of a single particle approximates to the segregation rate. Based on this particular condition, we carried out experiments in a three-dimensional shear cell. For the experiments, we used a single opaque intruder submersed in a RIM mixture of transparent grains of different sizes. Different shear-rates and size-ratios shed light on a dimensional analysis that gave us the functional form. We compared our results to those of van der Vaart et al. (2015) and we identified that the size ratio was able to explain physically the segregation asymmetry. This contribution has a direct importance for size segregation models that could be translated to industrial applications.

Internal dynamics of stationary granular avalanches

To visualize how the rheology affects particle-size segregation, I carried out RIM experiments in an inclined conveyor belt flume. This setup imposed steady and uniform flow conditions for an experimental set of mono and bidisperse granular avalanches. The experimental results were focused on the effects that velocity profiles and strain-rate had on particle concentrations, segregation and recirculation. Interestingly, the results showed two flow regions for all experiments: (i) a convective-dilated front, and (ii) a well-arranged layered tail. For bidisperse avalanches, these two regions combined formed a breaking-size segregation wave structure

whose length was controlled by the avalanche's overall species concentration Φ^s . Bagnold-like velocity profiles were measured, which prove that an equivalent $\mu(I)$ can be established for an equivalent concentration-dependent diameter. The obtained results could be used to validate or elaborate a rheology-segregation model employing travelling-wave solutions that mimic the experimental flow conditions.

1.6 Dissertation outline

Besides this introductory chapter, this dissertation comprises three main chapters. Each chapter elaborates on a contribution in the form of a research manuscript for publication. The main body of this thesis ends with the concluding remarks, after which I present three appendices on other relevant aspects of my work.

Chapter 2 provides an in-depth description of the two-dimensional shear cell experimental setup and a literature revision on the segregation of large particles. In this chapter, the results of the dilation and shear rate role on large particle segregation are presented and discussed.

Chapter 3 presents the scaling law for particle-size segregation. A state of the research on particle-size segregation is presented, along with a description of the three-dimensional shear cell setup. The experimental data set and results are presented with the corresponding analysis and the determined scaling law. The data of van der Vaart et al. (2015) is used for comparison and to validate the proposed functional form.

Chapter 4 describes the conveyor belt setup and the difficulties associated with its construction process and usage. Experimental results of mono- and bidisperse experiments are presented, to discuss the role of particle concentration in velocity fields, particle recirculation and segregation of stationary granular avalanches.

Finally, Chapter 5 presents the conclusions and outcomes of the previous chapters and this dissertation. The chapter finishes with a brief discussion on the potential outreach and perspectives for future challenges on the subject.

2 Large particle segregation in sheared dense granular flows

Tomás Trehela¹, J. M. N. T. Gray², and Christophe Ancey¹

¹ Laboratory of Environmental Hydraulics, École Polytechnique Fédérale de Lausanne, Lausanne, Switzerland.

² Department of Mathematics and Manchester Centre for Nonlinear Dynamics, University of Manchester, Oxford Road, Manchester M13 9PL, UK.

Under revision in *Physical Review Fluids*.

Doctoral candidate's contribution

For this chapter, the candidate carried out the experiments, processed the images, did the analyses and wrote the manuscript. General comments were received from Prof. Ancey and Prof. Gray. The initial idea for the experiments was of Prof. Gray but the developments on the strain-rate invariants and size ratio role on the mechanism were original ideas of the candidate.

Abstract

We studied the segregation of single large intruder particles in monodisperse granular materials. Experiments were carried out in a two-dimensional shear cell using different media and intruder diameters, whose quotient defined a size ratio that ranges from 0.3 to 0.833. When sheared, the intruders segregated and rotated at different rates, which depended on their size ratio and depth. We observed greater dilation around the intruders when size ratios were closer to zero, which in turn promoted a faster segregation. However, experiments with small size ratios showed that intruder rotation was weak and local shear rates were low. On the contrary, experiments with size ratios close to unity resulted in strong intruder rotation, high local shear rates, and contraction below the intruder. Therefore, an intruder with a diameter close to that of the medium also relies on rotation to segregate. We propose that large particle

Chapter 2. Large particle segregation in sheared dense granular flows

segregation depends on local dilation and, to a lesser extent, the local shear rate. Based on our observations we redefine large particle segregation as two well-defined processes dependent on the size ratio and local strain rate.

2.1 Introduction

Polydisperse granular materials naturally segregate according to their species' size when sheared. Grain size segregation generates or favors complex phenomena such as stratification (Makse et al., 1997), fingering (Pouliquen et al., 1997; Woodhouse et al., 2012), levees (Iverson, 1997; Félix and Thomas, 2004), front bulging (Takahashi, 1981; Denissen et al., 2019) and channelization (Mangeney et al., 2007; Kokelaar et al., 2014). Segregation processes affect geophysical flow characteristics (Delannay et al., 2017), mining extraction (Virčíková and Molnar, 1992), mixing in industrial or food processing (Shinbrot, 2004) and landforms (Makse, 2000). Large-particle segregation, in particular, is of great importance in helping us to comprehend debris-flow dynamics and to interpret geophysical flow deposits better (Gray and Kokelaar, 2010). In summary, studying particle-size segregation, and in particular how large grains segregate, is key to understand the dynamics of granular matter (Gray, 2018).

A variety of mechanisms to segregate particles have been identified and studied for various flow configurations (Bridgwater, 1976; Williams, 1976), with the segregation of large particles called *the Brazil nut effect* in vibrated systems (Rosato et al., 1987). Simultaneously, the shear-induced mechanisms *random fluctuating sieving*, also known as *kinetic sieving* (Middleton, 1970; Savage and Lun, 1988), and *squeeze expulsion* have been studied recurrently (Gray, 2018). Experimental observations and numerical simulations have described the mechanics of the *kinetic sieving* process precisely: this consists of small particles percolating through gaps generated by the relative movements of particle layers. The origin and nature of the *squeeze expulsion* mechanism, however, are not subject to a consensus. It was defined originally by Savage and Lun (1988) as imbalances in the contact forces applied on an individual particle which squeeze it out of its own layer into an adjacent one. Other authors have proposed that the mechanism results from mass continuity or a net flux balance (Hill and Fan, 2016; Jones et al., 2018). Therefore, a large particle will only rise if the surrounding voids are filled with percolating smaller particles. This assumption may hold for certain cases, but small particle percolation tends to be less pressure-dependent and segregation fluxes have been found to be asymmetric (Golick and Daniels, 2009; van der Vaart et al., 2015; Jones et al., 2018). This segregation flux asymmetry suggests that a connection between the two mechanisms may not be direct or independent of the particles size ratio or the local particle concentration.

Efforts to explain why large particles segregate have been particularly intense in recent years. Guillard et al. (2016) proposed a scaling to define a segregation force. They found that this force was similar to a lift force and that it depended on stress distribution. However, Guillard et al. (2016) did not address how a large intruder rises and how shear stress contributes to segregation. To address the question of why large particles segregate, van der Vaart et al. (2018b) proposed an analogy with the Saffman effect. They introduced a buoyancy-like force that depends on the size ratio to answer this question. The origin of this granular Saffman effect is similar to viscous drag, but in their work this drag is exerted by a granular flow. Recently, Staron (2018) failed to observe any lift-like force under flow conditions similar to those described by van der Vaart et al. (2018b). Staron (2018) concluded that force fluctuations

around the intruder should be responsible for large particle segregation. Resistance is higher towards a rigid fixed bottom, hence any force imbalance pushes the intruder upwards. An analogy to a plunging object was proposed by Staron (2018), based on previous work by Hill et al. (2005), to illustrate the previous sentence. The role of interparticle friction and rotation in particle segregation was studied by Jing et al. (2017) through numerical simulations. Jing et al. (2017) found that large particle segregation was suppressed when interparticle friction and rotation were negligible. They proposed that the rotation of a large particle is necessary for its segregation.

Particle size segregation of a single large particle has been studied at the laboratory scale. The work by van der Vaart et al. (2015) considered large particles segregating in a simple shear cell, but their results focused on segregation flux asymmetry. Other studies measured lift and drag forces acting over intruders in granular media (Ding et al., 2011; Guillard et al., 2014; Seguin et al., 2016). These intruders were held fixed or moved artificially, so no direct relation could be established between their results and the segregation of a single large particle.

To study the segregation of a large particle, we used a two-dimensional shear cell filled with small particles, in which one large particle (the intruder) was placed. The cell configuration imposed a flow condition different from those used by Guillard et al. (2016), van der Vaart et al. (2018b) and Staron (2018). In our experiments, shear was constant in depth but oscillated through time and the intruder moved freely towards the bulk free surface by the action of shear. Particle trajectories and velocity fields were determined using particle tracking velocimetry and interpolation routines, respectively. The strain rate tensor and its invariants were estimated to reveal how the granular material responded to external shear, as done in previous studies (Drescher and De Jong, 1972; Seguin et al., 2016). Various intruder and medium diameters were used to shed light on the role of size ratio in large particle segregation.

2.2 Methods

Experiments were carried out in a 5 mm-thick, two-dimensional, shear cell consisting of two parallel poly(vinyl chloride) (PVC) side-plates that rotated over axes located at their bases (see Fig. 2.1). The PVC side-plates were corrugated and had a roughness that scaled to d_m . Cell width was set between $W = 85$ and 145 mm in $\Delta W = 15$ mm steps. A granular material between the plates was sheared by their cyclic movements. Since the side plates were parallel, the externally imposed shear rate was independent of the depth but was periodic in time. The external shear rate is expressed by

$$\dot{\gamma}_e(t) = \tan \theta_{max} \omega |\cos(\omega t)|, \quad (2.1)$$

where $\theta_{max} = 15^\circ$ was the plates' maximum angle of inclination. The frequency $\omega = 2\pi/T$ was given by the period $T = 19.75$ s. Both parameters were fixed at those values for all the experiments.

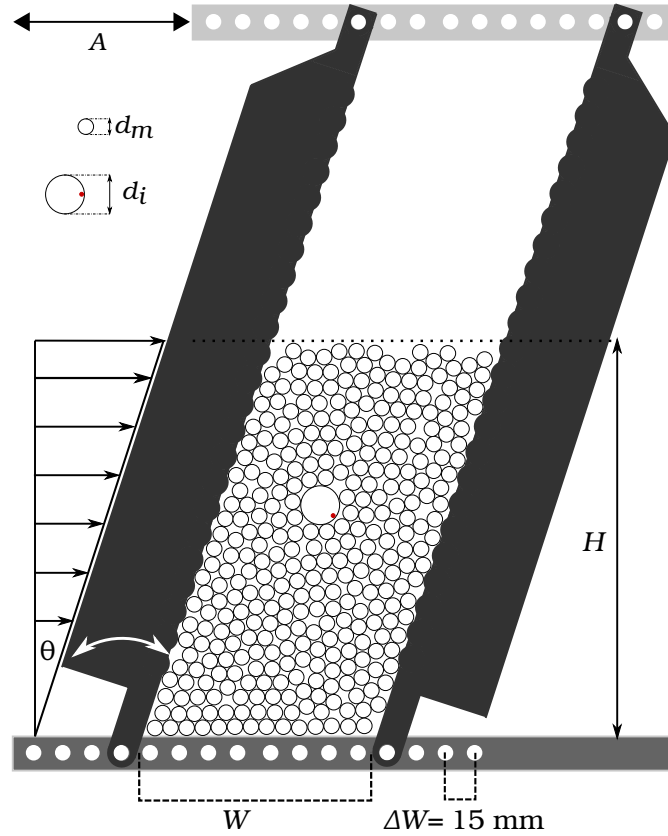


Figure 2.1 – Scaled schema of the 2D shear cell setup. d_m is the diameter of the disks forming the surrounding granular medium, d_i is the diameter of the intruder and A represents the amplitude generated by the cyclic movement of the plates. Bulk height $H = 19$ cm and maximum plate inclination $\theta_{max} = 15^\circ$ were the same for all experiments. Cell width W was changed for each d_m to maintain a fixed ratio of $W/d_m \approx 14$ for all experiments.

Simple shear cells or boxes have been used previously to study granular and segregation processes (e.g., Scott and Bridgwater, 1976; Stephens and Bridgwater, 1978b; van der Vaart et al., 2015)). Stephens and Bridgwater (1978b) observed that the percolation rates and segregation mechanisms in simple shear cells were quite similar to those found in annular shear cells.

A dry granular medium made of polyoxymethylene (POM) disks of diameter d_m and an intruder disk of the same material, but of a different diameter d_i , were placed between the cell's plates and glass panels. Three different disk diameters were employed as the surrounding media: $d_m = 6, 8$ and 10 mm. Only disks larger than the medium's disk diameter were used as intruders: $d_i = 10, 12, 14, 18$ and 20 mm. To quantify intruder rotation, a red dot was drawn on the edge of the intruders circumference. Commercial POM has a density of 1.42 gr cm^{-3} and a Young's modulus of 3000 MPa . According to Vaziri et al. (1988), the frictional coefficient between POM cylinders sliding on each other at low velocities is 0.16 .

The single intruder was initially placed in the center of the cell at a height of 4 cm, measured from the cell bottom to the lowest point of the intruder's circumference. The cell was then filled with the smaller disks up to a height of 19 cm, creating an effective bulk height of $h = 15$ cm over the intruder. This latter condition was maintained for all experiments.

Due to the characteristics of the cell, the appearance of the Janssen effect (Janssen, 1895) was an initial concern. Experiments with narrow width $W/d_m \approx 9$ showed a slightly different behavior, a constant segregation rate close to the cell's bottom. A constant vertical velocity of the intruder suggested that not only shear was constant with depth, pressure was also constant on depth, hence affected by Janssen effect. To avoid this effect, W was incremented for the present set of experiments. The variable and depth-dependent segregation rate of the intruder during the entire experiment suggest that Janssen effect was negligible compared to the previous narrower experiment.

2.2.1 Image acquisition and particle tracking

Experimental run-times ranged from 15 to 70 minutes. Each experiment was recorded using a Basler acA2000-165uc camera at 4 frames per second. The position and radius of every POM disk were determined using a circular Hough-transform algorithm available on Matlab (MAT, 2019). A particle tracking algorithm was used to correlate positions to trajectories (Crocker and Grier, 1996). First, the intruder position $\mathbf{r}_i = (x_i, z_i)$ and its velocity $\mathbf{u}_i = (u_i, w_i) = \partial \mathbf{r}_i / \partial t$ were determined separately as functions of time t . Secondly, all particle positions \mathbf{r}_m and trajectories were used to calculate particles velocities \mathbf{u}_m . Finally, spatial interpolation of the particles velocity at a certain time t enabled the calculation of the entire bulk's velocity field \mathbf{u} .

2.2.2 Intruder rotation

Red dot identification and tracking were done simultaneously to intruder tracking. The dot's position \mathbf{r}_d and movement, relative to the intruder's position, were used to estimate the intruder's angular velocity $\boldsymbol{\Omega}_i = 4\mathbf{r}_d \times \mathbf{u}_d / d_i^2$. Since rotation had no preferential direction, we were interested in the magnitude of $\boldsymbol{\Omega}_i$ so its norm was considered as relevant $\Omega_i = |\boldsymbol{\Omega}_i|$.

A conditional probability $P(w_i|\Omega_i) = P(w_i, \Omega_i) / P(\Omega_i)$ was calculated to quantify the occurrence of segregation and rotation. This probability was determined from a bivariate probability distribution function (pdf) of the time series of the intruder's vertical velocity w_i and angular velocity Ω_i . The bivariate pdf $P(w_i, \Omega_i)$ was calculated using Matlab's *mvnpdf* function (MAT, 2019). The second probability distribution function, for Ω_i alone, was determined using Matlab's *pdf* function.

2.2.3 Strain rate tensor invariants

The strain rate tensor $\mathbf{D} = \frac{1}{2}(\nabla \mathbf{u} + \nabla \mathbf{u}')$ was estimated from the velocity field \mathbf{u} . A tensor decomposition determined its first invariant, the dilation (Timošenko and Goodier, 1988; Landau and Lifšic, 1999)

$$I_{\mathbf{D}} = \frac{1}{2} \text{tr}(\mathbf{D}) = \frac{1}{2} (\nabla \cdot \mathbf{u}), \quad (2.2)$$

which is proportional to the velocity field's divergence. The strain rate tensor's second invariant was obtained from the deviatoric strain rate tensor

$$II_{\mathbf{D}} = \left(\frac{1}{2} \text{tr}(\mathbf{S}^2) \right)^{1/2}, \quad (2.3)$$

where $\mathbf{S} = -\frac{1}{2} I_{\mathbf{D}} \mathbf{1} + \mathbf{D}$ is the deviatoric strain rate tensor. This second invariant is called the shear rate (Andreotti et al., 2013). Both invariants were estimated from the velocity fields, which themselves resulted in the fields $I_{\mathbf{D}} = f(x, z)$ and $II_{\mathbf{D}} = f(x, z)$ for each time step.

To analyze the local strain rate around the intruder, we evaluated $I_{\mathbf{D}}$ and $II_{\mathbf{D}}$ on the intruder's circumference. Based on the intruder's position and diameter, we discretized the intruder's circumference in several perimeter arcs. Each arc represented a point for which the values of $I_{\mathbf{D}}$ and $II_{\mathbf{D}}$ were evaluated and extracted. This method allowed us to determine how dilated or sheared the bulk was around the intruder.

2.3 Results

2.3.1 Vertical positions

The intruder's position (see Fig. 2.2) and bulk's velocity field were the first results obtained from the images. Near the bottom, at the beginning of the experiment, segregation was considerably slower than in upper regions. The closer the intruder got to the free surface, the faster it moved. The intruder generally showed a non-linear, depth-dependent segregation rate in all the experiments.

For all our results we used a size ratio defined as d_m/d_i , the media diameter divided by the intruder diameter. This definition provided a better fit to our results, than a d_i/d_m definition, and allowed us to contain its values within a well-defined range, i.e. between 0 and 1.

As shown in Fig. 2.2, the segregation rate $q \approx w_i = dz/dt$ increased as d_m/d_i tended to 0. These findings also held for experiments using larger medium diameters ($d_m = 8$ and 10 mm). A laddering, almost step-wise ascent, was observed in these cases, especially in the $d_m = 10$ mm medium experiments.

All the intruders demonstrated oscillatory vertical movement. Indeed, due to the plates' cyclic movement, the intruders moved upwards and downwards when the bulk was sheared. This movement could be interpreted as noise relative to an average vertical position during a cycle. Cyclical vertical movement was observed throughout the entire experiment and exhibited the same amplitude, independent of z . The magnitude of this movement did not change between experiments, even when different intruder diameters were used, as shown in Fig. 2.2. It is important to note that the bulk media were sheared cyclically, so the oscillatory vertical movement was the result of the setup.

An exponential law was fitted to the intruder position (dashed lines, see Fig.2.2)

$$z(t) = z_0 e^{b_i t}, \quad (2.4)$$

where z_0 is the initial vertical position of the intruder at the beginning of the experiment. Initially, we tried to fit a quadratic law $z(t) = at^2 + bt + c$, but then the segregation rate $q \approx dz/dt$ would have required a linear fit of the type $2at + b$, which was not the case for our experimental data. Based on the exponential fit, it was possible to collapse the results for the experiments with $d_m = 6$ mm (see Fig. 2.2(b)). This analysis was done under the supposition that the b_i parameters were a linear function of size ratio, i.e., $b_i = m_b(1 - d_m/d_i)$ in Fig. 2.2(a). The selected function was consistent with the no segregation condition, achieved when $d_m/d_i = 1$. To collapse our experimental data, we cleared t from Eq. (2.4) and wrote it as a function of z . We replaced the b_i coefficient by the regressed expression $b_i = m_b(1 - d_m/d_i)$ to obtain the function

$$F(z, z_0, m_b, d_m/d_i) = \frac{\ln z/z_0}{m_b(1 - d_m/d_i)}. \quad (2.5)$$

which scaled with t . The experimental results shown in Fig. 2.2 (b) are collapsed as function of t . Despite we were not able to plot results independent of an experimental time-scale, we show a function that represents well the size ratio dependence of the intruder's segregation.

Because no *kinetic sieving* mechanism was observed using the 2D shear cell configuration, we do not show any results on the percolation of small intruders through granular media made of large disks (for details on this see A.1). We observed that when a single smaller intruder was introduced into the cell, it did not percolate down through the bulk. Small disks moved erratically on top of the upper layer until they found lateral gaps generated by the plate roughness, which we considered biased. We removed these experiments from our results.

We estimated a final segregation time t_f for each experiment. This was defined as the time necessary for the intruder to rise from its initial position to the top layer of particles. We normalized time t by t_f and we normalized the vertical position z by the effective bulk height $h = 150$ mm. Figure 2.3(a) shows all the normalized experimental results. Experiments with

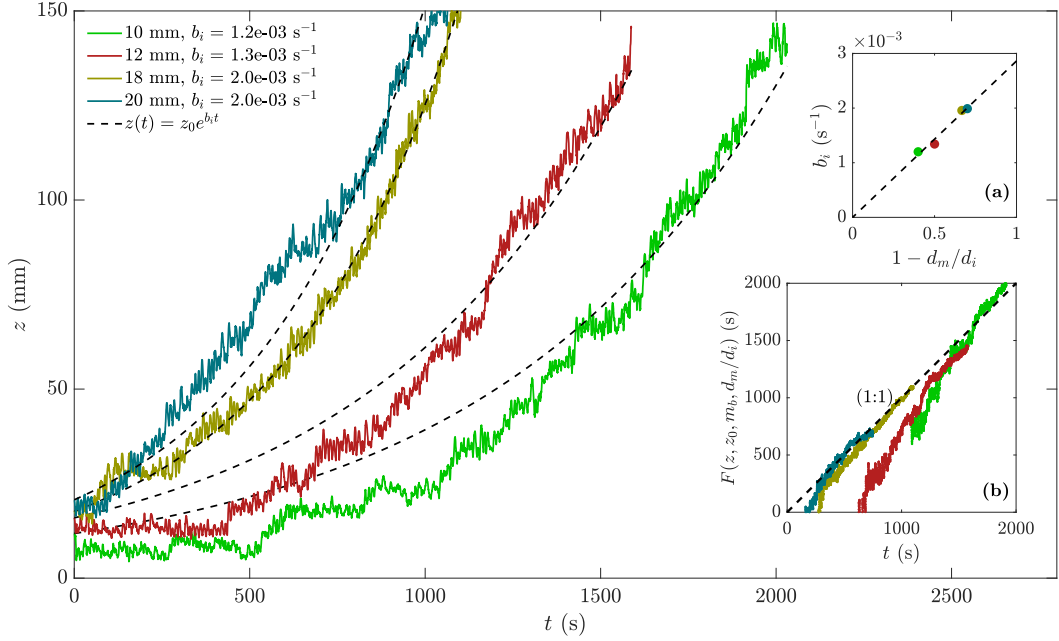


Figure 2.2 – Vertical position z as a function of time t for the intruders of $d_i = 10, 12, 18$ and 20 mm in the $d_m = 6$ mm medium experiments. The dashed lines (---) show the exponential fits (Eq. (2.4)) with the values of their respective b_i coefficients. (a) Linear fit for b_i as a function of $1 - d_m/d_i$ ($r^2 = 0.989$). (b) Experimental results collapsed using function F defined in Eq. (2.5), $m_b = 0.003$ correspond to the fitted parameter obtained from the linear regression of b_i in (a).

size ratios close to 0 (turquoise • and ♦) tended to a linear ascent, hence a nearly constant segregation rate. By contrast, experiments with size ratios close to 1 (green ♦ and red ★) showed strong nonlinear behavior.

To visualize all the experiments as a function of an averaged segregation rate \overline{w}_i , we defined this as the vertical distance h divided by t_f . This ratio neglects the nonlinear behavior shown in Fig. 2.2, so it is different from the instantaneous segregation rate $q \approx w_i$. Figure 2.3(b) plots \overline{w}_i as a function of $1 - d_i/d_m$. Experiments with size ratios close to 0 (turquoise • and ♦) exhibited the fastest averaged segregation rates, whereas experiments with size ratios close to 1 (green ♦ and red ★) exhibited the slowest averaged segregation rates. Figure 2.3(c) shows t_f as a function of $1 - d_m/d_i$. We did not observe a plateau for $t_f = f(1 - d_m/d_i)$, which would have indicated a constant relationship between the segregation rate and the size ratio. Neither did we find a local minimum t_f , which would have indicated a maximum segregation rate for a certain value of d_m/d_i . Our results showed a sharp increase of t_f when d_m/d_i tends to 1, especially for the experiment with $d_m/d_i = 0.833$. Despite, \overline{w}_i was expected to be non-monotonic for d_m/d_i , with a maximum around, e.g., 0.5 (Golick and Daniels, 2009), 0.58 ($d_l/d_s = 1.7$) Thornton et al. (2012) or 0.4 ($d_l/d_s = 2.5$) Thomas and D’Ortona (2018), it was not the case for our bi-dimensional experiments in the range of 0.3-0.833 ($d_l/d_s = 1.2$ -3.33).

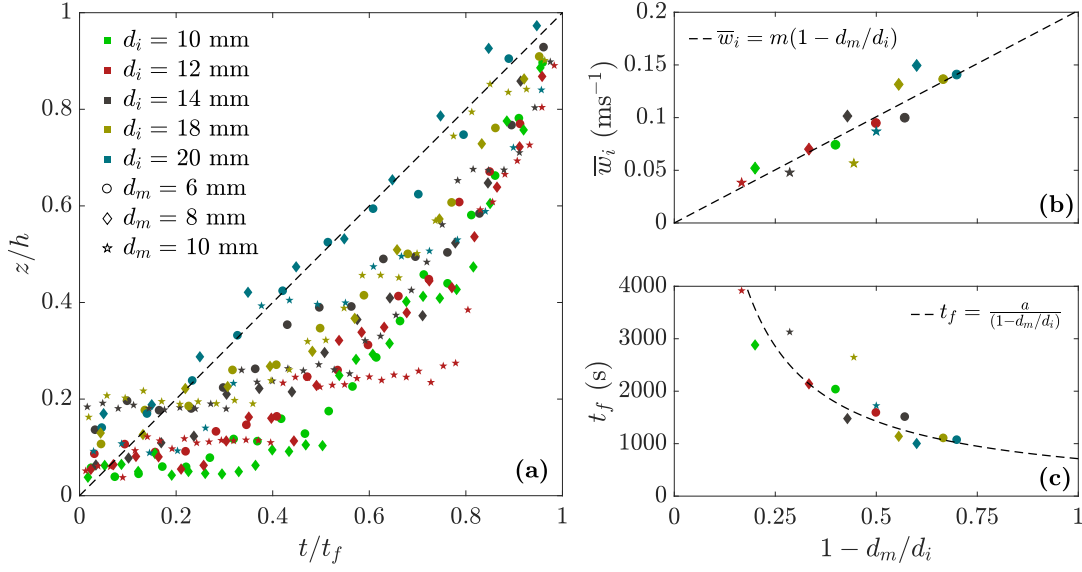


Figure 2.3 – (a) Normalized vertical position z/h as a function of normalized time t/t_f for all experiments. (b) Average vertical velocity $\bar{w}_i = h/t_f$ as a function of size ratio $1 - d_m/d_i$. The dashed line (---) in (b) represents a linear fit $\bar{w}_i = m(1 - d_m/d_i)$, with $m = 0.202 \text{ ms}^{-1}$ ($r^2 = 0.903$). (c) Final times for the segregation of intruders t_f as a function of size ratio $1 - d_m/d_i$. The dashed line (---) in (c) represents a curve fit using the expression $t_f = a/(1 - d_m/d_i)$, with $a = 713.83 \text{ s}$ ($r^2 = 0.9$).

2.3.2 Intruder rotation

Intruder rotation was observed as the bulk was sheared during each cycle. In some experiments the intruder rotated more, especially when intruder sizes were close to those of the media. Rotational movement did not tend towards any particular direction, and it was not necessarily synchronized with plate movement. In some cases we observed that the intruder upwards movement occurred simultaneously with its rotation.

Dot positions relative to the intruder's position are shown in Fig. 2.4. The red dot on the intruder's circumference is plotted relative to the intruder position. Figure 2.4 shows that intruder rotation was highest for size ratios close to 1. For example, the $d_i = 10 \text{ mm}$ intruder surrounded by $d_m = 6 \text{ mm}$ disks rotated around its center several times, which was reflected by the fact that the red dot's trajectory drew a complete circumference (Fig. 2.4 - top row, left-hand panel). Whereas smaller intruders completed several revolutions, larger intruders sometimes could not even complete one. A $d_i = 20 \text{ mm}$ intruder surrounded by $d_m = 6 \text{ mm}$ disks barely rotated. In this case the red dot was never oriented downwards or to the left of the intruder's center (Fig. 2.4 - top row, right-hand panel). Experiments using the $d_m = 10 \text{ mm}$ intruder showed the same tendency with one difference. In comparison, the same $d_i = 20 \text{ mm}$ intruder dot covered more of the circumference: hence this behavior was size-ratio dependent. These results indicated that in experiments with d_m/d_i closer to 1, segregation relied much

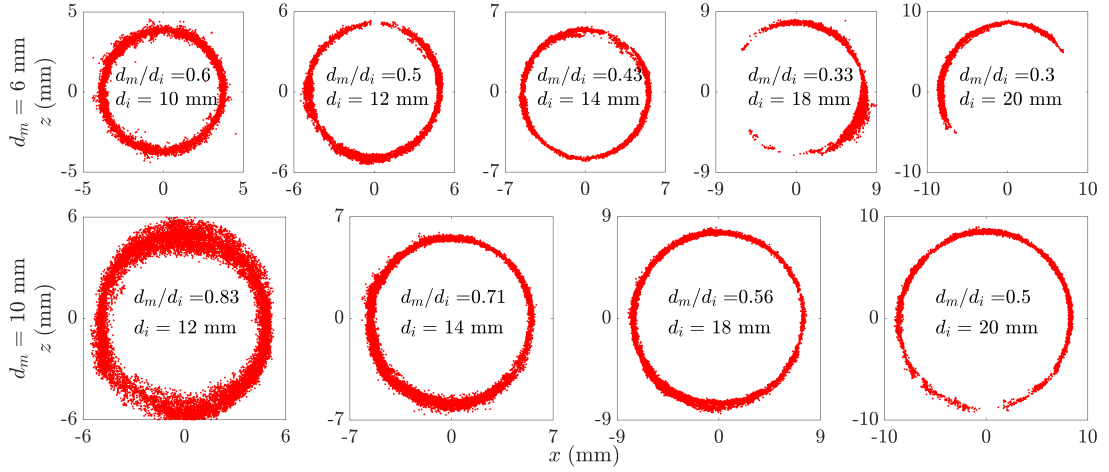


Figure 2.4 – Dot positions relative to the intruder's position. Top row (left to right): experiments using a $d_m = 6$ mm medium, with $d_i = 10, 12, 14, 18$ and 20 mm intruders. Bottom row (left to right): experiments using a $d_m = 10$ mm medium, with $d_i = 12, 14, 18$ and 20 mm intruders.

more on rotation. The less active rotation observed in experiments with $d_m/d_i < 0.5$ suggested that they relied on other mechanisms to segregate. Results in Fig. 2.4 are for the whole runtime of each experiment, a duration that was quite different and dependent on the size of the intruder as seen in §2.3.1. For shorter time intervals, for example the duration of the shortest experiment, the trend is preserved. Smaller intruders rotated more than larger intruders during equal time intervals.

We tracked these dots through time to measure rotation magnitudes. As explained in §2.2.2 we estimated the intruder's angular velocity Ω_i . Figure 2.5 shows that Ω_i was slightly correlated to vertical velocity $w_i = dz/dt$ which approximates to the segregation rate q . Another interesting feature was the increasing values of Ω_i as intruders rose to the surface. This increment was especially relevant for size ratios tending to unity as seen in Fig. 2.5, where we saw higher magnitudes for Ω_i and a tendency for even higher Ω_i values as the intruder approached the free surface. We suspect that the higher Ω_i values reached at the end of the experiment were a consequence of lower local confinement.

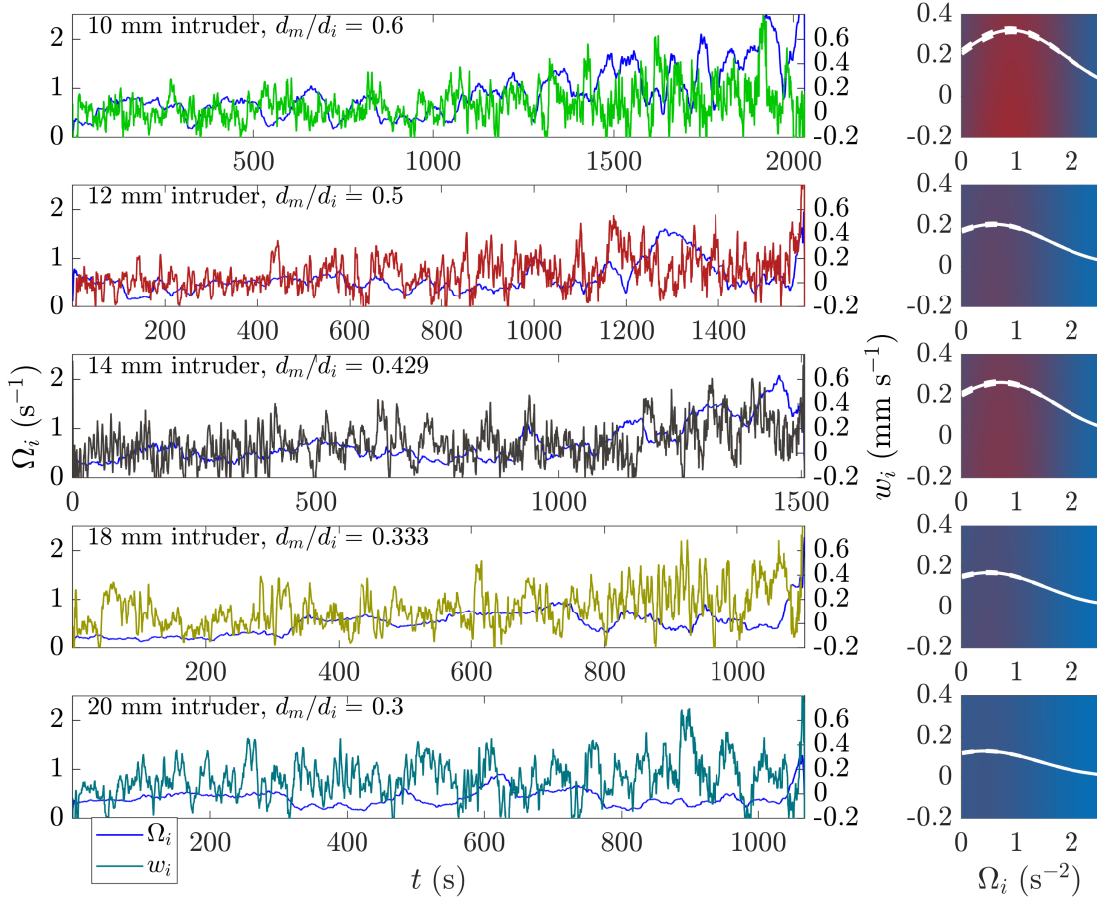


Figure 2.5 – Left column: intruders' angular acceleration Ω_i (left axis - blue line) and vertical velocities w_i (right axis, different colors) as a function of time t for experiments using the $d_m = 6$ mm medium and intruders of diameters $d_i = 10, 12, 14, 18$ and 20 mm (size ratios $d_m/d_i = 0.6, 0.5, 0.429, 0.33$ and 0.3). Right column: probability of w_i given that Ω_i , $P(w_i|\Omega_i)$. Red tones indicate a higher probability, with a maximum value of 0.4 , and blue tones indicate a lower probability, with minimum value of 0 . The continuous white line draws the mean values and the dashed white lines draw the mean values plus and minus standard deviations.

To illustrate the link between rotation and segregation, Fig. 2.5 plots their conditional probabilities $P(w_i|\Omega_i)$. As detailed in §2.2.2, $P(w_i|\Omega_i)$ expresses the probability that the intruder moved vertically upwards given that it rotated (Fig. 2.5 - right column). Experiments with $d_m/d_i > 0.4$ indicate higher probabilities that the intruder segregated given that it had rotated. Conversely, when $d_m/d_i < 0.4$, probabilities that the intruder segregated given it had rotated were lower. For each run, the probabilities of having a certain Ω_i value were averaged and plotted (Fig. 2.5 - white lines over colormaps). These averages and deviations were calculated to highlight the magnitude differences between runs with different size ratios. These results confirmed that as size ratios approach to 0 , intruders have lower probabilities of segregating

given that they rotated, and their rotation was weaker than that observed for size ratios tending to 1.

Figure 2.5 shows that, in general, Ω_i showed greater variability for $d_m/d_i > 0.4$ experiments. The experiment with $d_m/d_i = 0.3$ displayed the highest mean values for rotation, with a maximum at $\Omega_i \sim 2.5 \text{ s}^{-1}$. For the rest of the experiments, their maximum values for Ω_i decreased as size ratio decreased to 0, as well as their conditional probabilities.

2.3.3 Strain rate tensor invariants

The first and second invariants of the strain rate tensor were calculated according to §2.2.3. A field of each invariant was obtained for each experimental time step. Since we also knew the position of the intruder's circumference, we extracted the values of I_D and II_D around the intruder's circumference. As a result, the strain-rate tensor invariants I_{D_i} and II_{D_i} along the intruder's circumference can be plotted as functions of the intruder's arc angle ϕ_i . This angle was measured counter-clockwise from the horizontal direction towards the right of the cell (3 o'clock). To represent the experimental results of I_{D_i} and II_{D_i} , we took their time-averaged values over the entire experiment.

Figure 2.6 shows the strain rate tensor invariants around the intruder's circumference, using both cartesian and polar coordinates (Fig. 2.6 - left and right column, respectively). In general, the mean values for both invariants depended on the size ratio. A second general observation was that I_{D_i} and II_{D_i} were greatest on the upper half of the intruder's circumference, in accordance with the observed upward movement. The majority of the experiments showed maximum values at $\pi/2$ and minimum values at $3\pi/2$ for both invariants. In average, greater values are found on the upper half the intruder and smaller values are found on its lower half. These results showed that the intruder moved towards regions where I_{D_i} and II_{D_i} were greater, thus to the free surface.

Dilation I_{D_i} tended to be positive between 0 and π and negative elsewhere (contraction). For $d_m/d_i = 0.833$, the arc where $I_{D_i} > 0$ is particularly narrow (between $\pi/8$ and $3\pi/4$). This result suggests that for size ratios close to 1, gap formation was limited due to weak size heterogeneity. On the contrary, for $d_m/d_i = 0.3$, I_{D_i} is positive almost anywhere around the intruder's circumference. Grain movement creates dilation and segregation is enhanced. This grain movement resulted in faster intruder velocity, a result shown in Fig. 2.3(b). The contraction measured below the intruder, explains why large particles had difficulties to move to the cell's bottom.

Shear-rate magnitudes for each experiment depended on d_m/d_i as well. By definition, the values of II_{D_i} were always positive, with its highest values observed between 0 and π , and its local maximum also at $\pi/2$. Surprisingly, size ratios close to 1 showed higher II_{D_i} values. However, this observation was consistent with the argument that rotation and angular velocity play a role in the segregation of large particles. Shear rate is related to angular deformation,

which was observed experimentally by intruder rotation. The magnitudes of II_{D_i} are of the same order of magnitude as the average external shear rate $\bar{\gamma}_e = 2.67 \times 10^{-2} \text{ s}^{-1}$ (Eq. 2.1). Even though all the experiments shared the same externally imposed shear rate, II_{D_i} was locally distributed around the intruder's circumference at values ranging between approximately 1.8×10^{-2} and $2 \times 10^{-2} \text{ s}^{-1}$ (Fig. 2.6). Also, the mean values of II_{D_i} around the intruder's circumference are dependent on the size ratio. These mean values show differences of $6 \times 10^{-3} \text{ s}^{-1}$ between the experiments with size ratios of 0.833 and 0.3 (see Fig. 2.6 - red ★ and turquoise •, respectively).

Figure 2.6 also presents two intermediate cases with $d_m/d_i = 0.5$ for particle diameters of 6 and 10 mm, and intruders of 12 and 20 mm, respectively. Even though the size ratios are the same, the values calculated for I_{D_i} and II_{D_i} were different, with mean differences of 1×10^{-3} and $2 \times 10^{-4} \text{ s}^{-1}$, respectively. We think these differences were due to the plate roughness and slightly different W/d_m values.

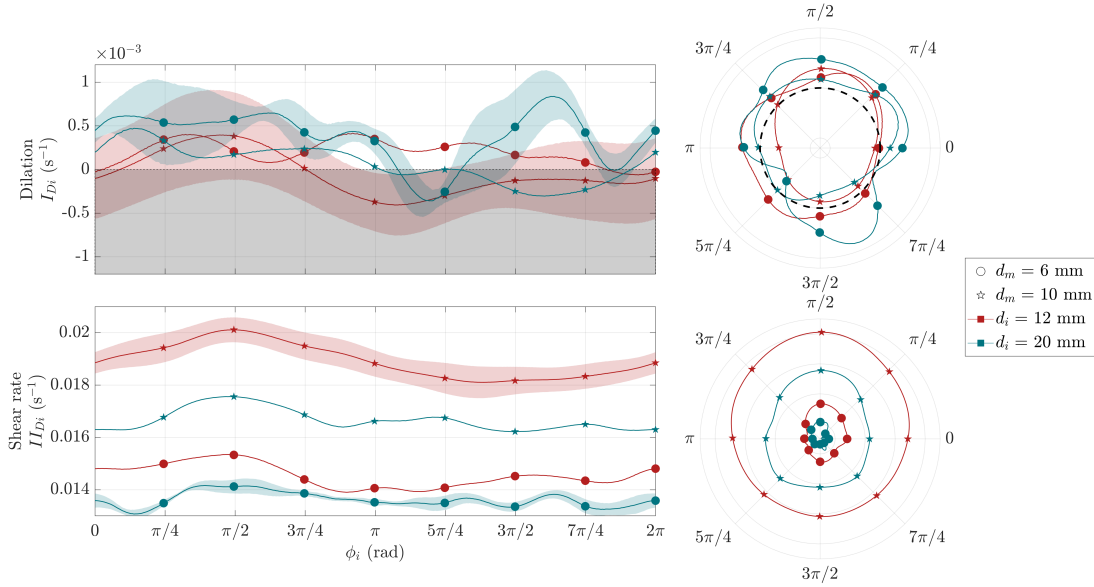


Figure 2.6 – Left column. Time-averaged strain rate-tensor invariants for dilation I_{D_i} (top row) and shear rate II_{D_i} (bottom row), around the intruder's circumference ϕ_i , with the angle measured counter-clockwise from the horizontal direction towards the right of the cell (3 o'clock). Colored areas represent values and their standard deviation. The gray area represents contraction. Right column. Polar plots of the same strain rate-tensor invariants for the experiments with $d_m = 6$ (•) and 10 (★) mm media, and $d_i = 12$ (red) and 20 (turquoise) intruders. Standard deviations were not plotted for all experiments for visualization purposes.

2.3.4 Segregation mechanism

Even though the *squeeze expulsion* mechanism was largely well-described by Savage and Lun (1988), they provided no clear role for the particles' size ratio. Our results in §2.3 suggest that

segregation is caused by a combination of dilation and rotation that depends on size ratio d_m/d_i . Dilation was predominant for d_m/d_i values closer to zero and segregation rates were faster in these cases. Dilation faded as d_m/d_i increased, but segregation still happened. For d_m/d_i tending to 1, rotation and shear rate became predominant, and they were significant for segregation. For $d_m/d_i < 0.5$, segregation rates were considerably higher; thus, dilation was a much more effective sub-mechanism for segregation than rotation was. Nonetheless, rotation's contribution for relatively smaller intruders is still key for their segregation.

Two processes occur in an initially dense granular material that undergoes shear (see Fig. 2.7 - first figure panels in both rows):

- If dilation I_D around the intruder is large enough, surrounding particles entrain below it. This small-particle entrainment may lift the intruder up, presumably through normal stress redistribution. This occurrence of entrainment does not depend solely on dilation. All our experiments were subjected to the same shear rate II_D and effective bulk height h , yet segregation rates differed (Fig. 2.3). Therefore, the second variable controlling the entrainment should be d_m/d_i . When $d_m/d_i < 0.5$ it becomes easier for disks surrounding the intruder to entrain. For d_m/d_i close to unity, entrainment is less frequent, due to weak gap generation, and the intruder usually remains in its place.
- Shear-induced dilation redistributes forces around the intruder. As a result, the intruder may become interlocked with its neighbors. Normal stresses transmitted through the intruder's neighbors create a force network that restrains the intruder's movement. When shear continues to be applied, the interlocked particles move conjointly around a pivot below them. Similarly to the first process, this rotational movement depends on d_m/d_i . Our results indicated higher rotation, a greater probability $P(w_i|\alpha_i)$, and higher local shear rates II_{Di} for $d_m/d_i > 0.5$ (Fig. 2.5). A size ratio close to 1 indicates that interlocking is likely to be occurring. It is plausible that slight size differences between the intruder and the medium require fewer surrounding particles to lock-in the intruder. However, our experiments showed that the probability of interlocking remains low. Therefore, the segregation caused by this process is slower and less effective than that caused by the first process.

2.4 Conclusions

A two-dimensional, oscillatory shear-cell was used to study the segregation of a large particle intruder through a medium of smaller particles. The intruder's position and rotation were measured and tracked over time. We found that the segregation rate was a non-linear function of time, dependent on the intruder's depth and the size ratio d_m/d_i . An increase in the size ratio decreased the segregation rate. Intruder rotation, quantified in terms of angular velocity, was found to be more frequent and intense, the closer the size ratio is to 1. We conclude that intruder rotation is a relevant mechanism in the segregation of large particles, in agreement

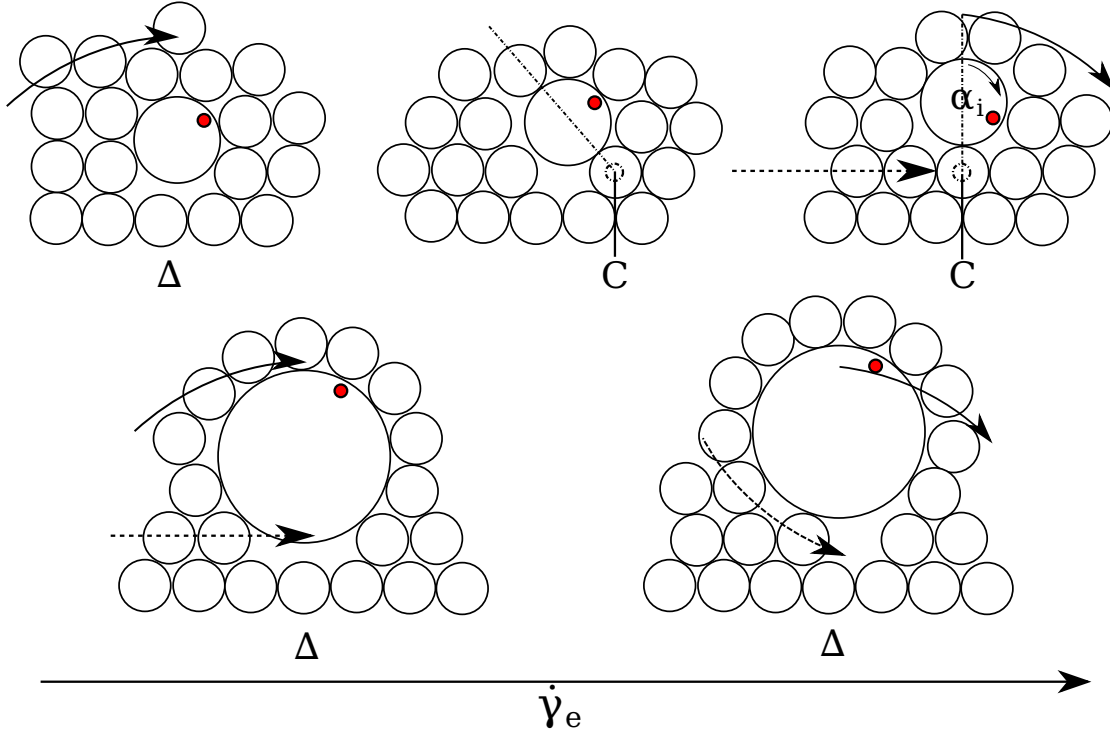


Figure 2.7 – Scaled schema of the segregation of a single large intruder of $d_i = 10$ (top row) and 20 (bottom row) mm under the action of an external shear rate $\dot{\gamma}_e$. Top row. Rotation-based mechanism. The bulk medium dilates with a magnitude Δ (left panel) and creates a contact network that locks-in the intruder (middle panel). Further shear generates intruder rotation (represented by α_i) around the pivotal point C (right panel). Bottom row. Dilation-based mechanism. The bulk medium dilates with a magnitude Δ (both panels), generating gaps for particles to slide beneath (right panel - dashed arrows).

with the proposition of Jing et al. (2017).

Using a different setup and flow configuration, we found the same segregation behavior as that presented by several authors (Golick and Daniels, 2009; Wiederseiner et al., 2011b; Guillard et al., 2016), large particles segregated, predominantly, towards regions where dilation was greater. Complementarily, we found that for size ratios close to 1 shear rate becomes a relevant variable for segregation. The shear-rate gradient causes the intruder to rotate, resulting in its segregation; subsequently, a higher shear-rate produces a faster segregation of the intruder. Even though we did not present stress measurements, we presented a plausible explanation for the role of the local shear-stress gradient in the segregation of large particles.

Based on the observations presented here, we have suggested a detailed description of the *squeeze expulsion* mechanism, the variables and the processes affecting it. The first process is strongly dependent on dilation, whereas the second depends on rotation, i.e., represented by the shear rate. Frustration of the rotation-based process depends on surrounding interparticle contacts, which was observed for $d_m/d_i < 0.5$ where the intruder needed more particles in

close contact to interlock. We proposed that the occurrence of these processes, although independent of each other, are highly dependent on the size ratio.

Supplementary images for segregation mechanisms

To better illustrate the segregation mechanisms for large particle segregation, two image sequences from experiments are shown in this section.

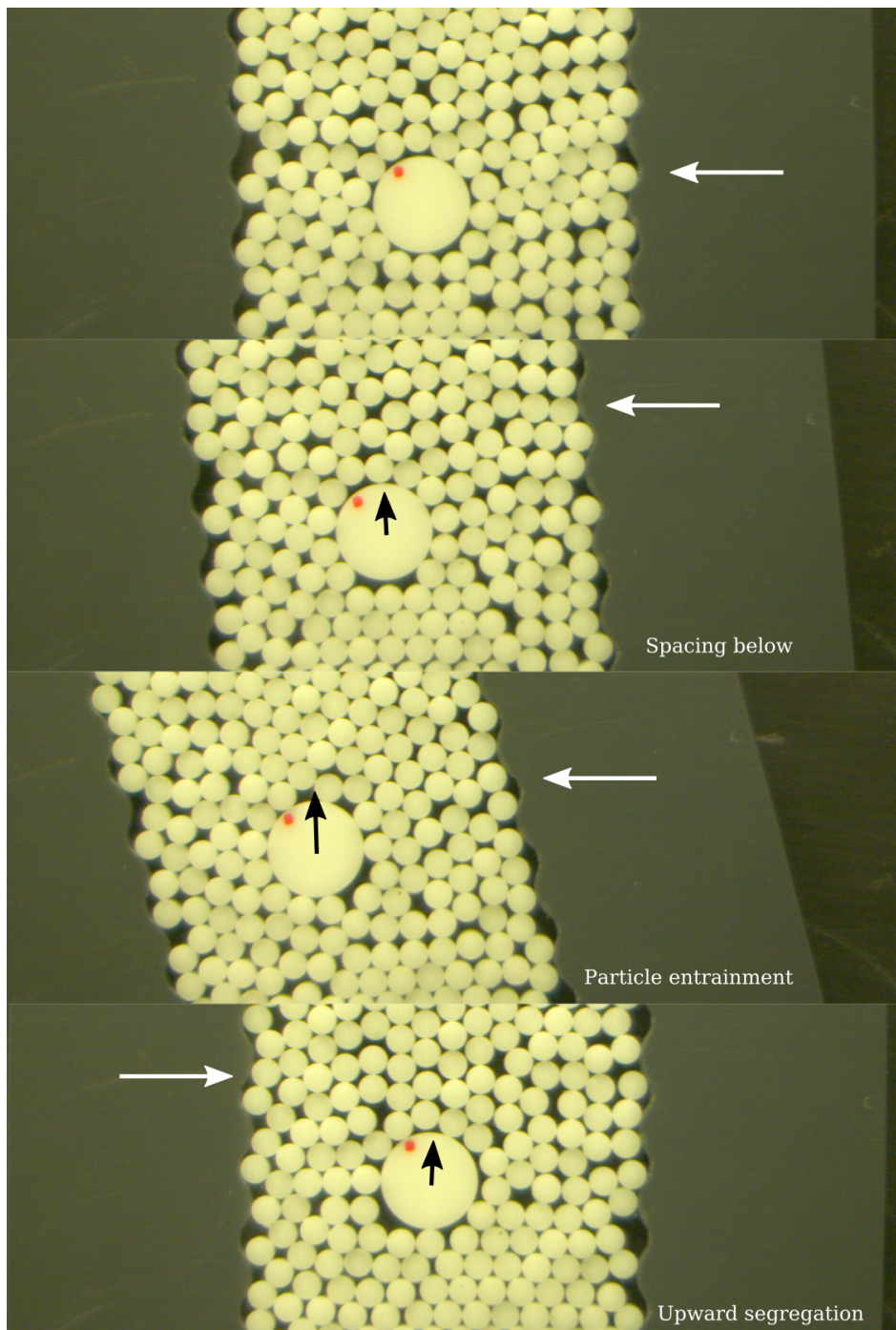


Figure 2.8 – Image sequence of the dilation-dominant segregation mechanism. A 20 mm intruder segregates upwards due to the squeezing action exerted by the surrounding 6 mm particles, which entrain below the intruder.

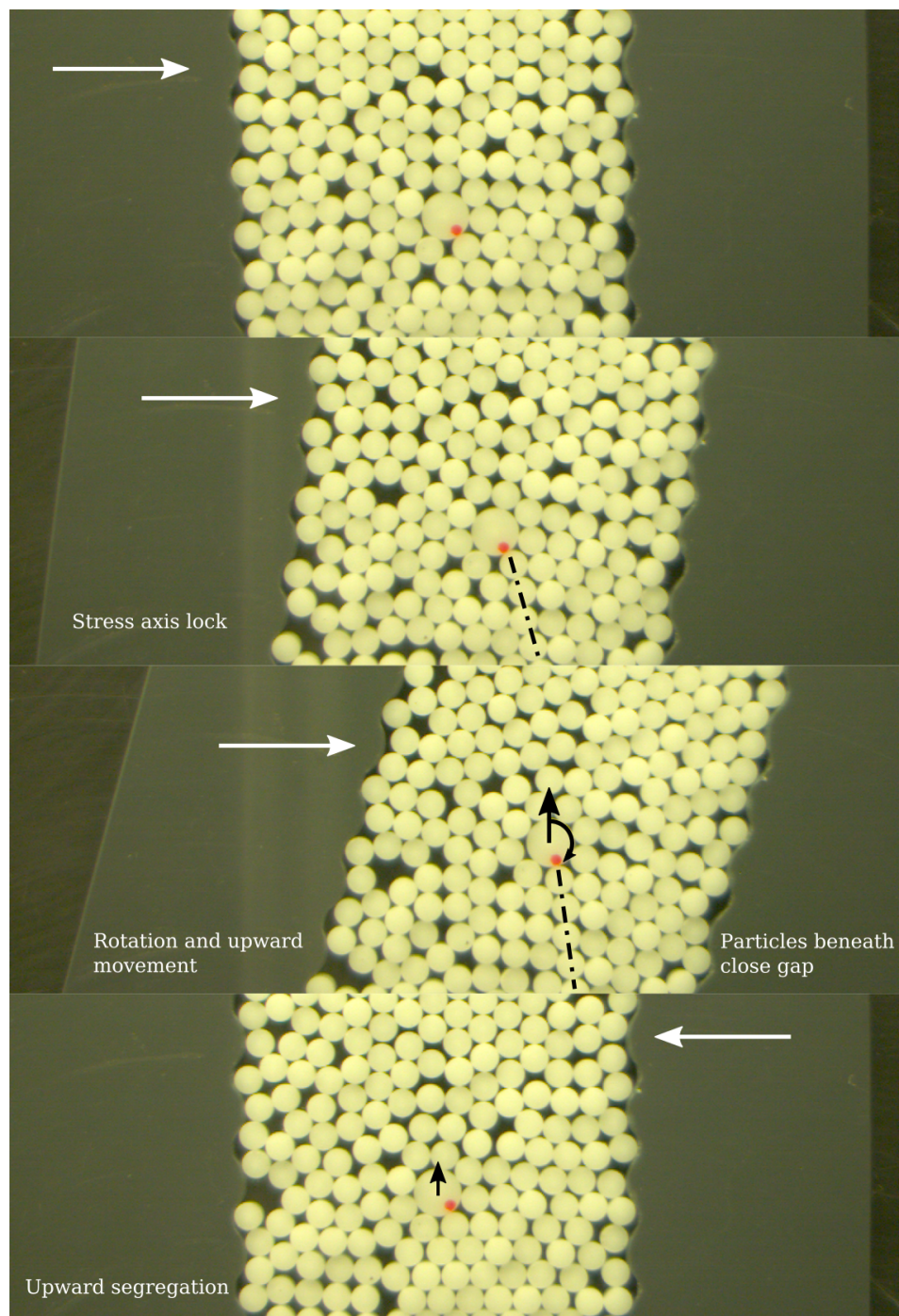


Figure 2.9 – Image sequence of the rotation-dominant segregation mechanism. A 10 mm intruder segregates upwards due to the interlocking of surrounding 6 mm particles that create a stress axis that locks and rotates the intruder, allowing the entrainment of the surrounding particles.

3 An experimental scaling law for particle-size segregation in dense granular flows

Tomás Trehela¹, Christophe Ancey¹, and J. M. N. T. Gray²

¹ Laboratory of Environmental Hydraulics, École Polytechnique Fédérale de Lausanne, Lausanne, Switzerland.

² Department of Mathematics and Manchester Centre for Nonlinear Dynamics, University of Manchester, Oxford Road, Manchester M13 9PL, UK.

Under revision in *Journal of Fluid Mechanics*.

Doctoral candidate's contribution

The experiments, analyses, figures and photos were done by the candidate, with the exception of those in section §3.7. The scaling and final fitting analysis was done co-jointly by Prof. Nico Gray and the candidate. The first draft of this chapter was written by the candidate, but it did not include the scaling analysis, the introduction and the comparison to van der Vaart et al.'s (2015) data. The determination of the functional dependence of the segregation rate came from discussions between Prof. Gray and the candidate during Prof. Gray's visits to EPFL and a visit of the candidate to the University of Manchester.

Abstract

Particles of differing sizes are notoriously prone to segregation in shear driven flows under the action of gravity. This has important implications in many industrial processes, where particle-size segregation can lead to reduced product quality, flow problems and longer product development and start-up times. Particle-size segregation also readily occurs in many hazardous geophysical mass flows (such as snow avalanches, debris flows and volcanic pyroclastic flows) and can lead to the formation of destructive bouldery flow fronts and significantly longer run-outs. Although general theories exist to model particle-size-segregation, the detailed functional dependence of the segregation flux on the shear-rate, gravity, pressure,

particle concentration, grain-size and grain-size ratio is still not known. This paper describes refractive-index matched oscillatory shear-cell experiments that shed light into the segregation velocity in the two extreme cases of (i) a single large intruder rising up through a matrix of smaller grains, and (ii) a single small intruder percolating down through a matrix of large particles. Despite the sometimes markedly different time scales for segregation in these two situations, a unifying scaling law has been found that is able to collapse all the experimental data over a wide range of shear rates and grain-size ratios. The resulting functional form is easily generalizable to intermediate concentrations, suggesting that this empirical law captures the fundamental processes that determine the segregation velocity in general.

3.1 Introduction

Shallow granular free-surface flows (or granular avalanches) are one of the most common particle transport mechanisms in industrial bulk solids handling processes. They form in chute flows (Savage and Hutter, 1989; Gray et al., 1999), as well as in thin fluid-like layers at the free-surface of heaps (Williams, 1968; Baxter et al., 1998; Fan et al., 2012), silos (Bates, 1997; Schulze, 2008; Liu et al., 2019; Isner et al., 2020) and rotating tumblers (Gray and Hutter, 1997; Hill et al., 1999; Khakhar et al., 2003; Schlick et al., 2015; Gilberg and Steiner, 2020). These high density, gravity driven, shear flows are highly efficient at segregating particles by size. Despite many years of research, particle size segregation continues to present considerable practical problems in many industrial processes (Johanson, 1978; Isner et al., 2020). Sometimes the segregation is useful, such as in the mining industry (Wills, 1979). However, in the bulk chemical, pharmaceutical, agricultural and food industries it is the single biggest cause of product non-uniformity (Bates, 1997). This can lead to complete batches having to be discarded at significant cost. In addition, the evolving local particle size-distribution may feedback on the rheology of the bulk flow and cause unexpected flow problems (Pouliquen et al., 1997; Pouliquen and Vallance, 1999; Baker et al., 2016) that are still poorly understood. Segregation induced frictional feedback is also thought to play a vital part in the formation of bouldery flow fronts (Pierson, 1986; Denissen et al., 2019) and static levees (Iverson and Vallance, 2001; Baker et al., 2016; Rocha et al., 2019) in hazardous geophysical mass flows (such as snow avalanches, debris flows and pyroclastic flows), which can significantly enhance their run-out.

In the avalanching region of these industrial and geophysical flows, small grains percolate towards the base of the shearing layer and large grains rise towards the free-surface. Complex interactions between the shear flow and an underlying static or slowly moving region of grains, can lead to the development of amazing patterns in the deposit (e.g. Williams, 1968; Gray and Hutter, 1997; Baxter et al., 1998; Hill et al., 1999). However, for a steady-state flow on a fixed base, an inversely graded particle size distribution develops, with the large particles concentrated at the top of the flow and the finer grains concentrated near the base. The segregation occurs due to the combination of two processes; kinetic sieving (Middleton, 1970) and squeeze expulsion (Savage and Lun, 1988). Essentially as the layers of grains shear past one another they act as random fluctuating sieves, which preferentially allow small particles

to percolate downwards into gaps that open up beneath them (known as kinetic sieving), while all particles are squeezed upwards with equal probability (known as squeeze expulsion), which maintains an approximately constant solids volume fraction (MiDi, 2004). This has been termed gravity driven segregation (Gray, 2018) for short, to reflect the fact that gravity is fundamental to the smaller grains falling into the gaps between the larger grains, and therefore setting the direction for segregation. The grains also diffuse within the shear flow, which produces a smoothly varying inversely graded particle-size distribution at steady-state (with the large grains concentrated on top of the fines) rather than being sharply segregated.

The earliest continuum model for bi-disperse particle segregation was developed by Bridgwater et al. (1985). It consisted of a spatially one-dimensional time-dependent advection-diffusion equation, with a shear rate dependent segregation flux that shut off when the species concentration reached zero and one hundred percent. The key elements of this theory are still present in more recent multi-dimensional models that use either a quadratic (e.g. Savage and Lun, 1988; Dolgunin and Ukolov, 1995; Khakhar et al., 2003; Gray and Thornton, 2005; Thornton et al., 2006; Gray and Chugunov, 2006; Wiedersseiner et al., 2011b; Gray and Ancey, 2011; Tripathi and Khakhar, 2013; Tunuguntla et al., 2014; Gajjar and Gray, 2014; Schlick et al., 2015; Gray and Ancey, 2015; Xiao et al., 2016; Liu et al., 2019; Gilberg and Steiner, 2020) or cubic (e.g. Gajjar and Gray, 2014; van der Vaart et al., 2015; Jones et al., 2018) small particle concentration dependence in the segregation flux.

Wiedersseiner et al. (2011b) filmed the spatially two-dimensional steady state segregation of large black and small white particles through the side wall of a chute. By using a calibration curve, they were able to determine the local small particle concentrations as the grains segregated from a sharply segregated normally graded inflow (with all the small particles on top of the large grains) to a fully developed inversely graded steady state. Wiedersseiner et al. (2011b) showed that by using the measured downslope velocity, and choosing appropriate constant values for the segregation velocity magnitude and the diffusivity, it was possible to accurately model the spatial development of the concentration using Gray and Chugunov's (2006) theory.

Thornton et al. (2012) performed Discrete Particle Model (DPM) simulations in a periodic box using bi-disperse mixtures of particles with different size ratios. The final steady-state numerical results were then compared to the exact steady-state solution of Gray and Chugunov (2006). In this solution the length scale for the transition between high concentrations of large and small particles, is inversely proportional to the Péclet number for segregation. This is defined as the flow thickness times the segregation velocity magnitude divided by the diffusivity. Thornton et al. (2012) showed that the Péclet number increased with increasing grain-size ratio and peaked at a value close to 8 at a grain-size ratio just below two. However, Wiedersseiner et al. (2011b) found experimental values of the Péclet number between 11 and 19 for similar size ratios. This discrepancy may be due to the coupling with the bulk velocity, which was an exponential profile in Wiedersseiner et al.'s (2011b) experiments, but will be Bagnold-like (Silbert et al., 2001) in Thornton et al.'s (2012) simulations, since they are not affected by sidewall friction.

In order to better visualize the segregation in experiments, van der Vaart et al. (2015) performed a series of refractive index matched particle-size segregation experiments in an oscillating shear box. This has the advantage that the shear-rate is independent of depth, and the flow field is explicitly prescribed rather than spontaneously developing in a chute flow. The experiment was stopped after each complete oscillation and the three-dimensional particle-size distribution was determined by scanning a laser sheet across the cell while taking a series of photographs. From this extremely detailed data, van der Vaart et al. (2015) showed that there was a fundamental asymmetry to particle size segregation. In particular, a single small intruder will percolate down through a matrix of large grains much faster than a single large intruder will rise up through a matrix of fines. This suggests that the segregation flux function is not quadratic, but has a more cubic-like dependence on the small particle concentration (Bridgwater et al., 1985; Gajjar and Gray, 2014; van der Vaart et al., 2015; Jones et al., 2018).

The annular shear cell experiments of Golick and Daniels (2009) also provide important insights into the functional dependence of the segregation flux. The experiment was driven by a moving bottom plate, but the top plate was also free to move vertically in response to the pressure generated during the flow. Their experiments showed that there were subtle packing effects, as a normally graded initial configuration mixed and then segregated into a final inversely graded steady state. The ability of the grains to pack tighter together in a shearing bi-disperse mixture caused the top plate to drop from its initial height, and then recover as the particles segregated again. Intriguingly, Golick and Daniels (2009) showed that when a weight was placed on the top plate the rate of segregation was dramatically decreased. This suggests that the segregation velocity magnitude is pressure and/or solids volume fraction dependent. This has been investigated further by Fry et al. (2019) using DPM simulations of a confined shear flow. Their simulations suggest that the percolation velocity, and hence the segregation velocity magnitude, is proportional to the reciprocal of the square root of the pressure. It follows that segregation is suppressed in Golick and Daniels's (2009) experiments, when a weight is applied, because the pressure reduces the segregation rate while having no effect on the diffusion.

A definitive form for the segregation flux function that makes sense of, and hopefully unifies, all the observations is still lacking. It is clear that it is dependent on the shear-rate (Bridgwater et al., 1985; Savage and Lun, 1988; May et al., 2010a; Fan et al., 2014), the pressure (Golick and Daniels, 2009; Fry et al., 2019), gravity (Vallance and Savage, 2000; Gray and Thornton, 2005; Gray et al., 2006; Fry et al., 2019), the mean particle size (Fry et al., 2019; Chassagne et al., 2020) and the particle size ratio (Savage and Lun, 1988; Gray and Thornton, 2005; Thornton et al., 2012; Fan et al., 2014), as well as that it has a non-quadratic concentration dependence (Bridgwater et al., 1985; Gajjar and Gray, 2014; van der Vaart et al., 2015; Jones et al., 2018). However, there may also be additional functional dependencies on the friction of the grains (Jing et al., 2017) and the evolving local solids volume fraction (Golick and Daniels, 2009; Gilberg and Steiner, 2020).

This paper aims to shed further light on the functional form of the segregation flux by using

refractive index matched shear cell experiments and dimensional analysis. §3.2 reviews the governing equations and explains the rationale behind studying the extreme end states of a single large, and a single small, intruder. §3.3 describes the experimental shear box and the refractive index matching technique. §3.4 uses dimensional analysis and a series of key observations to motivate a simple functional form for the flux. §3.5 and §3.6 compares the theoretical large and small intruder trajectories to those measured in experiment, for a wide range of shear rates and size ratios, and shows that the data can be collapsed using the same non-dimensional coefficients. §3.7 shows that the theory quantitatively matches van der Vaart et al.'s (2015) shear box experiments with a 50:50 mix of particles using the same non-dimensional coefficients and the simplest possible function to map between the size ratio dependence of the large and small intruders. §3.8 then concludes and makes some interesting observations about the functional form of the segregation flux that is implied by the theory.

3.2 Bidisperse particle-size segregation

3.2.1 Governing equations

Consider a mixture of large and small particles whose pore space is occupied by an interstitial fluid. Each of the constituents occupies a volume fraction $\Phi^v \in [0, 1]$ per unit mixture volume, where the constituent letters $v = l, s$ and f , refer to large particles, small particles and fluid, respectively. It is also possible to define volume fractions of large and small particles per unit granular volume

$$\phi^l = \frac{\Phi^l}{\Phi^l + \Phi^s}, \quad \phi^s = \frac{\Phi^s}{\Phi^l + \Phi^s}. \quad (3.1)$$

This is useful, because in many situations of practical interest the solids volume fraction $\Phi = \Phi^l + \Phi^s$ does not change very much (Silbert et al., 2001; MiDi, 2004) and can therefore be scaled out of the equations (Thornton et al., 2006). In this situation, the general form of the bidisperse segregation equations for the volume fractions (concentrations) of the large and small particles (see e.g. Gray, 2018) are

$$\frac{\partial \phi^l}{\partial t} + \nabla \cdot (\phi^l \mathbf{u}) - \nabla \cdot \left(f_{sl} \phi^l \phi^s \frac{\mathbf{g}}{|\mathbf{g}|} \right) = \nabla \cdot (\mathcal{D}_{sl} \nabla \phi^l), \quad (3.2)$$

$$\frac{\partial \phi^s}{\partial t} + \nabla \cdot (\phi^s \mathbf{u}) + \nabla \cdot \left(f_{sl} \phi^s \phi^l \frac{\mathbf{g}}{|\mathbf{g}|} \right) = \nabla \cdot (\mathcal{D}_{sl} \nabla \phi^s), \quad (3.3)$$

respectively, where \mathbf{u} is the bulk granular velocity field, f_{sl} is the segregation velocity magnitude, \mathbf{g} is the gravitational acceleration vector and \mathcal{D}_{sl} is the diffusivity of the large and small particles. Since by definition the concentration of large and small particles sum to unity

$$\phi^l + \phi^s = 1, \quad (3.4)$$

the sum of equations (3.2) and (3.3) imply that the bulk velocity field is incompressible

$$\nabla \cdot \mathbf{u} = 0. \quad (3.5)$$

This is reasonable leading order approximation that is made in the incompressible $\mu(I)$ -rheology (MiDi, 2004; Jop et al., 2006; Barker and Gray, 2017) for example. It should be noted, however, that in reality there is some compressibility and indeed compressibility is needed to make the rheology thermodynamically consistent (Goddard and Lee, 2018) and well-posed (Barker and Gray, 2017; Schaeffer et al., 2019). In this paper, however, the solids volume fraction is assumed to be equal to a constant uniform value of $\Phi = 0.6$.

3.2.2 Segregation fluxes and velocities

In (3.2) and (3.3) the large and small particle segregation fluxes are

$$\mathbf{F}^l = -f_{sl}\phi^l\phi^s \frac{\mathbf{g}}{|\mathbf{g}|}, \quad (3.6)$$

$$\mathbf{F}^s = +f_{sl}\phi^s\phi^l \frac{\mathbf{g}}{|\mathbf{g}|}, \quad (3.7)$$

respectively. These are aligned with the direction of gravitational acceleration \mathbf{g} to reflect the fact that the downward percolation of small particles due to kinetic sieving is a gravity driven process. In order to maintain bulk incompressibility there is a net reverse flow of large particles towards the surface due to squeeze expulsion. In the absence of diffusion the segregation velocity of the large and small particles relative to the bulk flow are

$$\hat{\mathbf{u}}^l = \mathbf{u}^l - \mathbf{u} = -f_{sl}\phi^s \frac{\mathbf{g}}{|\mathbf{g}|}, \quad (3.8)$$

$$\hat{\mathbf{u}}^s = \mathbf{u}^s - \mathbf{u} = +f_{sl}\phi^l \frac{\mathbf{g}}{|\mathbf{g}|}, \quad (3.9)$$

respectively. The summation constraint (3.4) implies that the segregation fluxes (3.6)–(3.7) are zero when either of the phases is in a pure phase. If f_{sl} is independent of ϕ^s and ϕ^l then (3.4) implies that the large particle segregation flux is quadratic in ϕ^s and is symmetric about $\phi^s = 1/2$. Equation (3.8) shows that the corresponding large particle segregation velocity is linear in ϕ^s and hence implies that the maximum segregation velocity is equal to f_{sl} and is attained when there is a single large grain at concentration $\phi^s = 1^-$ (note the superscript minus is used to show that the concentration is not 100% small particles, i.e. there is a large intruder, but it does not significantly change the local concentration from unity). Similarly, the small particle segregation velocity is linear in ϕ^l and the maximum segregation velocity equals $-f_{sl}$ and is attained when there is a single small grain at concentration $\phi^s = 0^+$. The quadratic large particle segregation flux function and the associated linear segregation velocities are plotted in figure 3.1(a,b).

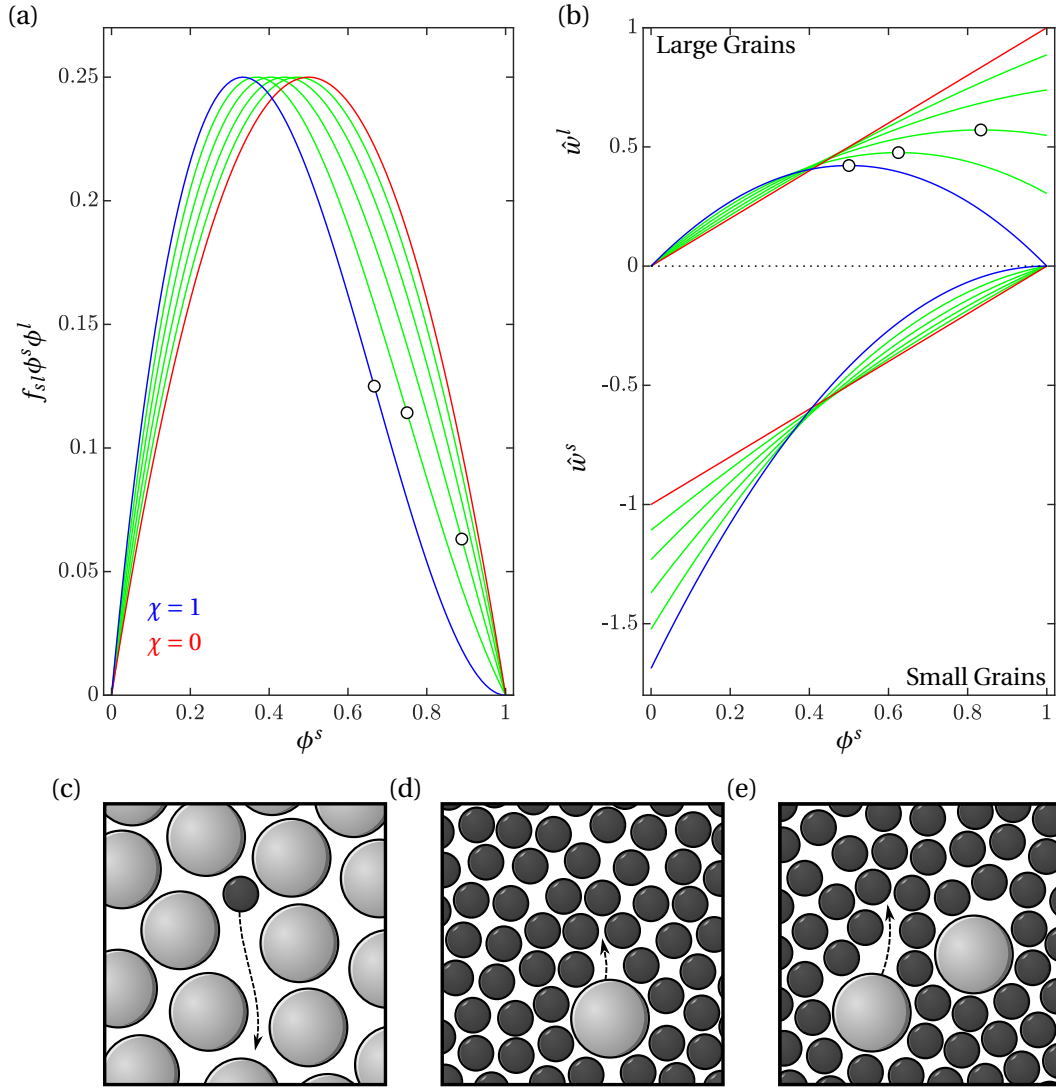


Figure 3.1 – (a) Segregation flux functions and (b) the large and small particle segregation velocities as a function of the small particle concentration ϕ^s (adapted from Gajjar and Gray, 2014; Gray, 2018). These assume that $f_{ls} = A_\chi(1 - \chi\phi^s)$, where $\chi \in [0, 1]$ and A_χ is a normalization factor to give all the flux functions the same amplitude as the quadratic flux when $\chi = 0$ (red lines). The blue lines show the cubic flux model of Bridgwater et al. (1985) for $\chi = 1$ and the green lines show the intermediate cases when $\chi = 0.2, 0.4, 0.6, 0.8$. For $\chi \in [1/2, 1]$ these develop an inflection point at $\phi_{\text{inf}}^s = (1 + \chi)/(3\chi)$ (circular markers a) and a group of large particles rise fastest at $\phi_{\text{crit}}^s = 1/(2\chi)$ (circular markers b). Sketches showing (c) the rapid percolation of a single small intruder in a matrix of large grains, (d) the slow rise of a single large particle in a matrix of fine and (e) the faster rise of a group of large particles at intermediate concentrations for a sufficiently skewed flux function.

Using shear box experiments van der Vaart et al. (2015) showed that there was an underlying asymmetry to the particle-size segregation, i.e. a single small particle percolating down

through a matrix of large particles moves much faster than a single large particle being squeezed up through a matrix of fines. This is illustrated schematically in figure 3.1(c,d) and is not captured in the simple quadratic flux model. Gajjar and Gray (2014) showed that this asymmetry could, however, be captured by skewing the peak segregation flux towards smaller concentrations of fine grains, as illustrated for a cubic flux function in figure 3.1(a). As the peak of the large particle segregation flux moves to the left, the maximum downward small particle segregation velocity (at $\phi^s = 0^+$) is progressively increased even though the maximum amplitude of the flux function stays the same. As the cubic flux curves become skewed, the large particle segregation velocity at concentration $\phi^s = 1^-$ is progressively diminished below that of the quadratic flux model. Moreover, as the skewness parameter χ rises above one half, an inflection point develops in the flux function and the maximum segregation velocity of large particles no longer occurs at $\phi^s = 1^-$, but at an intermediate concentration ϕ^s within the range $[1/2, 1]$. As a result a group of large particles will rise faster than an individual large intruder as illustrated schematically in figure 3.1(d,e).

The theory shows that studying (i) a large intruder being squeezed up through a matrix of fine particles and (ii) a small intruder percolating down through a matrix of large grains can yield a considerable amount of information about the shape of the segregation flux function. A series of single intruder refractive index matched shear box experiments have therefore been performed in this paper.

3.3 Refractive index matched shear box experiments

3.3.1 Experimental apparatus

The shear box apparatus is shown in figure 3.2(a). It consists of two polyvinyl chloride (PVC) rough lateral side plates that are able to pivot about two transverse steel rods, that are located at their centres and bolted to glass panes at the front and back of the shear box. The top ends of the PVC plates are attached to a steel bar that keeps the plates parallel and connects them to a horizontally moving plunger driven by a rotational motor. The bottom of the sheared domain is set by another PVC plate of length $L = 4.5$ cm that is free to move horizontally within slotted grooves in the transparent front and back walls. As the top of the PVC side plates are driven backwards and forwards the plates pivot about their centres and push the base plate from side to side as shown in figure 3.2(b). The three PVC plates have a random stepped roughness profile of average length 4 mm and depth 2 mm. To give structural stability the four corners of the glass panes were screwed to steel spacer tubes to maintain the transverse separation width $W = 7$ cm of the shear cell. The volume between the three PVC plates is filled to a height $h = 12$ cm with a mixture of large and small borosilicate glass beads of diameter d_l and d_s , respectively. The whole cell is then submerged in a refractive index matched fluid to make the semi-opaque intruder easy to identify and track. All the materials used to make the box were selected to be compliant with the refractive index matching technique.

3.3. Refractive index matched shear box experiments

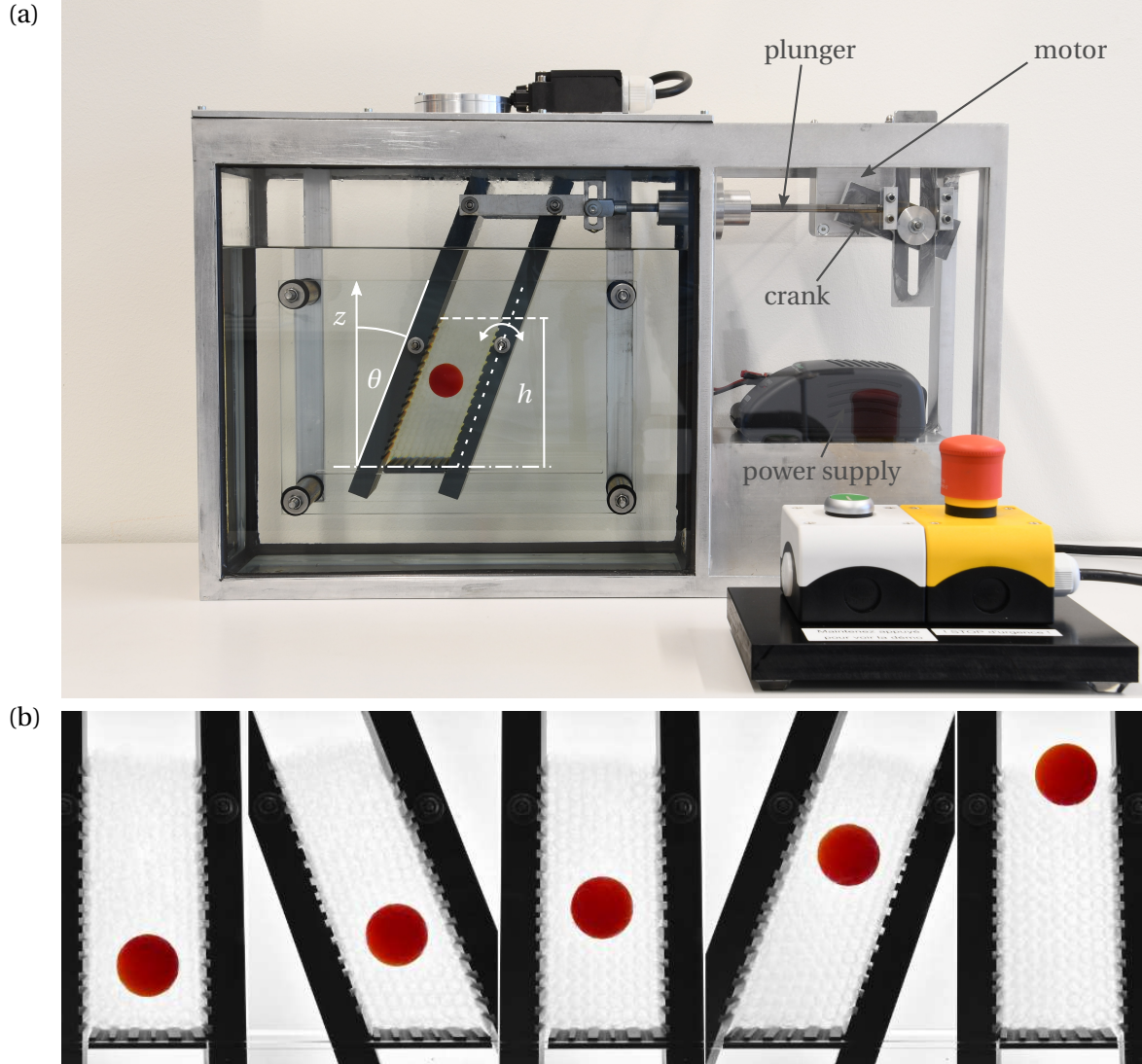


Figure 3.2 – (a) A photograph of the experimental apparatus showing the power supply, motor, crank and plunger that drive the upper end of the pivoted parallel PVC plates from side to side. The two pivot points are located in the middle of the sidewalls and one of them is indicated on the photo. The base plate sits in a notched groove and is able to move freely from side to side in response to the driving motion. The volume between the pivoted PVC plates is filled with a granular material of thickness h that is composed of large and small borosilicate glass beads with diameters d_l and d_s , respectively. The whole system is submersed in a refractive index matched fluid of benzyl alcohol and ethanol that makes the majority of particles transparent, allowing the position of the semi-opaque red intruder to be easily identified. (b) An image sequence showing the rise of a large red intruder of diameter $d_l = 25$ mm through a background medium of small particles of diameter $d_s = 6$ mm over a number of oscillatory cycles. The small grains are just visible so it is possible to see the free-surface.

Figure 3.2(b) shows that over a series of cycles the large red intruder is progressively squeezed upwards until it reaches the top of the cell. To analyze this motion it is useful to define a coordinate system $Oxyz$ with the horizontal x -axis orientated in the direction of shear, the horizontal y axis across the cell and the z axis pointing vertically upwards. Assuming that the PVC plates are pivoted at a height $z = z_{\text{pivot}}$ their imposed horizontal displacement field is

$$x = (z - z_{\text{pivot}}) \sin(\omega t) \tan(\theta_{\text{max}}), \quad (3.10)$$

where ω is the frequency and θ_{max} is the maximum angle of displacement of the sidewalls measured from the vertical axis. Typically θ_{max} ranges between 22.5° and 25° in the experiments presented here. Assuming that the resulting velocity \mathbf{u} within the granular material is spatially uniform in each (x, y) -plane, the resulting velocity components are

$$u = (z - z_{\text{pivot}}) \omega \cos(\omega t) \tan(\theta_{\text{max}}), \quad v = 0, \quad w = 0, \quad (3.11)$$

respectively. The shear-rate $\dot{\gamma} = 2\|\mathbf{D}\|$ where $\|\mathbf{D}\| = \sqrt{\frac{1}{2}\text{tr}(\mathbf{D}^2)}$ is the second invariant of the strain-rate tensor $\mathbf{D} = (\nabla \mathbf{u} + (\nabla \mathbf{u})^T)/2$. For the imposed bulk velocity field (3.11) it follows that the shear rate

$$\dot{\gamma} = \left| \frac{du}{dz} \right| = \omega |\cos(\omega t)| \tan(\theta_{\text{max}}). \quad (3.12)$$

This varies in time, but is spatially uniform throughout the shear cell. The average shear-rate over one complete cycle is

$$\dot{\gamma}_m = \frac{\omega}{2\pi} \int_0^{2\pi} \dot{\gamma} dt = \frac{2\omega}{\pi} \tan(\theta_{\text{max}}). \quad (3.13)$$

The motor which drives the oscillatory shear cell has a variable voltage input, so the applied shear rate depends directly on the voltage and the amplitude of the crank connected to the plunger.

3.3.2 Refractive index matching, image acquisition and particle tracking

Material	n_r	ρ (g cm $^{-3}$)	η (cP)	Supplier
Borosilicate glass	1.4726	2.2	NA	Schäffer Glas
Benzyl alcohol	1.5396	1.044	5.474	Acros Organics
Ethanol	1.3656	0.789	1.2	Fisher Scientific

Table 3.1 – Refractive indexes n_r , densities ρ , viscosities η and suppliers for the materials used in the refractive index matched experiments.

The experiments rely on the refractive index matching (RIM) technique to make the intruder visible. This is achieved by using transparent borosilicate glass beads for the background media and submerging them in a mixture of benzyl alcohol and ethanol. A summary of the material properties is given in table 3.1. A calibration procedure was required to get the right

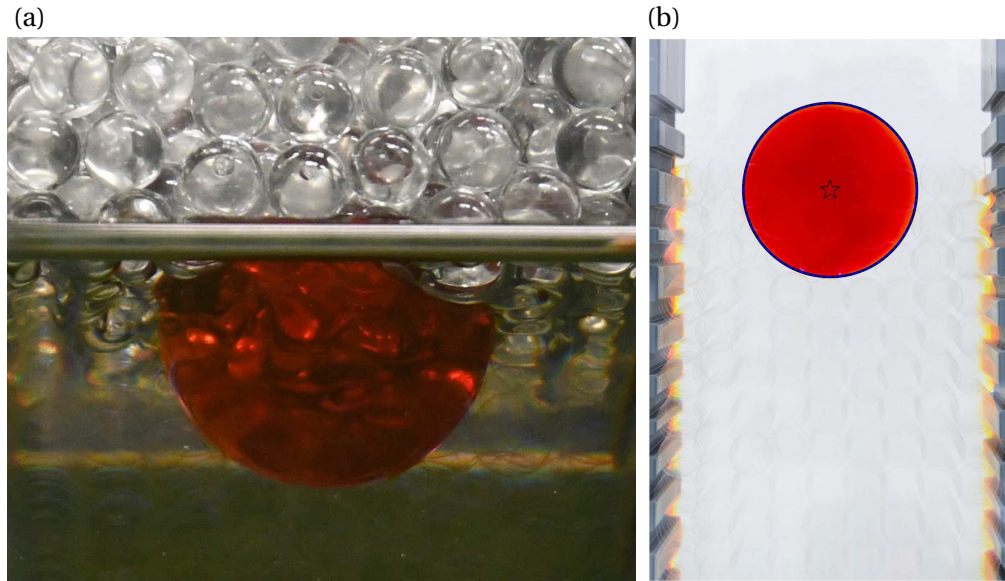


Figure 3.3 – (a) Image showing the contrast between dry and wet conditions using the RIM technique with transparent borosilicate glass beads and a mixture of benzyl alcohol and ethanol. (b) Semi-opaque red intruder identified with the image analysis code.

index match. An Atago RX 5000 α refractometer was therefore used to measure samples of the interstitial fluid. The initial mixture was based on the measurement tables of Chen et al. (2012). Further adjustments to obtain the desired value of $n_r = 1.4726$ were done by adding small quantities of either ethanol or benzyl alcohol. A value of n_r in between 1.471 and 1.472 were acceptable to clearly observe the intruder, a condition that improved for a period of time due to the faster evaporation of ethanol. For the same reason, values over 1.473 were undesirable despite an initially good match. The effect of the refractive index matching is shown in figure 3.3(a) where a large red intruder can clearly be seen in the submersed lower two-thirds of the image, but is completely obscured by the small particles in the dry upper third of the image.

The RIM technique allows the intruder to be clearly seen throughout the experiment (figure 3.2b). Image acquisition was performed with a Basler acA2000-165uc camera positioned in front of the shear box. Different frame rates were used for each experiment, but for most experiments recording was done at 10 frames per second (fps). Particle identification was done using the *imfindcircles* routine implemented in *Matlab*. The single-intruder tracking was performed using the code of Crocker and Grier (1996). As well as tracking the opaque intruder this code also helped to identify, and exclude, false intruders, which could occur when the intruder size was close to that of the background medium. Figure 3.4 shows two space time plots constructed by taking the vertical line of pixels through the centre of the intruder at each frame and plotting them adjacent to one another. It is striking that for comparable size ratios and shear rates the large intruder takes much longer to be squeezed up to the free-surface

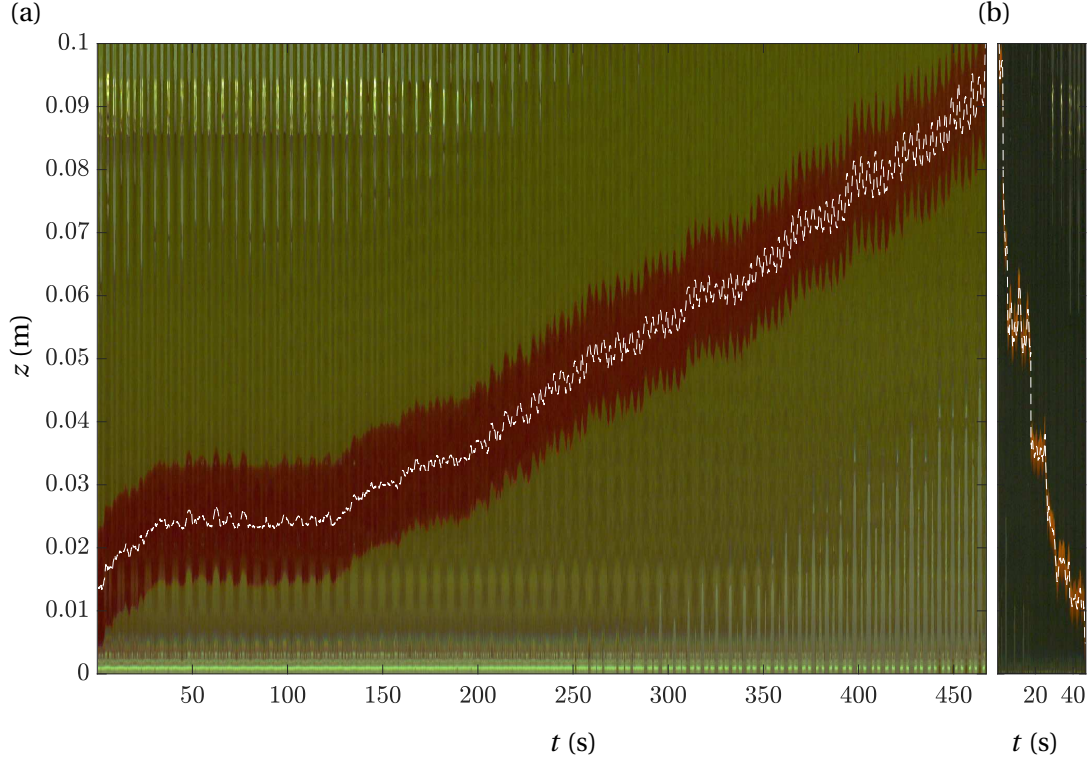


Figure 3.4 – (a) Space-time plot of a large intruder of diameter $d_l = 19$ mm segregating upwards in a medium of small particles of diameter $d_s = 6$ mm subject to an average shear-rate $\dot{\gamma}_m = 0.26 \text{ s}^{-1}$ (taken from set 2 in table 3.2). The space time plot is made by plotting the vertical line of pixels that passes through the centre of the large particle at each time. The intruder therefore appears as a band of red, while the index matched interstitial fluid and the background medium of small particles appear green. The trajectory of the centre of the large intruder as a function of time is shown with the white dashed line. (b) Space time plot of small intruder particle of diameter $d_s = 6$ mm percolating down through a matrix of large particles of diameter $d_l = 14$ mm at a shear rate $\dot{\gamma}_m = 0.34 \text{ s}^{-1}$ (taken from set 4 in table 3.2). In this experiment the background medium appears black while the intruder is orange. The intruder centre as a function of time is shown with a white dashed line.

than the small intruder takes to percolate down to the base. It is also very significant that the trajectories of the intruder centres are both curved.

3.3.3 Experimental data sets

A series of five sets of experiments were performed in order to understand the functional dependence of the segregation velocity magnitude f_{sl} . Sets 1 and 2 correspond to experiments with a single large intruder rising through a medium of small particles. In set 1 the diameter of the large and small particles are held constant and the shear-rate is varied, while in set 2 the

3.4. Preliminary interpretation of the data

diameter of the small particles and the shear-rate are held constant and the diameter of the large intruder is changed. These sets represent experimental conditions where $\phi = 1^-$. Sets 3, 4 and 5 all relate to a small intruder segregating through a matrix of large grains, when $\phi = 0^+$. In sets 3 and 4 the shear-rate is varied for two different small intruder diameters, while in set 5 the shear-rate is held constant and the small intruder diameter is changed. The experimental conditions of all the sets are summarized in table 3.2.

Set	Intruder	d_l (mm)	d_s (mm)	$R = d_l/d_s$	$\dot{\gamma}_m$ (s ⁻¹)
1	Large	19	6	3.17	0.26
		19	6	3.17	0.42
		19	6	3.17	0.59
		19	6	3.17	0.77
2	Large	10	6	1.67	0.26
		12	6	2	0.26
		19	6	3.17	0.26
		25	6	4.17	0.26
3	Small	14	8	1.75	0.34
		14	8	1.75	1.10
		14	8	1.75	2.30
4	Small	14	6	2.33	0.34
		14	6	2.33	0.63
		14	6	2.33	0.87
5	Small	14	12	1.17	0.34
		14	10	1.4	0.34
		14	8	1.75	0.34
		14	6	2.33	0.34
		14	4	3.5	0.34

Table 3.2 – Diameters of the large particles d_l , small particles d_s , the size-ratio $R = d_l/d_s$ and average shear rates $\dot{\gamma}_m$ for each experimental set 1–5. Sets 1-2 correspond to a single large intruder rising through a matrix of small particles, whereas sets 3-5 correspond to a single small particle percolating down through a matrix of large grains.

3.4 Preliminary interpretation of the data

3.4.1 Dimensional analysis

The experimental data is complex and contains a number of functional dependencies that are hard to interpret without a clear initial hypothesis. It is therefore useful to consider what dimensional analysis can say about the functional behaviour of the segregation velocity magnitude f_{sl} before presenting the results. For a dry bi-disperse mixture of large and small particles, f_{sl} is considered to be an output of the system. The inputs are the particle sizes d_l and d_s , the intrinsic density of the grains ρ_* , the volume fraction of small particles $\phi^s = 1 - \phi^l$ per unit granular volume, the solids volume fraction Φ , the bulk shear stress τ , the pressure p ,

gravity g and the shear-rate $\dot{\gamma}$. This is a total of nine variables with three primary dimensions (mass, length and time), so dimensional analysis implies that there are six independent non-dimensional quantities

$$\mu = \frac{\tau}{p}, \quad I = \frac{\dot{\gamma} \bar{d}}{\sqrt{p/\rho_*}}, \quad \Phi, \quad P = \frac{p}{\rho_* g \bar{d}}, \quad R = \frac{d_l}{d_s}, \quad \phi^s, \quad (3.14)$$

where μ is the friction, I is the generalized inertial number in which \bar{d} is the volume fraction weighted average particle diameter

$$\bar{d} = \phi^l d_l + \phi^s d_s, \quad (3.15)$$

P is the non-dimensional pressure and $R = d_l/d_s$ is the grain-size ratio. For a mono-disperse system in the absence of gravity, only the first three non-dimensional variables in (3.14) are relevant, and (3.15) reduces to the monodisperse particle diameter. It was this type of dimensional analysis combined with observations from Discrete Particle Method (DPM) simulations and experiments that led to the development of the incompressible $\mu(I)$ -rheology (MiDi, 2004; Jop et al., 2006), which has advanced our understanding of the rheology of monodisperse granular flows.

Dimensional analysis also provides a powerful way of interpreting the segregation experiments in this paper. It is assumed that it is the combination of shear induced gravity driven percolation (kinetic sieving) and squeeze expulsion (Middleton, 1970; Bridgwater et al., 1985; Savage and Lun, 1988; Gray and Thornton, 2005; Gray, 2018) that generate the dominant mechanism for segregation in dense granular flows. In particular, dimensional analysis implies that the segregation velocity magnitude should scale as

$$f_{sl} \sim \dot{\gamma} \bar{d} \mathcal{G}(\mu, I, \Phi, P, R, \phi^s), \quad (3.16)$$

where $\dot{\gamma} \bar{d}$ is chosen as a reference scale and \mathcal{G} is an arbitrary function of the six non-dimensional variables defined in (3.14). The five sets of experiments detailed in table 3.2 provide key observations that help to constrain the functional form of \mathcal{G} .

3.4.2 Fundamental observations and resulting hypothesis

This paper makes four key assumptions based on the observations (a)-(d) below:- (a) Experimental data sets 1, 3 and 4 imply that the segregation velocity magnitude f_{sl} scales linearly with the shear rate $\dot{\gamma}$ for both large and small intruders. (b) Experimental set 2 implies that the rise velocity of large intruders scales linearly with the particle size-ratio R , and since it necessarily shuts off when $R = 1$ this implies that f_{sl} scales linearly in $(R - 1)$ in the limit $\phi^s = 1^-$. (c) Set 5 shows that in the limit $\phi^s = 0^+$ small intruders exhibit an approximately quadratic dependence on $(R - 1)$ for large size ratios, but have the same linear dependence on $(R - 1)$, as the large intruders, for small size ratios in the range $[1, 1.5]$. (d) All of the data-sets in 1-5 show

that the large and small intruders move along curved trajectories (see e.g. figure 3.4), with slower percolation and rise rates deeper in the flow, where the lithostatic pressure is higher. These trajectories are well approximated by quadratic curves. Since the pressure is lithostatic in the shear cell, this suggests that f_{sl} is proportional to $1/(\mathcal{C} + P)$, where the non-dimensional constant \mathcal{C} has been introduced to prevent a singularity when $P = 0$ at the free-surface.

The four key experimental observations (a-d) above suggest that the segregation velocity magnitude can be written as

$$f_{sl} = \mathcal{B} \dot{\gamma} \bar{d} \frac{\mathcal{F}(R, \phi^s)}{\mathcal{C} + P}, \quad (3.17)$$

where \mathcal{B} and \mathcal{C} are non-dimensional constants and \mathcal{F} is a function of R and ϕ^s . The particle size-ratio dependence is encapsulated in \mathcal{F} , which satisfies the limits

$$\mathcal{F}(R, 1^-) = R - 1, \quad (3.18)$$

$$\mathcal{F}(R, 0^+) = R - 1 + \mathcal{E}(R - 1)^2, \quad (3.19)$$

where \mathcal{E} is another non-dimensional constant. A simple functional form that captures the single large and small intruder cases (3.18) and (3.19) is

$$\mathcal{F} = (R - 1) + \mathcal{E} \Lambda(\phi^s) (R - 1)^2, \quad (3.20)$$

where the function Λ satisfies the constraints

$$\Lambda(0) = 1, \quad \text{and} \quad \Lambda(1) = 0. \quad (3.21)$$

A very simple linear function for Λ will be investigated further in §3.7.

Substituting for the non-dimensional pressure P from the scaling (3.14) the segregation velocity magnitude can be written as

$$f_{sl} = \mathcal{B} \frac{\rho_* g \dot{\gamma} \bar{d}^2}{\mathcal{C} \rho_* g \bar{d} + p} \mathcal{F}(R, \phi^s). \quad (3.22)$$

This formula captures the key processes of gravity, shear and pressure that drive kinetic sieving and squeeze expulsion during the segregation of particles of different sizes and size ratios. The local small particle concentration $\phi^s = 1 - \phi^l$ enters through the average grain-size (3.15) and the nonlinear size ratio dependence (3.20), and automatically generates asymmetry in the segregation flux functions. Equation (3.22) neglects any dependence on the friction of the particles μ and the solids volume fraction Φ . Such dependencies may exist (see Jing et al., 2017; Golick and Daniels, 2009), but they add an extra level of complexity that goes beyond the scope of this paper. Since $I = \dot{\gamma} \bar{d} / \sqrt{p / \rho_*}$ is linear in the shear-rate $\dot{\gamma}$, equation (3.22) can be reformulated to have a linear inertial number dependence instead of a linear shear-rate dependence. Importantly the experimental observation (a), above, implies that there is either a linear shear-rate dependence or a linear inertial number dependence, but to leading order, at least, other shear-rate or inertial number dependencies are not permitted.

3.4.3 Effect of the interstitial fluid

Equations (3.17) and (3.22) take no account of the interstitial fluid that is present in the experiments described in §3.3. Thornton et al. (2006) argued that for slow flows the dominant effect of the fluid was to introduce a factor $\hat{\rho} = (\rho_* - \rho_*^f)/\rho_*$ in the segregation velocity, where ρ_*^f is the intrinsic density of the fluid. This factor represents the relative density difference between the grains and the fluid and slows the segregation-rate down as the density of the fluid approaches that of the grains. In particular, it is able to explain the lack of particle size segregation in density matched experiments with mixtures of particles and fluids (Vallance and Savage, 2000). This factor will not explicitly be considered in this paper, since it is the same in all experiments, but it may affect the assumed value of the non-dimensional constant \mathcal{B} .

3.4.4 Intruder trajectories

In the shear box the gravitational acceleration vector \mathbf{g} points downwards parallel to the z axis, i.e. $\mathbf{g} = -g\mathbf{k}$, where \mathbf{k} is the unit vector in the z -direction. For the bulk velocity field defined in (3.11) it follows from (3.8) that, in the absence of diffusion, the vertical velocity of the large particles satisfies

$$w^l = \frac{dz^l}{dt} = f_{sl}\phi^s, \quad (3.23)$$

where f_{sl} is given by (3.22). For the case of a single large intruder, $\phi^s = 1^-$, and hence the average particle size $\bar{d} = d_s$. The large particle trajectory therefore satisfies the ordinary differential equation (ODE)

$$\frac{dz^l}{dt} = \mathcal{B} \frac{\rho_* g \dot{\gamma} d_s^2}{\mathcal{C} \rho_* g d_s + p} \mathcal{F}(R, 1^-). \quad (3.24)$$

Substituting for $\mathcal{F}(R, 1^-)$ from (3.18) and assuming that the pressure in the grains is lithostatic

$$p = \rho_* g \Phi(h - z), \quad (3.25)$$

the ODE (3.24) reduces to

$$\frac{dz^l}{dt} = \mathcal{B} \frac{\dot{\gamma} d_s^2 (R - 1)}{\mathcal{C} d_s + \Phi(h - z^l)}. \quad (3.26)$$

This is separable and can be integrated, subject to the initial condition that $z^l = z_0^l$ at $t = 0$, to show that time is a quadratic function \mathcal{Z}^l of the vertical coordinate z^l , i.e.

$$\mathcal{K}^l t = \mathcal{C} d_s (z^l - z_0^l) + \frac{\Phi}{2} \left[(h - z_0^l)^2 - (h - z^l)^2 \right] = \mathcal{Z}^l(z^l), \quad (3.27)$$

where the constant

$$\mathcal{K}^l = \mathcal{B} \dot{\gamma} d_s^2 (R - 1), \quad (3.28)$$

is different for each individual experiment. Note that d_s and Φ , which arise in the definition of \mathcal{Z}^l in (3.27), are the same for all the experiments in sets 1 and 2. The quadratic equation (3.27) can be solved to give an explicit formula for the trajectory of the large intruder

$$z^l = \frac{1}{\Phi} \left[\mathcal{C} d_s + \Phi h - \sqrt{\mathcal{C}^2 d_s^2 + 2\mathcal{C} d_s \Phi (h - z_0^l) + \Phi^2 (h - z_0^l)^2 - 2\Phi \mathcal{K}^l t} \right]. \quad (3.29)$$

An exactly analogous argument implies that at $\phi^s = 0^+$ the trajectory of a small intruder satisfies the ODE

$$\frac{dz^s}{dt} = -\mathcal{B} \frac{\dot{\gamma} d_l^2 [(R-1) + \mathcal{E}(R-1)^2]}{\mathcal{C} d_l + \Phi(h - z^s)}. \quad (3.30)$$

This is also separable and can be integrated, subject to the initial condition that $z^s = z_0^s$ at $t = 0$, to show that time is a quadratic function \mathcal{Z}^s of the vertical coordinate z^s ,

$$\mathcal{K}^s t = -\mathcal{C} d_l (z^s - z_0^s) - \frac{\Phi}{2} [(h - z_0^s)^2 - (h - z^s)^2] = \mathcal{Z}^s(z^s) \quad (3.31)$$

where the constant

$$\mathcal{K}^s = \mathcal{B} \dot{\gamma} d_l^2 [(R-1) + \mathcal{E}(R-1)^2], \quad (3.32)$$

changes between experiments. In all the experiments in sets 3-5 the values of d_l and Φ in the definition of \mathcal{Z}^s are the same. The quadratic equation (3.31) can be solved to give an explicit formula for the small intruder trajectory

$$z^s = \frac{1}{\Phi} \left[\mathcal{C} d_l + \Phi h - \sqrt{\mathcal{C}^2 d_l^2 + 2\mathcal{C} d_l \Phi (h - z_0^s) + \Phi^2 (h - z_0^s)^2 + 2\Phi \mathcal{K}^s t} \right]. \quad (3.33)$$

A key test of this scaling argument and the fundamental assumptions (a)-(d) in §3.4.2 is whether the intruder trajectories (3.29) and (3.33) are able to collapse all of the data with the same choices of the non-dimensional constants \mathcal{B} , \mathcal{C} and \mathcal{E} .

3.4.5 The role of particle diffusion

It is important to note that the intruder trajectories calculated in §3.4.4 implicitly assume that there is no diffusion. In fact, experimental observations suggest that there is a significant amount of self diffusion that leads to the intruders performing random walks around the mean path. Utter and Behringer (2004) used a two-dimensional Couette cell to make detailed experimental measurements of the self-diffusion in a monodisperse system of disks. They concluded that the diffusion was anisotropic, but that to leading order the diffusivity was proportional to $\dot{\gamma} d^2$, where d was the particle diameter. The natural generalization of this result to polydisperse systems is to replace the particle diameter with the mean particle diameter (3.15) to give

$$\mathcal{D}_{sl} = \mathcal{A} \dot{\gamma} \bar{d}^2, \quad (3.34)$$

where \mathcal{A} is a non-dimensional constant. Figure 9b in Utter and Behringer's (2004) paper shows that the tangential diffusivity implies $\mathcal{A} = 0.223$, whereas the radial diffusivity implies $\mathcal{A} =$

0.108. The simulations in §3.7 adopt the lower value of \mathcal{A} , because it is based on measurements of the diffusivity made normal to the direction of shear, which is also the predominant direction for diffusion and segregation in the shear box experiments. Note, that since $\bar{d} = d_s$ for a large intruder and $\bar{d} = d_l$ for a small intruder equation (3.34) implies that there will be much more diffusion, and hence variability, for the small intruder paths than for the large intruders.

3.5 Large intruder experiments

The segregation of a single large intruder is stable and robust, especially when the size ratio is large. This is a reflection of the fact that, according to the diffusion scaling (3.34), the underlying self diffusion within the small particle matrix is lower than for a large particle matrix. Larger size ratio intruders also have a lot of contacts with the surrounding small grains, which provides another mechanism for averaging the natural fluctuations. As a result the large intruders only occasionally migrate to the PVC side plates, where they can become stuck when the particle size ratio R is close to unity. To determine the values of \mathcal{B} and \mathcal{C} a global least squares fit is made to all the large intruder trajectories in experimental sets 1 and 2. This suggests that

$$\mathcal{B} = 0.3744, \quad \text{and} \quad \mathcal{C} = 0.2712. \quad (3.35)$$

In practice, the constant \mathcal{C} only changes the gradient of the trajectory close to the free-surface, and this is least well constrained because the experimental free-surface is not clearly defined at the particle scale. Good fits to the data can also be obtained by assuming $\mathcal{C} = 0$, in which case $\mathcal{B} = 0.3615$. This is only a 3.45% difference. Setting $\mathcal{C} = 0$ does, however, introduce a pressure singularity at $p = 0$, which implies that the segregation velocity becomes infinite at the free-surface. This singularity is not only unphysical, but causes difficulties in numerical methods, so in the sections that follow \mathcal{C} is assumed to take its global value defined in (3.35).

3.5.1 Variable shear rate for the large intruders

The experimentally measured position of a large 19 mm intruder in a matrix of small 6 mm particles as a function of time is shown in figure 3.5, for four different shear-rates. These experiments correspond to set 1 in table 3.2. The intruder struggles to segregate upwards when it is close to the bottom of the cell, but once it moves past a few layers it segregates faster and faster towards the surface. As a result the intruder trajectories all show a pronounced curvature in time that are well-fitted by the quadratic curves derived in §3.4.4 using the global value of \mathcal{C} defined in (3.35). For each individual trajectory, equation (3.27) is fitted to the experimental data by determining the constant \mathcal{K}^l that gives the best approximation. Typically the fits were extremely good, with a coefficient of determination lying in the range 0.96–0.97. As the shear-rate $\dot{\gamma}_m$ is increased the large intruder segregates to the surface faster and therefore the time to reach the surface decreases, while the fitting constant increases. The four values of \mathcal{K}^l are plotted as a function of $\dot{\gamma}_m$ in the inset plot in figure 3.5, together with

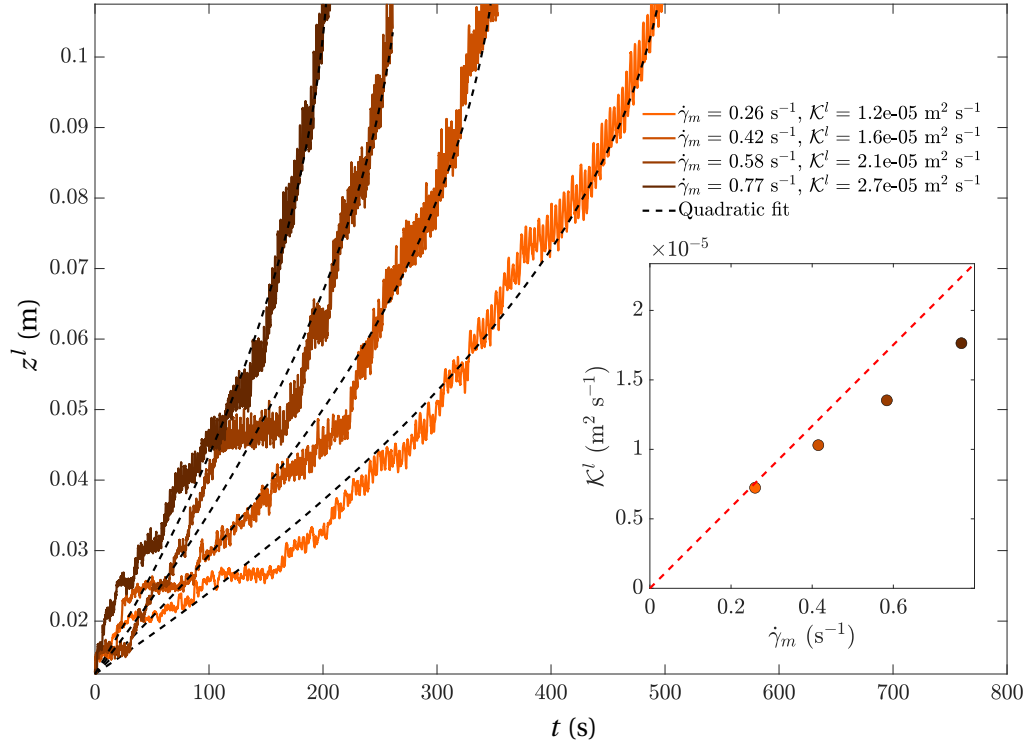


Figure 3.5 – Experimentally measured position of a 19 mm large intruder segregating through a 6 mm matrix of small particles as a function of time, for four different imposed shear rates $\dot{\gamma}_m = 0.26, 0.42, 0.59$ and 0.77 s^{-1} . Darker red lines correspond to higher shear-rates. This data corresponds to set 1 in table 3.2. For each case, equation (3.27) is fitted to the experimental data to determine the constant \mathcal{K}^l assuming that the depth $h = 12 \text{ cm}$ and $\mathcal{C} = 0.2712$ is given by the global best fit to all the large intruder data. The fitted intruder trajectory in time (3.29) is then plotted for each $\dot{\gamma}_m$ with dashed lines for comparison. The coefficient of determination ranges between 0.96 and 0.97 for the proposed fits. The inset shows the fitting constants \mathcal{K}^l as a function of $\dot{\gamma}_m$. These points are closely approximated by the global best fit straight (red dashed) line that passes through the origin (3.36), implying that f_{sl} has a linear shear-rate dependence.

the theoretical straight line passing through the origin defined in (3.28), i.e.

$$\mathcal{K}^l = \mathcal{B} \dot{\gamma}_m d_s^2 (R - 1), \quad (3.36)$$

where it is assumed that $\dot{\gamma} = \dot{\gamma}_m$ and \mathcal{B} is given by the global value in (3.35). The points all lie close to the straight line, although for this subset of data the global fit is not quite the best fit. The data is, however, close to the global fit and is consistent with the fundamental assumption (a) in §3.4.2 that the segregation velocity magnitude is linear in the shear-rate.

3.5.2 Variable size ratio for the large intruders

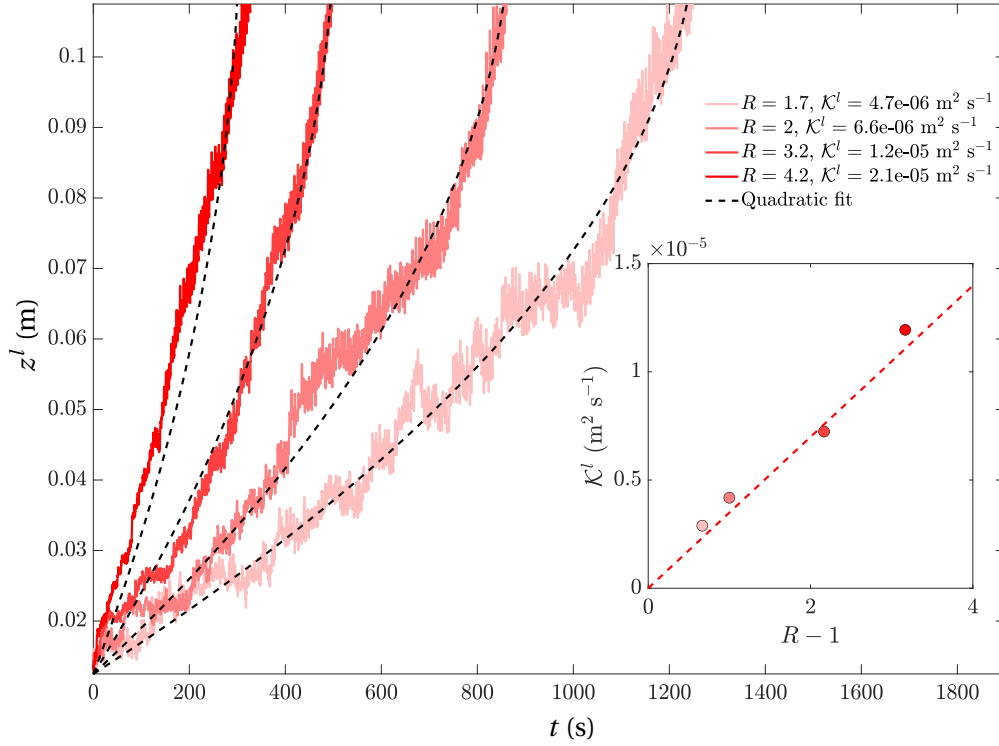


Figure 3.6 – Experimentally measured position of a large intruder of size $d_l = 10, 12, 19$ and 25 mm (darker red lines correspond to larger intruders) in a matrix of 6 mm small particles as a function of time, and at the same imposed shear-rate $\dot{\gamma}_m = 0.26 \text{ s}^{-1}$. This corresponds to set 2 in table 3.2. For each case, equation (3.27) is fitted to the experimental data to determine the constant \mathcal{K}^l assuming that the depth $h = 12$ cm and $\mathcal{C} = 0.2712$ is given by the global best fit to all the large intruder data. The fitted intruder trajectory in time (3.29) is then plotted for each size ratio R with dashed lines for comparison. The coefficient of determination ranges between 0.93 and 0.98. The inset shows the measured constants \mathcal{K}^l as a function of $R - 1$. These points are well approximated by a global best fit straight (red dashed) line that passes through the origin (3.36), implying that f_{sl} has a linear dependence on $R - 1$.

Figure 3.6 shows experimental set 2 (from table 3.2) in which both the shear-rate $\dot{\gamma}_m = 0.26 \text{ s}^{-1}$ and the small particle diameter $d_s = 6$ mm are held constant, while the diameter of the large intruder d_l is varied. In this limit the average particle size $\bar{d} = d_s$, but the size ratio R changes between experiments. As the size ratio is increased the particles segregate faster and the time for a particle to rise from the bottom to the top of the cell decreases. In each case the large intruders describe curved trajectories in time as they rise through the cell. This implies that near the bottom of the cell the segregation rate is considerably lower than close to the surface, where the intruder moves notably faster. The intruder trajectories are all well approximated by the quadratic curves derived in §3.4.4, although there is some evidence that the curves

become more linear at high size ratios. The curves are fitted using a similar procedure to §3.5.1, i.e. by determining the best value of the constant \mathcal{K}^l for each experiment using the global value of \mathcal{C} defined in (3.35). The fitted values of \mathcal{K}^l are plotted as a function of the size ratio $R - 1$ in the inset of figure 3.6. The points lie extremely close to the theoretical straight line (3.36) that passes through the origin, indicating that the segregation rate magnitude f_{sl} is linear in $R - 1$ even at high size ratios, as assumed in hypothesis (b) in §3.4.2.

3.5.3 Collapse of all the large intruder experiments

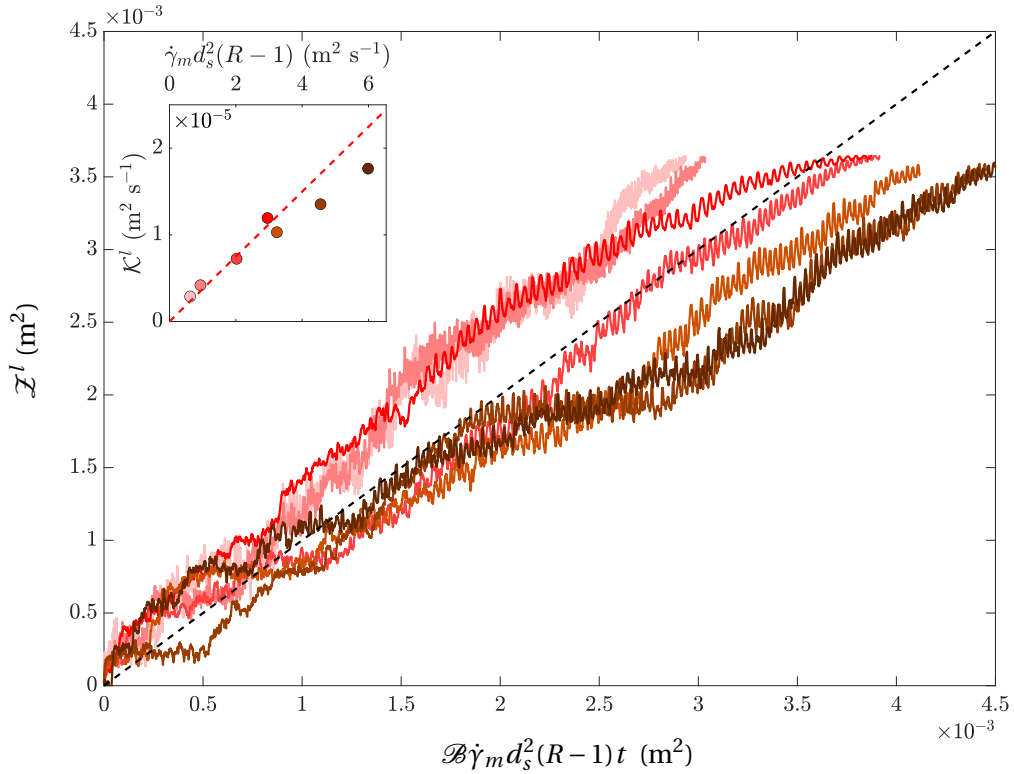


Figure 3.7 – The large intruder trajectories for varying shear rate $\dot{\gamma}_m$ and size ratio R are collapsed onto an approximately straight (dashed) 45 degree line by plotting the transformed height \mathcal{Z}^l , defined in (3.27), against the scaled time $\mathcal{B}\dot{\gamma}_m d_s^2 (R - 1) t$. The data corresponds to all the cases in sets 1 and 2 in table 3.2. The inset plot shows the best fit values of the constants \mathcal{K}^l for each of the experiments as a function of $\dot{\gamma}_m d_s^2 (R - 1)$. The red dashed line in the inset has gradient $\mathcal{B} = 0.3744$, i.e. the global best fit value of \mathcal{B} . The colours of the points and the lines are the same as those used in figures 3.5 and 3.6, where the legends are defined.

All the large intruder trajectory data from sets 1 and 2 can be collapsed by plotting the quadratic function of the height \mathcal{Z}^l , defined in (3.27), as a function of scaled time $\mathcal{B}\dot{\gamma}_m d_s^2 (R - 1) t$ as shown in figure 3.7. This collapse is based on equations (3.27) and (3.36), which imply that

$$\mathcal{Z}^l = \mathcal{B}\dot{\gamma}_m d_s^2 (R - 1) t. \quad (3.37)$$

The mapped trajectories should therefore all lie on the 45 degree line shown in figure 3.7. All the trajectories follow the right trend, but move slightly off the ideal straight line as they rise up through the cell. Some variability is to be expected because the theoretical large intruder trajectory completely ignores the effect of diffusion, which will generate random walks around the average behaviour captured by the theory. Some of the variability is also likely to be an artifact of the oscillatory shear cell, which moves through a maximum angle θ_{\max} before reversing direction, rather than shearing in a consistent direction. This reduces the particle rearrangements, somewhat, and creates brief interludes during which the large intruder oscillates around a given level, before rising upwards again. As can be seen in figure 3.7 these interludes create a horizontal offset in some of the shear-rate data, before the overall rise continues along a line parallel to the 45 degree line. The inset image in figure 3.7 shows the values of \mathcal{K}^l as a function of $\dot{\gamma}_m d_s^2 (R - 1)$. All the experimental points for variable shear-rate and variable size-ratio lie close to the theoretical straight line implied by the global fit with the values of \mathcal{B} and \mathcal{C} from equation (3.35). This confirms that hypotheses (a), (b) and (d), made in §3.4.2, are able to collapse all the large intruder data, with the same constant values of \mathcal{B} and \mathcal{C} .

3.6 Small intruder experiments

The small intruders typically percolate downwards much faster than the large particles segregate upwards (as shown in figure 3.4) and it is anticipated that they will be subject to much more diffusion than the large intruders, because the average grain size $\bar{d} = d_l > d_s$ in the diffusivity (3.34). In general, these combined effects result in the small intruders segregating much more erratically than the large intruders. Several experimental difficulties were observed. The intruder could migrate towards the PVC side plates and become stuck, or get stuck on top of a layer of well-packed large particles. Experimental data where the intruder suddenly dropped down after being stuck for a large number of cycles was not considered to be representative. Once again, such events are probably an artifact of the shear cell, which reverses the direction of shear and has finite dimension. In flows where the shear is in a consistent direction, layers of grains that are higher in the flow move faster than those beneath them and provide a natural mechanism for the small intruders to find new gaps that they can fall into, and hence prevent them from becoming stuck at a given level for a long period of time. To ensure that representative data was collected, each experiment was repeated eight times.

3.6.1 Variable shear rate for the small intruders

Figure 3.8 shows the trajectories of an 8 mm small intruder in a matrix of 14 mm large particles for three different shear rates corresponding to set 3 in table 3.2. Three representative profiles are plotted for each shear rate. The theoretical small particle trajectory is fitted to each curve using the same value of \mathcal{C} as in (3.35), and the average value of \mathcal{K}^s is then used to determine

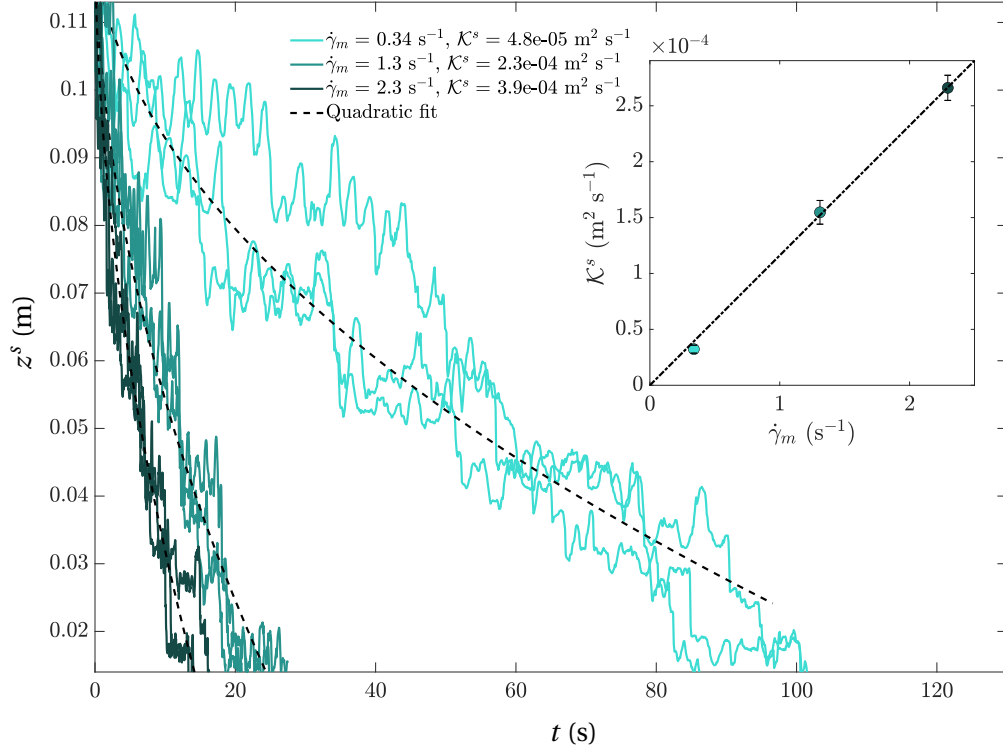


Figure 3.8 – Measured position of a 8 mm small intruder segregating through a 14 mm matrix of large particles as a function of time for three different imposed shear rates $\dot{\gamma}_m$ (darker turquoise lines correspond to higher shear-rates). Three representative experimental profiles are plotted for each experiment. This data corresponds to set 3 in table 3.2. For each case, equation (3.31) is fitted to the data set and the value is then averaged over the three realizations to determine \mathcal{K}^s , assuming the same value of \mathcal{C} as in (3.35). The average fitted intruder trajectory (3.33) is then plotted as a function of time for each $\dot{\gamma}_m$ with dashed lines for comparison. The insets show the fitting constant \mathcal{K}^s as a function of $\dot{\gamma}_m$. All the points are closely approximated by a straight (dot-dashed) line that passes through the origin, implying that f_{sl} has a linear shear-rate dependence at moderate size ratios.

the overall fit. There is quite a lot of variability about the individual fits, as anticipated, but the fitted trajectory captures the overall behaviour of the small intruders as they percolate downwards. As the shear rate is increased the time taken for intruder to reach the bottom of the cell decreases and \mathcal{K}^s increases. The values of \mathcal{K}^s are plotted in the inset graph in figure 3.8 and show a clear linear dependence on the average shear rate $\dot{\gamma}_m$, consistent with the theoretical line

$$\mathcal{K}^s = \mathcal{B} \dot{\gamma}_m d_l^2 [(R-1) + \mathcal{E}(R-1)^2], \quad (3.38)$$

implied by equation (3.32). The quadratic dependence on $(R-1)$ in equation (3.38) suggests that the segregation rate could be much larger for higher size ratios. To test this, and to test that there is still a linear shear rate dependence, figure 3.9 shows how a 6 mm small

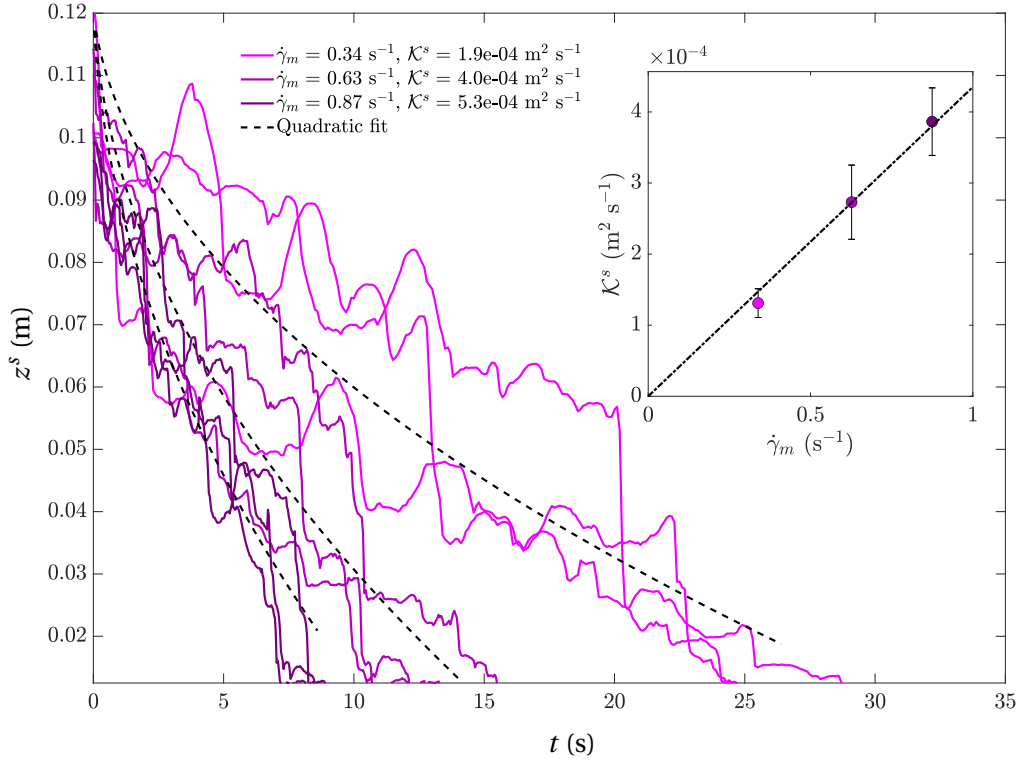


Figure 3.9 – Measured position of a 6 mm small intruder segregating through a 14 mm matrix of large particles as a function of time for three different imposed shear rates $\dot{\gamma}_m$ (darker magenta lines correspond to higher shear-rates). Three representative experimental profiles are plotted for each experiment. This data corresponds to set 4 in table 3.2. For each case, equation (3.31) is fitted to the data set and the value is then averaged over the three realizations to determine \mathcal{K}^s , assuming the same value of \mathcal{C} as in (3.35). The average fitted intruder trajectory (3.33) is then plotted as a function of time for each $\dot{\gamma}_m$ with dashed lines for comparison. The insets show the fitting constant \mathcal{K}^s as a function of $\dot{\gamma}_m$. All the points are closely approximated by a straight (dot-dashed) line that passes through the origin, implying that f_{sl} has a linear shear-rate dependence even at larger size ratios.

intruder percolates down through a matrix of 14 mm large particles at various shear rates. This corresponds to a size ratio $R = 2.333$, which is not that much larger than $R = 1.75$ for the previous experiments in figure 3.8, but the time taken to reach the bottom of the cell for $\dot{\gamma}_m = 0.34 \text{ s}^{-1}$ is approximately a quarter of that when the size ratio was $R = 1.75$. Importantly, however, the fitted values of \mathcal{K}^s still exhibit a linear dependence on $\dot{\gamma}_m$ as shown in the inset of figure 3.9. This observation suggests that the dramatic enhancement in the segregation rate of the small intruders at large size ratios, can be modelled through an additional quadratic size ratio dependence in the function $\mathcal{F} = \mathcal{F}(R, \phi^s)$ defined in (3.20) at low small particle volume fractions.

3.6.2 Variable size ratio for the small intruders

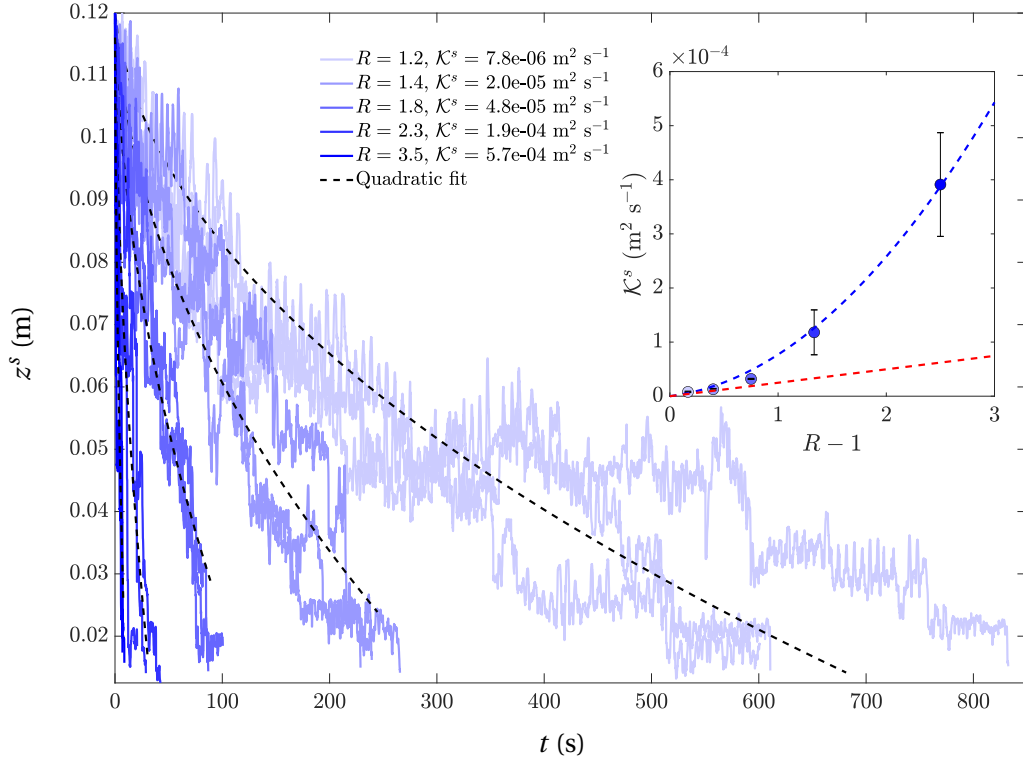


Figure 3.10 – Experimentally measured position of a small intruder of size $d_l = 12, 10, 8, 6$ and 4 mm in a matrix of 14 mm large particles as a function of time, and at the same imposed shear-rate $\dot{\gamma}_m = 0.34 \text{ s}^{-1}$. This corresponds to set 5 in table 3.2. For each case, equation (3.31) is fitted to the data set and the value is then averaged over the three realizations to determine \mathcal{K}^s , assuming the same value of \mathcal{C} as in (3.35). The average fitted intruder trajectory (3.33) is then plotted as a function of time for each size ratio R with dashed lines for comparison. The inset shows the fitting constants \mathcal{K}^s as a function of $(R - 1)$. At size ratios close to unity the constants follow the same linear dependence on $(R - 1)$ as the large grains (red dashed line), but for larger size ratios the constants \mathcal{K}^s become much larger. This is well fitted by the quadratic size ratio dependence in equation (3.38) with $\mathcal{E} = 2.0957$ (dashed blue line).

In order to determine the non-dimensional constant \mathcal{E} in (3.38) a series of experiments were performed at the same shear rate, but with variable size ratio. These correspond to set 5 in table 3.2 and are shown in figure 3.10. Fits to the three sets of data shown for each case were performed in the same way as in §3.5.1 and the values of \mathcal{K}^s are shown in the inset of figure 3.10. For size ratios close to unity the values of \mathcal{K}^s lie very close to the red dashed line, corresponding to equation (3.38) with $\mathcal{E} = 0$, using the same coefficients \mathcal{B} and \mathcal{C} that were determined for the large intruders in (3.35). However, as the size ratio increases above $R = 1.5$ the values of \mathcal{K}^s depart markedly from this line. The additional quadratic dependence on $(R - 1)$ in (3.38) is, however, able to capture the dramatic increase in the segregation velocity at

large size ratios. A least squares fit to the data suggests that

$$\mathcal{E} = 2.0957. \quad (3.39)$$

3.6.3 Collapse of all the small intruder experiments

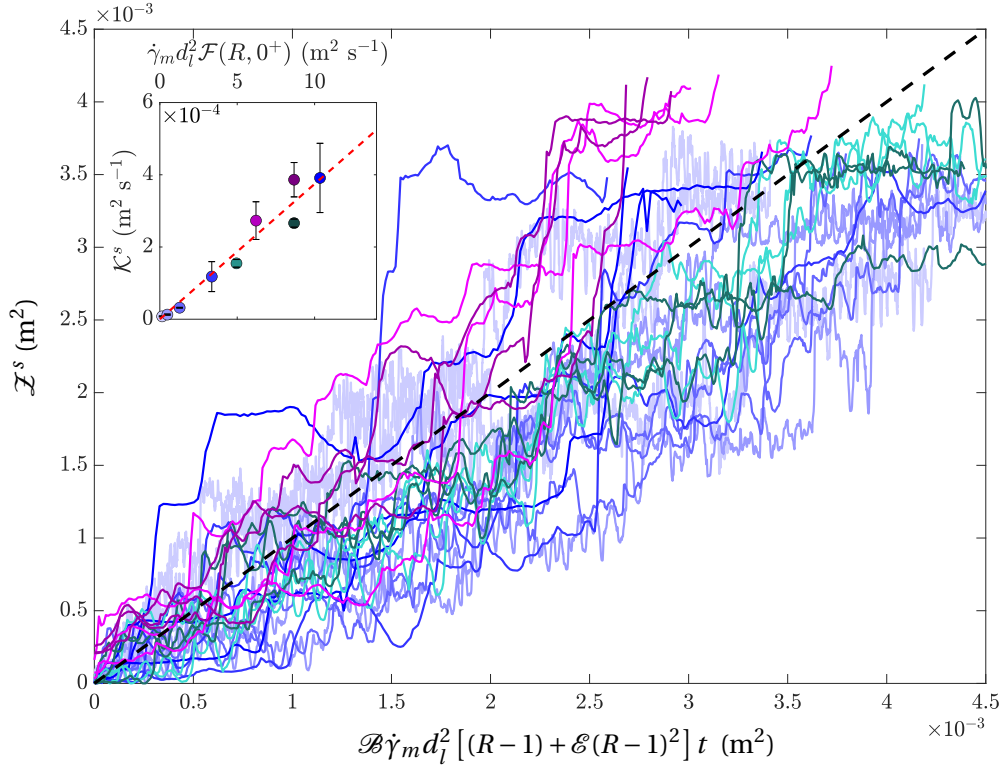


Figure 3.11 – The small intruder trajectories for varying shear rate $\dot{\gamma}_m$ and size ratio R are collapsed onto an approximately straight (dashed) 45 degree line by plotting the transformed height \mathcal{Z}^s , defined in (3.31), against the scaled time $\mathcal{B}\dot{\gamma}_m d_l^2 [(R-1) + \mathcal{E}(R-1)^2] t$. The data corresponds to all the cases in sets 1 and 2 in table 3.2. The inset plot shows the best fit values of the constants \mathcal{K}^s for each of the experiments as a function of $\dot{\gamma}_m d_l^2 \mathcal{F}(R, 0^+)$. The red dashed line in the inset has gradient $\mathcal{B} = 0.3744$, i.e. the global best fit value of \mathcal{B} . The colours of the points and the lines are the same as those used in figures 3.8, 3.9 and 3.10, where the legends are defined.

All the small intruder data from sets 3, 4 and 5 in table 3.2 and shown in figures 3.8–3.10 can now be collapsed onto a single curve using the same coefficients \mathcal{B} , \mathcal{C} and \mathcal{E} . This is achieved by plotting the quadratic function of the height \mathcal{Z}^s defined in (3.31) as a function of the scaled time $\mathcal{B}\dot{\gamma}_m d_l^2 [(R-1) + \mathcal{E}(R-1)^2] t$ as shown in figure 3.11. This collapse is based on equations (3.31) and (3.32), which imply that

$$\mathcal{Z}^s = \mathcal{B}\dot{\gamma}_m d_l^2 [(R-1) + \mathcal{E}(R-1)^2] t. \quad (3.40)$$

The mapped trajectories should therefore lie on the 45 degree line in figure 3.11. The collapse for the individual trajectories is far from perfect for the reasons discussed at the beginning of §3.6, which is to be anticipated, but they do follow the right general trend for a wide range of shear rates and particle size ratios. The collapse is much more convincing when the individual fitted values of \mathcal{K}^s are plotted against the theoretical line implied by equation (3.38), which is shown in the inset of figure 3.11. All the measured points lie very close to the theoretical straight line passing through the origin. This confirms that both the small intruder data (as well as the large intruder data) can be collapsed for the same values of the non-dimensional constants \mathcal{B} , \mathcal{C} and \mathcal{E} and validates the preliminary hypotheses (a)-(d) made in §3.4.2.

3.7 Simulation of van der Vaart *et al.*'s (2015) experiment

The fully index matched experiment of van der Vaart *et al.* (2015), which was performed in a similar shear cell to that in this paper, provides an important final constraint on the functional form of \mathcal{F} , since the particle-size distribution evolves through the complete range of $\phi^s \in [0, 1]$.

3.7.1 Summary of the equations and coefficients

In order to derive the governing equations, the particle-size distribution is assumed to be spatially uniform in the x and y directions. Substituting the gravity vector $\mathbf{g} = -g\mathbf{k}$ and the velocity field (3.11) into (3.3) implies that the small particle segregation equation reduces to

$$\frac{\partial \phi^s}{\partial t} - \frac{\partial}{\partial z} \left(f_{sl} \phi^s \phi^l \right) = \frac{\partial}{\partial z} \left(\mathcal{D}_{sl} \frac{\partial \phi^s}{\partial z} \right), \quad (3.41)$$

where f_{sl} and \mathcal{D}_{sl} are the segregation velocity magnitude and diffusivity, respectively. Substituting the lithostatic pressure (3.25) into (3.22) and cancelling $\rho_* g$, implies that

$$f_{sl} = \frac{\mathcal{B} \dot{\gamma} \bar{d}^2 \mathcal{F}}{\mathcal{C} \bar{d} + \Phi(h - z)}, \quad (3.42)$$

where the size ratio dependence is encapsulated in

$$\mathcal{F} = (R - 1) + \mathcal{E} \Lambda(\phi^s) (R - 1)^2. \quad (3.43)$$

The function $\Lambda = \Lambda(\phi^s)$ satisfies the constraints that $\Lambda(0) = 1$ and $\Lambda(1) = 0$. It describes the effect of the size ratio at intermediate concentrations, and allows \mathcal{F} to smoothly transition from the linear $(R - 1)$ dependence of a single large intruder (3.18) to the quadratic $(R - 1)$ dependence (3.19) for a single small intruder. The simplest possible form for Λ is the linear law

$$\Lambda = \phi^l = 1 - \phi^s, \quad (3.44)$$

which will be investigated here. However, much more complicated functions are possible, so long as they satisfy the constraints (3.21). As discussed in §3.4.5 the diffusivity is assumed to

take the form

$$\mathcal{D}_{sl} = \mathcal{A} \dot{\gamma} \bar{d}^2, \quad (3.45)$$

where the non-dimensional coefficient \mathcal{A} is determined by the experiments of Utter and Behringer (2004). The other non-dimensional coefficients \mathcal{B} , \mathcal{C} and \mathcal{E} have been determined by the shear box experiments in this paper and all of them are summarized in table 3.3.

$$\mathcal{A} = 1.08, \quad \mathcal{B} = 0.3744, \quad \mathcal{C} = 0.2712, \quad \mathcal{E} = 2.0957.$$

Table 3.3 – Non-dimensional coefficients \mathcal{B} , \mathcal{C} , \mathcal{E} determined from the refractive index matched shear cell experiments. Note that it is anticipated that in the absence of an interstitial fluid the segregation rate will be enhanced (see §3.4.3), which increases the assumed value of \mathcal{B} . The non-dimensional coefficient \mathcal{A} is taken from figure 9 of Utter and Behringer (2004).

3.7.2 Non-dimensionalization and numerical method

In order to solve the system of equations (3.41)–(3.45) it is useful to non-dimensionalize the equations using the same scalings as in van der Vaart et al. (2015), i.e.

$$t = T\tilde{t}, \quad z = h\tilde{z} \quad (3.46)$$

where $T = 13$ s is the period of one cycle and $h = 0.087$ m is the depth of the cell. It follows that the segregation equation (3.41) can be written in the non-dimensional form

$$\frac{\partial \phi^s}{\partial \tilde{t}} - \frac{\partial}{\partial \tilde{z}} \left(S_r \phi^s \phi^l \right) = \frac{\partial}{\partial \tilde{z}} \left(D_r \frac{\partial \phi^s}{\partial \tilde{z}} \right), \quad (3.47)$$

where the non-dimensional segregation rate and non-dimensional diffusivity are

$$S_r = \frac{T f_{sl}}{h} = \frac{\mathcal{B} \dot{\gamma} T (\bar{d}/h)^2 \mathcal{F}}{\mathcal{C} (\bar{d}/h) + \Phi(1 - \tilde{z})}, \quad (3.48)$$

$$D_r = \frac{T \mathcal{D}_{sl}}{h^2} = \mathcal{A} \dot{\gamma} T (\bar{d}/h)^2, \quad (3.49)$$

respectively. The period $T = 2\pi/\omega$ by definition. It therefore follows from (3.13) that the average shear rate $\dot{\gamma}_m$ times the period

$$\dot{\gamma}_m T = 4 \tan(\theta_{\max}), \quad (3.50)$$

where $\theta_{\max} = 30^\circ$ in the experiments of van der Vaart et al. (2015). The mean value $\dot{\gamma}_m T$ is used to approximate $\dot{\gamma} T$ in (3.48) and (3.49). The non-dimensional segregation equation (3.47) is solved subject to no flux conditions at the surface and the base of the cell

$$S_r \phi^s \phi^l + D_r \frac{\partial \phi^s}{\partial \tilde{z}} = 0, \quad \text{at} \quad \tilde{z} = 0, 1, \quad (3.51)$$

and the initial condition

$$\phi^s = \begin{cases} 1, & \tilde{z} > 0.5 \\ 0, & \tilde{z} \leq 0.5, \end{cases} \quad (3.52)$$

so that all the small grains are above the large particles at the start of the experiment (van der Vaart *et al.*, 2015). A Galerkin finite element solver (Skeel and Berzins, 1990) is used to generate the results. This method is conveniently coded in the `pdepe` routine in Matlab and has been extensively tested in previous papers (Wiederseiner *et al.*, 2011b; Gray and Ancey, 2011; van der Vaart *et al.*, 2015; Gray and Ancey, 2015). It should be noted, however, that this method fails when $C = 0$, because in this case the segregation rate becomes unbounded at the free surface.

3.7.3 Asymmetric segregation flux functions

It is interesting to see what the consequences the empirically derived scaling law has for the shape of the segregation flux function. The non-dimensional segregation equation (3.47) implies that the non-dimensional segregation flux of large and small particles in the vertical direction are

$$\tilde{F}^l = S_r \phi^s \phi^l, \quad (3.53)$$

$$\tilde{F}^s = -S_r \phi^s \phi^l, \quad (3.54)$$

respectively. Rather than being a non-dimensional constant (as in Gray and Thornton, 2005; Gray and Chugunov, 2006), the non-dimensional segregation rate S_r is a function, whose value varies locally in the flow, and which is given by (3.48).

Figure 3.12(a) shows a series of flux curves for different size ratios R , assuming that $\hat{z} = 1/2$, $d_s = 4$ mm and the non-dimensional coefficients in table 3.3. All the flux curves are asymmetric and have an inflection point that lies to the right of the maximum. Qualitatively they look similar to the cubic flux functions for $\chi > 1/2$ illustrated in figure 3.1. Crucially, however, these curves have been derived to quantitatively match experimental data and contain complex functional dependencies on the shear rate, the local small particle concentration, the average grain size, the grain-size ratio and the local pressure. In particular, as the grain-size ratio is increased the amplitude of the flux function increases and both the local maximum and the inflection point move to the left.

The increasing skewness with grain-size ratio encodes the idea that small intruders find it increasingly easy to percolate downwards as the size ratio increases, whereas the large intruders find it harder to segregate upwards when there are more contacts with neighbouring small particles. The flux curves have this asymmetric behavior even when $\mathcal{C} = 0$ and $\mathcal{E} = 0$, indicating that the scaling of the segregation rate on the mean particle diameter \bar{d} in (3.22) is already sufficient to produce this effect. The flux curves look similar at other heights in the flow and grow in amplitude as one approaches the free surface. When $\mathcal{C} \neq 0$ there is an upper bound for the amplitude at $\hat{z} = 1$, but when $\mathcal{C} = 0$ the segregation flux becomes unbounded at

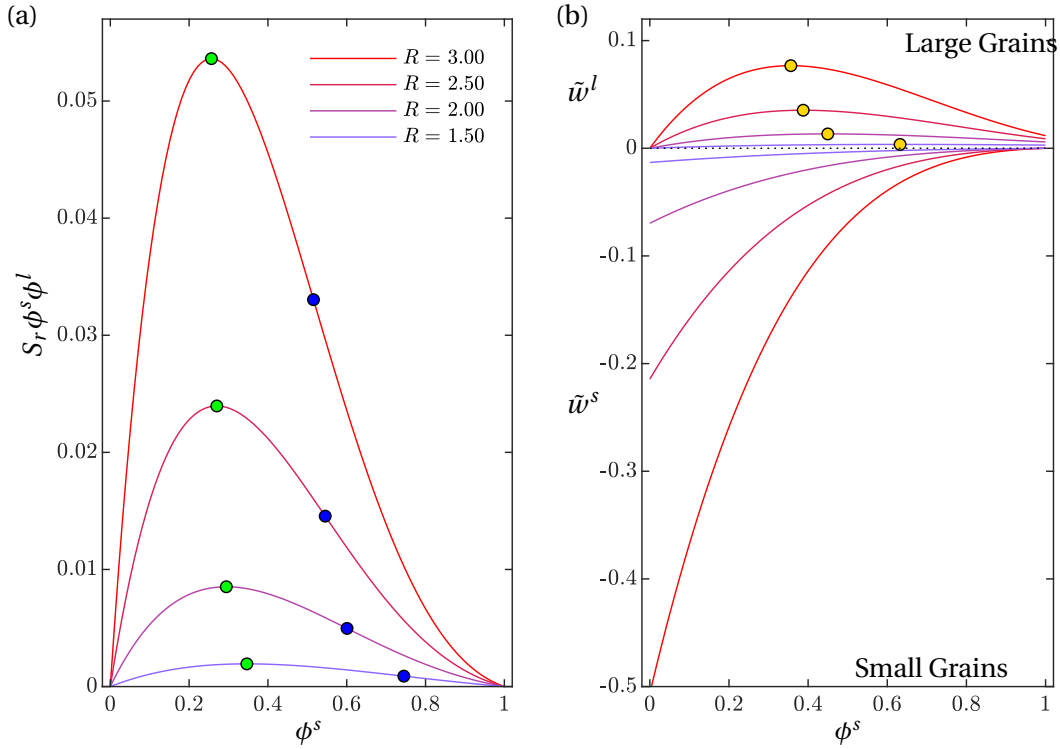


Figure 3.12 – (a) The non-dimensional segregation flux $S_r \phi^s \phi^l$ as a function of the small particle concentration ϕ^s , for a range of grain-size ratios $R = 1.5, 2, 2.5$ and 3 . The flux is evaluated with $h = 87$ mm, $T = 13$ s, $\theta_{\max} = 30^\circ$, $d_s = 4$ mm and $\hat{z} = 1/2$, using the non-dimensional coefficients summarized in table 3.3. The green markers show the position of the maximum and the blue markers show the inflection point. (b) Shows the corresponding non-dimensional large and small particle segregation velocities, \tilde{w}^l and \tilde{w}^s , as a function of ϕ . The yellow markers show the position of the maximum large particle segregation velocity, which occurs at intermediate concentrations.

the free surface, which is not desired.

3.7.4 Large and small particle segregation velocities

In the absence of diffusion the non-dimensional vertical velocity of the large and small particles are given by

$$\tilde{w}^l = S_r \phi^s, \quad (3.55)$$

$$\tilde{w}^s = -S_r \phi^l, \quad (3.56)$$

respectively. These are plotted in figure 3.12(b) for the same size ratios and parameters as the flux functions in figure 3.12(a). For a given size ratio, the downward small particle segregation velocity is an increasing function of the large particle concentration $\phi^l = 1 - \phi^s$,

and therefore the maximum speed is attained at $\phi^s = 0^+$. Conversely, the large particles have a local maximum segregation velocity at an intermediate concentration $\phi^s \in (0, 1)$, with the segregation velocity of a single large intruder at $\phi^s = 1^-$ being at a much reduced rate, compared to either the maximum large particle, or the maximum small particle, segregation speed. Experimental measurements of the single intruder end states have been specifically used in this paper to determine the scaling law for segregation, and hence the segregation rate S_r . The particle velocities in these end states are therefore a close match to the experimental data.

It is interesting to note that when $\mathcal{C} = 0$, the ratio of the maximum percolation velocity of a single small intruder to the rise velocity of a single large intruder at a given height \hat{z}_0 , satisfies the simple relation

$$\frac{|\tilde{w}^s(0^+)|}{|\tilde{w}^l(1^-)|} \bigg|_{\hat{z}=\hat{z}_0} = \frac{S_r(0^+)}{S_r(1^-)} \bigg|_{\hat{z}=\hat{z}_0} = R^2 (1 + \mathcal{E}(R - 1)). \quad (3.57)$$

The remarkable equation relates two seemingly disparate ends of the flux curve with a simple relation that is purely dependent on the particle size ratio R . It holds at all heights \hat{z}_0 in the flow, which implies that the trajectories of the particles are also related. In particular, it follows from equations (3.27) and (3.31) that the ratio of the time t_l for a large intruder to reach the top of the cell, and the time t_s for a small intruder to percolate down to the base, satisfies the same law

$$\frac{t_l}{t_s} = R^2 (1 + \mathcal{E}(R - 1)). \quad (3.58)$$

Even when $\mathcal{C} = 0.2712$, and there is some dependence on the average grain size and the position in the flow, equations (3.57) and (3.58) provide good approximations to the ratio of the single particle intruder speeds and the ratio of intruder times, respectively.

3.7.5 Comparison to van der Vaart's (2015) experimental data

Van der Vaart *et al.* (2015) used an earlier version of shear cell and the refractive index matching technique to measure the evolution of the particle-size distribution in a 50:50 mix of 8 mm and 4 mm particles that was initially in a normally graded configuration. To do this, the shear was stopped after each complete cycle and the cell was scanned with a laser while a series of photographs were taken. From these photos it was possible to determine the three-dimensional particle positions after each cycle and hence to build up a picture of the evolving particle size distribution in time. A space-time plot of the van der Vaart *et al.*'s (2015) small particle concentration data is shown in figure 3.13(a).

Figure 3.13(b) shows a contour plot of the computed small particle concentration as a function of the non-dimensional depth and time, using the experimentally determined non-dimensional coefficients in table 3.3. The simulations are in very good quantitative agreement with the experimental data of van der Vaart *et al.* (2015). In particular, the simulations accurately capture the time at which the first small grains reach the base of the flow, as well as the

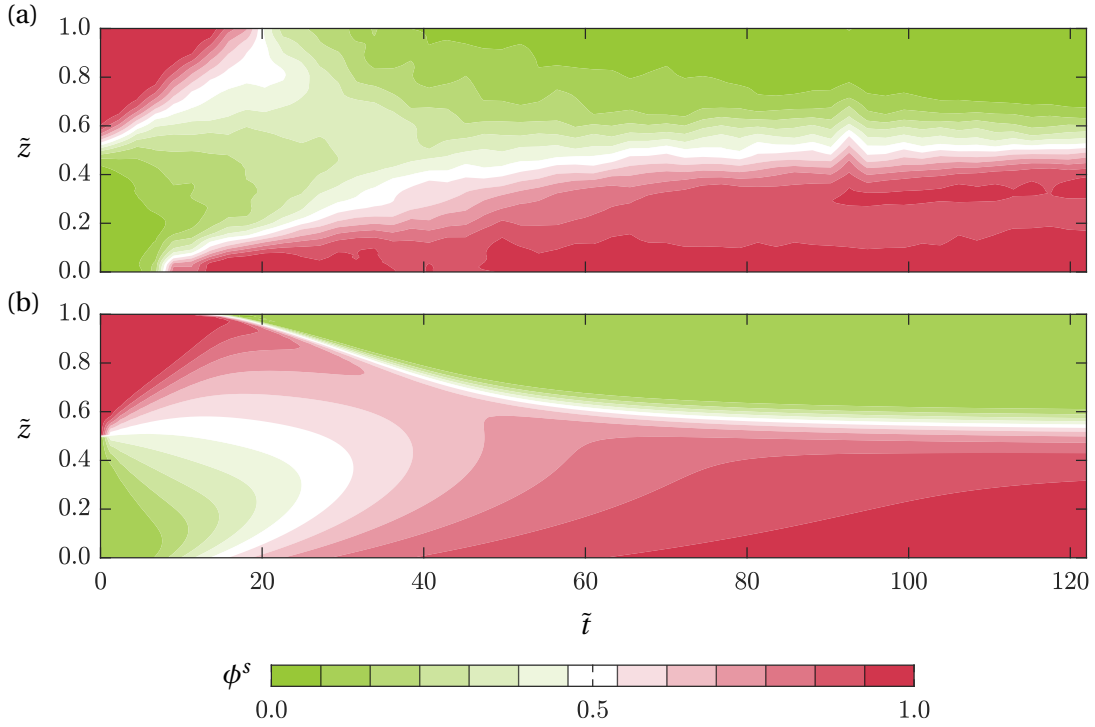


Figure 3.13 – (a) Contour plot of van der Vaart et al.’s (2015) small particle concentration data as a function of the non-dimensional depth $\tilde{z} = z/h$ and non-dimensional time $\tilde{t} = t/T$, for a 50:50 mix of large and small particles with $h = 87$ mm, $T = 13$ s, $\theta_{\max} = 30^\circ$, $d_s = 4$ mm and $d_l = 8$ mm. (b) Contour plot of the corresponding numerical results using the non-dimensional coefficients summarized in table 3.3.

slightly later arrival of the first large grains at the top of the flow. The simulated concentration is not in perfect agreement with experiment between $\hat{t} = 20$ and 60 non-dimensional time units, but the results accurately capture the overall timescale for the large particles to rise to the surface and the small particles to percolate down to the base. In particular, by $\hat{t} = 120$ non-dimensional time units the particle-size distribution is close to steady-state, with the large particles concentrated in the top half of the cell, while the small grains are concentrated in the bottom half. It should be emphasized that this excellent overall agreement is achieved with the value of \mathcal{A} determined from the experiments of Utter and Behringer (2004) and the same non-dimensional coefficients \mathcal{B} , \mathcal{C} or \mathcal{E} measured in this paper, together with the simplest possible functional form for Λ .

3.7.6 Properties of the steady-state solution

A first order ordinary differential equation (ODE) for the steady-state concentration profile can be formulated by assuming that the concentration is independent of time. Integrating the non-dimensional segregation equation (3.47) with respect to \tilde{z} , applying the no flux condition

(3.51) and cancelling the $\dot{\gamma}T(\bar{d}/h)^2$ dependence yields

$$\frac{d\phi^s}{d\tilde{z}} = -\frac{(\mathcal{B}/\mathcal{A})\phi^s\phi^l\mathcal{F}(R,\phi^s)}{\mathcal{C}(\bar{d}/h) + \Phi(1-\tilde{z})}. \quad (3.59)$$

This equation has some interesting properties. In particular, the non-dimensional coefficient \mathcal{C} is included in the theory primarily to remove the singularity in the segregation-rate at the free-surface in the numerical method. When $\mathcal{C} = 0$, equation (3.59) just depends on the particle size ratio R , and is completely independent of \bar{d} and h . The thickness does enter in the non-dimensionalization (3.46), so although the non-dimensional solution will be identical for a fixed size ratio, the physical solution will be stretched vertically proportionately to h . As a result, a flow of double the thickness will have steady-state concentration gradients that are half as strong as another flow with the same size ratio. This is a highly non-intuitive consequence of the combination of the scaling law (3.42) and the diffusivity (3.45), and is a bold prediction of the resulting theory.

3.7.7 Exact steady-state solution for the case $\mathcal{C} = 0$

In the case when $\mathcal{C} = 0$, it is possible to derive an exact steady-state solution to (3.59). Substituting (3.43) and (3.44) into (3.59) and writing it as an ODE for $\hat{z} = \hat{z}(\phi^s)$ implies

$$\frac{-1}{(1-\hat{z})} \frac{d\hat{z}}{d\phi^s} = \frac{\mathcal{A}\Phi}{\mathcal{B}(R-1)\phi^s(1-\phi^s)[1+\mathcal{E}(1-\phi^s)(R-1)]}. \quad (3.60)$$

Using partial fractions the righthand side can be integrated to give the exact solution

$$z = 1 - K(1-\phi^s)^{-\lambda_1}(1+\mathcal{E}(1-\phi^s)(R-1))^{\lambda_2}(\phi^s)^{\lambda_3}, \quad (3.61)$$

where K is a constant of integration and the coefficients λ_1 , λ_2 and λ_3 are

$$\lambda_1 = \frac{\Phi\mathcal{A}}{\mathcal{B}(R-1)}, \quad \lambda_2 = \frac{\Phi\mathcal{A}\mathcal{E}}{\mathcal{B}(1+\mathcal{E}(R-1))}, \quad \lambda_3 = \frac{\Phi\mathcal{A}}{\mathcal{B}(R-1)(1+\mathcal{E}(R-1))}, \quad (3.62)$$

respectively. The average volume fraction of small particles in the cell is obtained by integrating the area under the curve $\phi^s = \phi^s(\hat{z})$ between zero and unity. Since, this area is exactly the same as the area under the curve $\hat{z} = \hat{z}(\phi^s)$ in the range $\phi^s = [0, 1]$, it is easy to find the constant of integration for any given average concentration of small particles in the cell.

3.7.8 Steady-state comparison to van der Vaart's (2015) experiment

Figure 3.14 shows the predicted steady-state exact solution for the experiment of van der Vaart *et al.* (2015), where $K = 0.4041$ for the initial 50:50 mix of particles. At $\hat{t} = 221$ non-dimensional units the exact solution lies very close to the computed concentration profile using the non-zero value of $\mathcal{C} = 0.2712$ determined in this paper. In fact both the curves

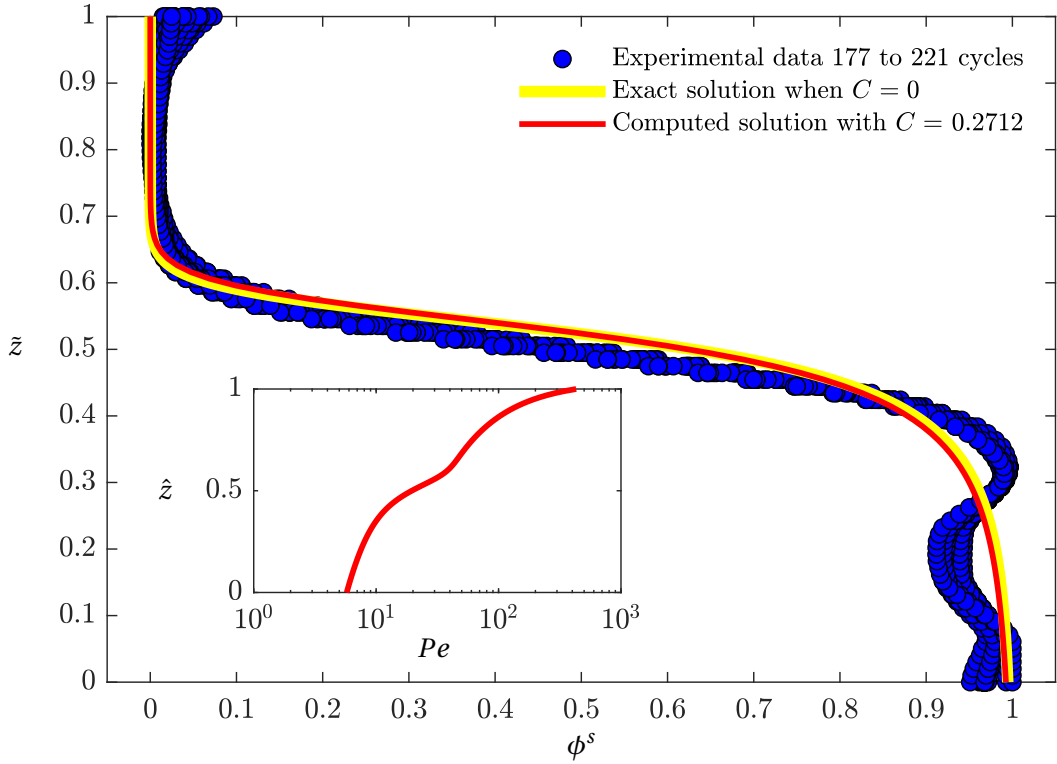


Figure 3.14 – Plot of the computed small concentration ϕ^s at $\bar{t} = 221$ non-dimensional time units (red line) as a function of the non-dimensional depth, for $h = 87$ mm, $T = 13$ s, $\theta_{\max} = 30^\circ$, $d_s = 4$ mm, $d_l = 8$ mm and using the non-dimensional coefficients summarized in table 3.3. The blue circles show the corresponding experimental data of van der Vaart et al. (2015) between $\bar{t} = 177$ and 221 non-dimensional time units (cycles). The yellow curve shows the exact steady-state solution (when $\mathcal{C} = 0$) with a constant of integration $K = 0.4041$ for a 50:50 mix of particles as in van der Vaart et al.’s (2015) experiments. The inset image shows the variation of the Péclet number with depth for the computed solution when $\mathcal{C} \neq 0$.

lie very close to van der Vaart et al.’s (2015) experimental data between 177 and 221 cycles, when the experiment is essentially in steady state (see fig. 3.14). Following Wiederseiner et al. (2011b) and Gray (2018), the Péclet number for segregation is defined as the ratio of the non-dimensional segregation-rate to the rate of non-dimensional diffusion, i.e.

$$Pe = \frac{S_r}{D_r} = \frac{\mathcal{B}(R-1)(1+\mathcal{E}(1-\phi^s)(R-1))}{\mathcal{A}(\mathcal{C}(\bar{d}/h) + \Phi(1-\bar{z}))}. \quad (3.63)$$

It provides a measure of the strength of the segregation relative to the diffusion. As opposed to some earlier theories (see e.g. Gray and Chugunov, 2006; Wiederseiner et al., 2011b), which had a constant Péclet number, the segregation model developed in this paper produces a Péclet number that varies strongly with depth. This is due to the changing local grain-size distribution and the decreasing lithostatic pressure distribution with increasing height. For the computed solution (see inset fig. 3.14) the Péclet number starts at $Pe = 5.74$ at the base of the

flow, rises to $Pe = 18.86$ at $\hat{z} = 1/2$ and then tends to a finite, but, large, value of $Pe = 430$ at the top. Note that in the case when $\mathcal{C} = 0$, the Péclet number will be similar over most of the range, but the singularity in pressure at the free-surface implies that $Pe \rightarrow \infty$ at $\hat{z} \rightarrow 1$. Since the diffuse interface separating high concentrations of large particles from high concentrations of fines, in figure 3.14, lies between $\hat{z} = 0.4$ and 0.6 , the Péclet number $Pe = 11.38$ at the lower end of this range and rises sharply to $Pe = 37$ near the top. As a result, the solution is much more rounded and diffuse at the bottom, which is a defining feature of the current theory.

3.8 Conclusions

This paper uses the refractive index matching technique to make detailed measurements of the trajectory of single intruders as they segregate through a matrix of differently sized grains in an oscillatory shear cell. A wide range of shear-rates, grain-sizes and grain-size ratios have been explored (as summarized in table 3.2) and four key observations have been made; (a) The segregation velocity magnitude f_{sl} scales linearly with the shear rate $\dot{\gamma}$ for both large and small intruders. (b) The rise velocity of large intruders scales linearly with size ratio R and shuts off when $R = 1$. (c) The percolation velocity of the small intruders has a linear dependence on $(R - 1)$ for size ratios close to unity, but develops a quadratic dependence at larger size ratios. (d) On average the trajectories of both the large and small intruders describe quadratic curves as they segregate through the cell.

These four observations combined with dimensional analysis suggest a simple functional form (3.22) for the segregation velocity magnitude. When (3.22) is substituted into equation (3.7) it implies that the small particle segregation flux

$$\mathbf{F}^s = \frac{\mathcal{B}\rho_*\dot{\gamma}\bar{d}^2}{\mathcal{C}\rho_*g\bar{d} + p} \left[(R - 1) + \mathcal{E}\phi^l(R - 1)^2 \right] \phi^s\phi^l\mathbf{g}, \quad (3.64)$$

is dependent of the shear-rate $\dot{\gamma}$, the local mean particle size \bar{d} , the intrinsic density of the grains ρ_* , the pressure p , the size ratio R , the gravitational acceleration vector \mathbf{g} and the local concentration of small particles $\phi^s = 1 - \phi^l$. In particular, this segregation flux is able to collapse all the intruder data collected in this paper using the same values of the non-dimensional coefficients \mathcal{B} , \mathcal{C} and \mathcal{E} . Moreover, when combined with the generalized diffusivity (3.34), which is based on Utter and Behringer's (2004) monodisperse Couette cell experiments, equation (3.64) can also quantitatively predict van der Vaart et al.'s (2015) index-matched shear cell experiment at intermediate concentrations, without introducing any fitting parameters, as shown in figures 3.13 and 3.14.

The non-dimensional coefficients \mathcal{C} plays a small, but, very important role in the theory. It is primarily introduced to remove the singularity in the segregation flux function (3.64) when the pressure p is equal to zero at the free surface. In particular, this is vital for the numerical method that is used to compute the results in figures 3.13 and 3.14. However, it is sometimes useful to make the approximation $\mathcal{C} = 0$ as it significantly simplifies the

Chapter 3. Scaling law for particle-size segregation in dense granular flows

mathematical formulation, and allows an exact solution (3.61) to be derived for the steady-state concentration distribution.

Particle-size segregation usually takes place in rapidly sheared free-surface flows, where the pressure is lithostatic. Interesting, when the lithostatic pressure distribution (3.25) is substituted into (3.64) the intrinsic density dependence and the magnitude of the gravitational acceleration $g = |\mathbf{g}|$ cancels out to leave the segregation flux

$$\mathbf{F}^s = \frac{\mathcal{B} \dot{\gamma} \bar{d}^2}{\mathcal{C} \bar{d} + \Phi(h-z)} \left[(R-1) + \mathcal{E} \phi^l (R-1)^2 \right] \phi^s \phi^l \check{\mathbf{g}}, \quad (3.65)$$

where $\check{\mathbf{g}} = \mathbf{g}/|\mathbf{g}|$ is the unit vector in the direction of gravity. This implies that gravity sets the direction for segregation, but it does not determine the time-scale for particles to segregate. This is consistent with Savage and Lun's (1988) statistical model for kinetic sieving and squeeze expulsion, in which the shear-rate sets the timescale for segregation, as it determines the rate at which small particles see gaps that they can percolate down into during the kinetic sieving process. The independence of (3.65) on the magnitude of gravity g is an indication that the timescale for a small particle to drop down through a gap under the action of gravity is short compared to the time that it takes to find a gap to percolate down into.

The non-dimensionalized vertical component of the segregation flux function (3.65) is plotted in figure 3.12(a). It is asymmetric in shape with an inflection point to the right of the maximum amplitude, with a skewness that becomes more pronounced as the grain-size ratio is increased. These asymmetric properties imply that for the same grain size ratio R , a single small particle intruder percolates downwards faster than a single large intruder is squeezed upwards, as shown in figure 3.12(b), and that this velocity asymmetry become more pronounced as the grain-size ratio is increased. These seemingly disparate behaviours are unified by the remarkably simple formulae for the ratio of the intruder segregation speeds (3.57) and the ratio of the intruder segregation times (3.58) at fixed size ratio R , which are both just dependent on the grain-size ratio (assuming that $\mathcal{C} = 0$).

The ability of the theory to match all the existing experiments that have been performed in the oscillating shear cell, suggests that the new scaling law for segregation derived in this paper might usefully be applied to other problems. In particular, the theory has the right pressure dependence in the segregation and diffusion terms to allow suppression of segregation in Golick and Daniels's (2009) annular shear cell experiments, as well as in Fry et al.'s (2019) DPM simulations. Further comparison is left to subsequent work, but potential users of the theory should note that the value of \mathcal{B} given in table 3.3 may need to be modified for flows in air, to correct for the buoyancy induced by the refractive index matched fluid in our experiments. According to Thornton et al. (2006) the presence of an interstitial fluid moderates the segregation by a factor of $\hat{\rho} = (\rho_* - \rho_*^f)/\rho_*$, where ρ_*^f is the density of the fluid. For the densities given in table 3.1, this would imply an enhancement factor of 1.7 times \mathcal{B} , for the theory to apply to subaerial flows, i.e. a value of $\mathcal{B} = 0.6365$. The value of \mathcal{B} may also have to be enhanced further, if the process of kinetic sieving proves to be more efficient in flows where

the direction of shear is not constantly being reversed. However, it is believed that the overall structure of the equations derived in this paper may find universal application to segregation problems in other configurations and in the absence of an interstitial fluid.

4 A conveyor belt experimental setup to study the internal dynamics of granular avalanches

Tomás Trehela¹ and Christophe Ancey¹

¹ Laboratory of Environmental Hydraulics, École Polytechnique Fédérale de Lausanne, Lausanne, Switzerland.

In preparation for *Experiments in Fluids*.

Doctoral candidate's contribution

The candidate participated actively in the setup's final stage of construction. The experiments, analyses and figures for this chapter were done by the candidate. The chapter was entirely written by the candidate, with editorial and structural comments from Prof. Ancey.

Abstract

We present a conveyor belt experimental facility to study the internal dynamics of stationary and uniform granular avalanches. To visualize within the granular bulk of these avalanches and determine their composition and velocity fields, we used the refractive index matching (RIM) technique in combination with particle tracking velocimetry and coarse-graining algorithms. In particular, RIM implementation posed various technical difficulties, hereby addressed, for the design and construction of the conveyor belt setup. To test and give the experimental setup a proof of concept, we carried out mono- and bidisperse granular avalanches in it. These avalanches showed distinctive flow regions and structures: (i) a convective-blunt front, (ii) a compact-layered tail and, in between them, (iii) a breaking size segregation wave structure. We found that bulk strain-rate, measured in terms of its tensor invariants, varied significantly between the flow regions and were bound to the flow characteristics. In terms of the flow velocity fields, the interpolated profiles were well-adjusted to a Bagnold scaling, despite considerable basal slip. We estimated a segregation flux field using recent developments on particle-size segregation. Along with vertical velocity changes and dilation, segregation flux

was markedly higher at the very front of the avalanche which suggests a connection between flow rheology and grain segregation. Therefore, our experimental setup and results showed potential for further theoretical developments on rheology and segregation coupled models.

4.1 Introduction

Conveyor belts are often used for granular material transportation in sediment extraction, mineral processing or logistic centers (Standish et al., 1991; Álvarez-Valero et al., 2009; Pane et al., 2019). In general, they can be described as mechanical rough-belts that drag materials from one place to another. On laboratory-scale, these transportation belts are particularly useful for long hydraulic sediment transport studies that require constant sediment inflow at a flume's inlet or sediment restitution (e.g., Armanini et al., 2005; Dhont and Ancey, 2018). If the static friction coefficient between the belt and the transported grains is surpassed, a particle-laden flow may be produced. Of course, such condition is undesirable in industrial processes or the mentioned sediment feeding system, but it presents an opportunity to study granular flows. For instance, a fine-tuned slip-drag condition could create a stationary granular flow, that resembles a flow moving downstream at the same speed it is being conveyed.

Granular flows propagation is commonly studied via dam-break or constant-flow-rate experiments over very long channels to allow flow development (for a review on these and other type of granular flow experiments, see Delannay et al., 2017). While simple and straight-forward, the front development in these experiments is brief and unstable. The wavefronts are known to accelerate, stabilize and then decelerate, hence traveling at a variable velocity that makes the wavefront difficult to capture with a moving camera. Despite being a specific flow condition, a steady quasi-static granular wavefront offers an ideal approach to study granular flows.

The internal dynamics of granular flows are crucial for their propagation. Internal changes in pressure, grain-friction or composition produce relevant differences in run-out distances (Roche et al., 2008; Mangeney et al., 2010; Kokelaar et al., 2014). This relevance has prompted the development of several techniques to visualize and measure within the granular bulk. Among the many techniques available for their use on laboratory-scale, the refractive index matching (RIM) is relatively cheaper and simpler to implement compare to other sophisticated techniques (Budwig, 1994; Wiederseiner et al., 2011a; Dijkstra et al., 2012; Sanvitale and Bowman, 2016). However, the visualization of the wavefront's internal dynamics using RIM can still be difficult. When the setup is not submersed, phase-separation, free-surface effects, and bubbles pose problems for an image acquisition that is usually done fairly away from the flow releasing point. To overcome most of these difficulties, it is advisable to submerge the setup in the RIM fluid, but a very large amount of fluid may be required for long inclined flumes, with the drawback of creating large unused fluid volumes when variable and high-slope experiments are required (van der Vaart et al., 2018a). Another well known difficulty for RIM implementation is the reduced number of possible matches for the technique. Fluid-particle RIM candidates are quite limited for dry granular flow applications, due to the fluid's

properties (Wiederseiner et al., 2011a; Dijkstra et al., 2012). Often, these fluids can be highly viscous or very dense and may include chemicals that produce adverse effects on setup and instruments. All of these difficulties must be considered in the design and construction of experimental setups that want to be used with the RIM technique.

Conveyor belts have been used to study granular flows experimentally (e.g., Davies, 1990; Perng et al., 2006; Martínez, 2008; Marks et al., 2017; van der Vaart et al., 2018a). Recently and in particular, the articles of Marks et al. (2017) and van der Vaart et al. (2018a) focused on particle-size segregation, a frequent phenomenon observable in granular media. Polydisperse granular materials are prone to separate themselves by their particles' sizes (Gray, 2018). In granular flows over an incline, large particles are often encountered at the flow's front and surface, and small ones are more likely to be found at its tail and base (Johnson et al., 2012; Gray, 2018). This inversely-graded arrangement is the reason for which, a stationary granular flow condition with a well-defined front is particularly helpful to study size segregation, as it could shed light on the relation between flow and segregation. In continuum-based models, segregation fluxes are formulated as relative velocities between the bulk and its species (Gray and Thornton, 2005; Gajjar and Gray, 2014; Trehwela et al., 2020a). Since conveyor belts create a condition where the average bulk velocity in the flow direction is determined by the belt velocity, the relative movement between grains at the front can be easily observed. Following this simplified flow idea, Marks et al. (2017) carried out perpetual avalanche experiments in a two-dimensional conveyor belt configuration to describe grain-size segregation processes. However, strict two-dimensional configuration has shown to produce artifacts that are not observed in three dimensional configurations, i.e., non-negligible wall effects, convection cells and restrictions for small particle percolation (Thomas and Vriend, 2019; Trehwela et al., 2020b). (van der Vaart et al., 2018a) found mobility-feedback dynamics similar to those of (Marks et al., 2017) but on a three-dimensional conveyor belt configuration. These recent studies have also pointed-out pending challenges, such as the implication of breaking size segregation waves in particle-size segregation theories (Gray, 2018), and intermediate or reverse segregation (Thomas and D'Ortona, 2018).

In this paper we present a three dimensional conveyor belt experimental setup to study stationary granular avalanches. This setup is a second version of the prototype used by van der Vaart et al. (2018a). Our setup's design addressed various technical difficulties, observed in the previous prototype. Two experimental sets of mono- and bidisperse granular flows were carried out to study perpetual granular avalanches. A qualitative and quantitative description of the stationary granular flows, in terms of bulk's composition, velocity profiles, strain-rate tensor invariants and segregation flux, is provided as a proof of concept that this setup can be useful to study granular flows dynamics and study size segregation phenomena.

4.2 Theoretical framework

4.2.1 Granular flow equations

The flow of a granular material of intrinsic density ρ_* down an incline can be described using the mass and momentum equations

$$\frac{\partial \rho}{\partial t} + \nabla \cdot (\rho \mathbf{u}) = 0, \quad (4.1)$$

$$\frac{\partial (\rho \mathbf{u})}{\partial t} + \nabla \cdot (\rho \mathbf{u} \otimes \mathbf{u}) = \nabla \cdot \boldsymbol{\sigma} + \rho \mathbf{g}, \quad (4.2)$$

where $\rho = \Phi \rho_*$ is the bulk's density at a constant solids volume fraction Φ , \mathbf{u} is the velocity field, \otimes is the dyadic product, $\boldsymbol{\sigma} = -p\mathbf{1} + \boldsymbol{\tau}$ are the Cauchy stresses and \mathbf{g} is gravity. $\boldsymbol{\sigma}$ can be decomposed by the pressure p , multiplied to the identity tensor $\mathbf{1}$, and $\boldsymbol{\tau}$ the deviatoric stress tensor.

A conveyor belt flow configuration, that creates a shallow, steady, uniform and inclined granular avalanche, simplifies Eq. 4.2 to its longitudinal and vertical components as

$$\frac{d\tau_{xz}}{dz} = -\rho g \sin \theta, \quad (4.3)$$

$$\frac{d\sigma_z}{dz} = \rho g \cos \theta, \quad (4.4)$$

where θ is the inclination angle. We can integrate Eq. 4.3 and 4.4 for the case of a flow of height h that satisfies a stress-free condition at $z = h$ to obtain

$$\tau_{xz}(z) = \rho g \sin \theta (h - z), \quad (4.5)$$

$$\sigma_z(z) = -\rho g \cos \theta (h - z). \quad (4.6)$$

Combining the found expressions with the $\mu(I)$ constitutive relation $\tau = \mu(I)\sigma$ we obtain that $\mu(I) = \tan \theta$. Then, a relation between I and θ , derived from the empirical law of Jop et al. (2006), can be used to calculate the inertial number

$$I = I_0 \frac{\tan \theta - \mu_1}{\mu_2 - \tan \theta} \quad (4.7)$$

where I_0 , μ_1 and μ_2 are empirically-determined parameters. For this law to be valid, a steady-

uniform flow is only achieved for $\mu_1 < \tan \theta < \mu_2$ for which the inertial number definition (MiDi, 2004)

$$I = \frac{\dot{\gamma} d}{\sqrt{\sigma_z} / \rho}, \quad (4.8)$$

where $\dot{\gamma} = |du/dz|$ is the shear rate and d is the particles' diameter. This definition together with Eq. 4.8 and the basal velocity condition $u_0 = u_b$ for the belt velocity, yields a Bagnold-like velocity profile

$$u(z) = -u_b + \frac{2I\sqrt{g\cos\theta h^3}}{3d} \left\{ 1 - \left(1 - \frac{z}{h} \right)^{3/2} \right\} \quad (4.9)$$

where I is constant and calculated using Eq. 4.7. This theoretically-determined velocity profile is characteristic for steady and uniform granular flows of monodisperse grains. However, granular materials are usually polydisperse and as such, a bidisperse granular flow may exhibit a different velocity profile due to segregation-induced grain rearrangement.

4.2.2 Size segregation equations

The internal dynamics of the stationary granular avalanches were studied in terms of size segregation via a continuum approach, hence particles' concentration and velocity fields. For a bidisperse granular mixture of grains of different diameters, the volumetric concentrations of the grains species satisfy

$$\sum_v \phi^v = 1, \quad (4.10)$$

where ϕ^v is the partial volume fraction for each species $v = \{s, l\}$, which are characterized by a diameter d^v . Then, the bidisperse size segregation equation for the v species is described according to (Gray, 2018)

$$\frac{\partial \phi^v}{\partial t} + \nabla \cdot (\phi^v \mathbf{u}) + \nabla \cdot \mathbf{F}^v = \nabla \cdot (\mathcal{D}_{sl} \nabla \phi^v), \quad (4.11)$$

where \mathbf{u} is the bulk velocity and $\mathbf{F}^v = f_{sl} \phi^s \phi^l \mathbf{g} / |\mathbf{g}|$ are the segregation fluxes, which are oriented to the direction of gravity and satisfy

$$\sum_v \mathbf{F}^v = 0. \quad (4.12)$$

In a stationary regime and in the absence of diffusion we can simplify Eq. 4.11 to obtain

$$\begin{aligned}\mathbf{u}^l - \mathbf{u} &= -f_{sl}(\phi^s)\phi^l, \\ \mathbf{u}^s - \mathbf{u} &= f_{sl}(\phi^s)\phi^s,\end{aligned}\tag{4.13}$$

where f_{sl} corresponds to a theoretical segregation flux function for large and small particles. This function has been proposed to be cubic (Bridgwater et al., 1985), quadratic (Dolgunin and Ukolov, 1995), asymmetric (Gajjar and Gray, 2014; van der Vaart et al., 2015) and highly non-linear (Trehwela et al., 2020a). Most important is the asymmetric nature of the segregation process, small particles segregate faster than their large counterparts, that has been described theoretically and has been observed in both numerical and laboratory experiments (Gajjar and Gray, 2014; van der Vaart et al., 2015; Jones et al., 2018).

For the present work we used the coarse-graining technique to obtain the bulk's density ρ , partial concentrations ϕ^v and velocity fields \mathbf{u} from our discrete particle positions \mathbf{r}_i and velocities \mathbf{u}_i . The velocity fields for each species \mathbf{u}^v were also computed. With these computations and other assumptions, we calculated f_{sl} following the recent scaling law presented by Trehwela et al. (2020a),

$$f_{sl} = \mathcal{B} \frac{\rho_* g \dot{\gamma} d^2}{\mathcal{C} \rho_* g d + p} \mathcal{F}(R, \phi^s),\tag{4.14}$$

where $\mathcal{B} = 0.3744$ and $\mathcal{C} = 0.2712$ are two constants introduced and determined in their work. \mathcal{F} is a function that depends mostly on the size ratio $R = d^l/d^s$, for intermediate values of ϕ^s , and will be considered to be equal to $(R - 1)$. $\dot{\gamma}$ is the shear rate, $d = d^s\phi^s + d^l\phi^l$ is the concentration-averaged diameter and $p = \rho_* g \Phi(h - z) \cos \theta$ is the pressure, considered to be lithostatic for a flow of height h . We derived an expression for d as a function of ϕ^s which resulted in

$$d = R d^s \left\{ 1 - \left(1 - \frac{1}{R} \right) \phi^s \right\} = R d^s d_\phi.\tag{4.15}$$

Therefore, by replacing the latter in Eq. 4.14 we determined a simplified segregation flux function

$$f^s = \mathcal{B} \frac{\dot{\gamma} (R d^s d_\phi)^2}{\mathcal{C} R d^s d_\phi + \Phi(h - z) \cos \theta} (R - 1),\tag{4.16}$$

which could be entirely determined using our experimental images. The shear rate calculation is detailed in the next subsection and was done with the notion of the strain-rate tensor

invariants.

The usage of the scaling proposed by Trehwela et al. (2020a) was based on the fact that it captures well the asymmetric nature of the size segregation process, where small particles percolate at a different time-scale than the rise of large particles. Also, in their scaling, the segregation time-scale is mainly set by shear rate $\dot{\gamma}$ and it is affected by size ratio R and pressure distribution p .

4.2.3 Strain-rate tensor invariants

Based on the velocity field \mathbf{u} , the strain-rate tensor is defined as

$$\mathbf{D} = \frac{1}{2}(\nabla \mathbf{u} + (\nabla \mathbf{u})^T), \quad (4.17)$$

where T denotes the transpose. The first invariant of the strain-rate tensor, also called dilation, can be calculated as

$$I_{\mathbf{D}} = \frac{1}{2}\text{tr}(\mathbf{D}) = \frac{1}{2}(\nabla \cdot \mathbf{u}). \quad (4.18)$$

A tensor decomposition determines the deviatoric strain-rate tensor $\mathbf{S} = -\frac{1}{3}I_{\mathbf{D}}\mathbf{1} + \mathbf{D}$ useful for the calculation of the second invariant of the strain-rate tensor,

$$II_{\mathbf{D}} = \left(\frac{1}{2}\text{tr}(\mathbf{S}^2) \right)^{1/2}, \quad (4.19)$$

where $\dot{\gamma} = 2II_{\mathbf{D}}$. Throughout this paper, references or discussions on the shear rate are also referring to the strain-rate tensor's second invariant.

4.3 Materials and techniques

4.3.1 Refractive index match

Most granular materials are opaque, a property that restricts their visualization to their boundaries. Even in cases where grains are transparent, refractive index differences between the surrounding medium and the grains' material obstruct the visualization within the granular bulk. To overcome such natural restriction, a refractive index match between the grains' material and the interstitial fluid can be achieved under controlled conditions, usually in a laboratory environment. Such technique, called refractive index matching (RIM) has been used to study not only granular flows, but fluid flows in general (Budwig, 1994; Li et al., 2005;

Chapter 4. A conveyor belt setup to study granular avalanches

Wiederseiner et al., 2011a; Dijkstra et al., 2012; Bai and Katz, 2014; Clément et al., 2018; Rousseau and Ancey, 2020).

For the present study we used a RIM mixture of borosilicate glass, and a fluid solution of ethanol and benzyl-alcohol. Their refractive indexes, densities and suppliers, are detailed in Table 4.1. Two additional RIM mixtures were initially considered for this study, but were disregarded due to the interstitial fluids properties. The first alternative was a Triton X-100 and poly(methyl methacrylate) (PMMA) match (see, Dijkstra and van Hecke, 2010; Wiederseiner et al., 2011a; Dijkstra et al., 2012). We were discouraged to use it due to the fluid high viscosity ($\eta = 270$ cP) and a low relative density between particles and fluid, $\rho' = (\rho_p - \rho_f) / \rho_p = 0.102$, that restrained granular processes we were interested in. The second alternative was an aqueous sodium iodide (see, Narrow et al., 2000; Bai and Katz, 2014; Clément et al., 2018) and borosilicate glass mixture, but the interstitial fluid was too dense and the grains showed positive buoyancy. After the evaluation of these alternatives, we committed to the borosilicate glass, ethanol and benzyl-alcohol match, which was also recently used by Rousseau and Ancey (2020). The viscosity of our mixture was substantially lower than Triton X-100's, $\eta \approx 3$ cP, and the density difference between borosilicate and the mixture was negative and sufficient to replicate the physics of dry granular flows $\rho' \approx 1.34$.

Material	n_r	ρ_*	Supplier
Borosilicate glass	1.4726	2.23	Schäfer Glas
Benzyl alcohol	1.5396	1.044	Acros Organics
Ethanol	1.3656	0.789	Fisher Scientific

Table 4.1 – Refractive indexes n_r , intrinsic densities ρ_* and suppliers of the materials used for our RIM experiments.

An initial fluid mixture in a 35:65 weight proportion of ethanol and benzyl-alcohol, as reported by Chen et al. (2012), was used as a first approximation to the desired refractive index of the glass beads, i.e., $n_r = 1.4726$ (Tab. 4.1). From this starting point, we tuned the refractive index of the mixture by adding small volumes of either ethanol or benzyl-alcohol. The n_r was constantly measured during its fine-tuning with a Atago RX 5000 α refractometer in a 20 °C temperature-controlled environment. However, a very precise value was unattainable, mainly due to the large volume required for our experiments (≈ 40 l). For such a large volume, the mixing process was done with a motorized mixer, therefore, this index-related difficulty was related to the mixing and evaporation rates of the ethanol and benzyl-alcohol mixture. The mixing process created sufficient heat and bubbles to enhance the evaporation rate of ethanol, in comparison to that of benzyl-alcohol, which was lower. In addition, the creation of bubbles carried vaporized ethanol to the surface. A lower mixing rate was not sufficient to solve the problem, a low homogenization rate was enough to allow evaporation of ethanol that tended to be at the surface due to its lower density. We sorted out all these difficulties by simplifying our process. We aimed to obtain a lower refractive index than 1.4726, so that evaporation would adjust the index to this value for us. Although this took the control of the refractive

index away from us, the results were satisfactory and within a tolerance of 1.472 ± 0.0005 the match was enough.

4.3.2 Image acquisition

The RIM technique is often used for image acquisition and analysis. To visualize the granular matrix, the matched granular-fluid mixture was mixed with Rhodamine 6G (Acros Organics), a fluorescent agent. When exposed to a green laser sheet, the rhodamine was excited and by contrast, the grains appeared to sight as black circles. This combination of instruments and techniques is also referred as granular planar laser-induced fluorescence (PLIF) in the literature (Sanvitale and Bowman, 2012, 2016).

We used a 4W Viasho laser with a wavelength $\lambda = 532$ nm to create the laser sheet. Images of the laser-contrasted black circles were acquired with a Basler A403k camera and a 28 mm Nikon lens mounted to it. Recording was performed at a fixed frame rate of 40 frames per second for all experiments. The resolution for our images was of 2352x600 pixels.

4.3.3 Particle tracking and coarse-graining

The sequences of images that captured the moving black circles were analyzed using circle identification and a particle tracking algorithm. The *imfindcircles* algorithm included in Matlab 2019a was used to find circles of various sizes. After all particles positions were determined for the entire image sequence, they were correlated using the tracking algorithm of Crocker and Grier (1996) to obtain particle trajectories $\mathbf{r}_i(x, z, t)$ along time, hence particle velocities $\mathbf{u}_i(x, z, t)$.

A recurrent issue when studying discrete particle flows is to translate punctual or step-wise information to continuous profiles or fields that can be comparable to predictions of continuum models. To overcome this issue, coarse-graining techniques have been used to translate experimental and numerical results of discrete granular flows to continuum fields (e.g., Weinhart et al., 2012; van der Vaart et al., 2015; Tunuguntla et al., 2016). The advantages of the coarse-graining technique are multiple (Goldhirsch, 2010), among them: (i) it is possible to obtain continuous, smooth and differentiable fields and profiles, a particularly helpful feature close to the boundaries; (ii) the used coarse-graining functions are required to be differentiable and integrable so the obtained fields satisfy both mass and momentum conservation. For our experimental analyses, we used a 4th degree Lucy polynomial (Lucy, 1977), which has been used in discrete particle simulations (Tunuguntla et al., 2016).

4.4 The conveyor belt experimental setup

We designed and built a conveyor belt flume to study stationary granular flows, of which a spatial scheme is shown in Fig. 4.1. This setup's core consists in an enclosed aluminium flume

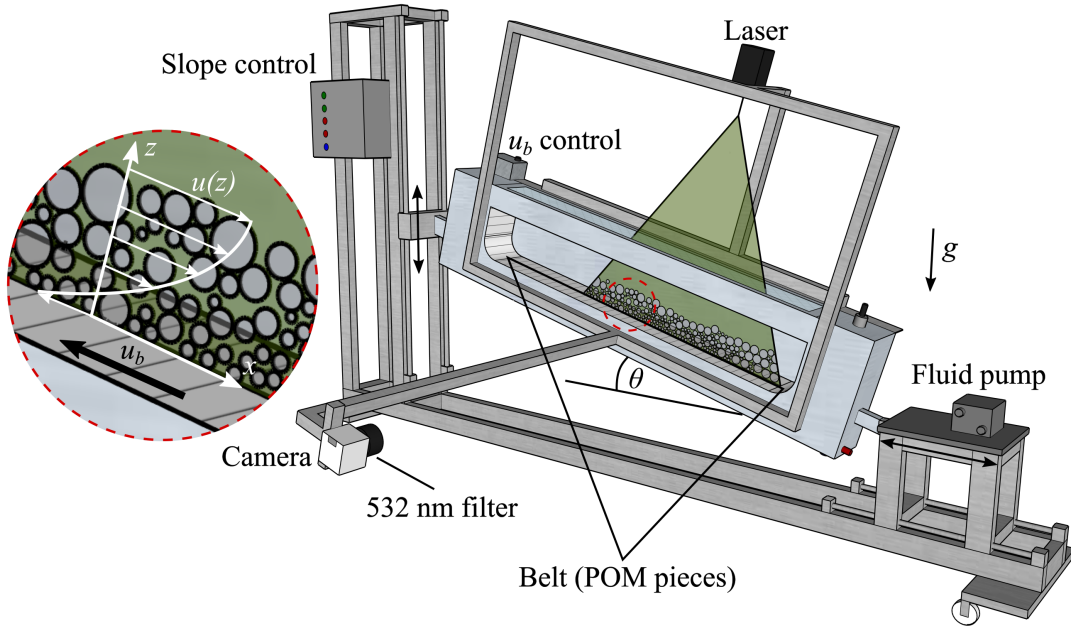


Figure 4.1 – Diagram of the conveyor belt setup. The enclosed aluminium flume, shown at the center, is closed by a rectangular windowed lid that allows the passage of the laser sheet from above. 300 independent POM pieces form the rough conveyor-belt that circulate around the flume with the guidance of grooves encaved into the front and back walls of the aluminium flume. To the left, the slope θ control sets the vertical position of the flume's left-end, along with its right end and a sliding chariot where the fluid pump rests. At the flume's left-end, on top of it, the belt velocity is controlled by an electronic system (denoted as u_b control in the figure). Image acquisition is carried out by a Basler A403k camera placed at the front of the flume. The camera was equipped with a Nikon 28 mm lens and a 532 nm filter.

of dimensions 141 cm length, 14 cm width and 42 cm height. A rectangular panel with a glass window closes and seals the setup from above. This top glass window allows the laser, attached to the flume, to illuminate the inside of the flume perpendicularly. Inside the flume, two grooves carved on the front and back panels allow the movement of 300 independent pieces that form the conveyor belt. The grooves create a circuit and guide these pieces to move in the longitudinal direction of the flume and around four transversal aluminium rollers, one pair located at each end of the aluminium flume. Both roller pairs are arranged vertically to create walls that confine the granular material to a conveyed volume over the belt moving pieces. This conveyed volume corresponds to the effective volume where the granular material can be conveyed by the belt and it has dimensions of 104 cm length, 10 cm width and 15 cm height. The front wall of the aluminium flume has a glass window to allow image acquisition and visualization of the entire conveyed volume. At each end of the aluminium structure, behind the roller pair, a mixer is located to aid fluid homogenization. Various valves, beneath and on top of the setup, help the setup filling and emptying processes.

An analog electro-mechanical system sets the slope by moving vertically the flume's left-end,

its right-end moves simultaneously in the horizontal direction with the help of an attached chariot. The slope can be set continuously and has a wide range of values but it cannot be set completely horizontal. Very low or very steep slopes during operation are unadvised and impractical, as particles could overflow the upper rollers and create mechanical issues.

Each independent piece of the actual belt is a polyoxymethylene (POM) half-cylinder screwed to an aluminium band. The purpose of these assemblable pieces is to be able to change the roughness of the belt by replacing the POM half-cylinders. For our experiments, we used a uniform roughness given by half-cylinders of 4 mm radius. The pieces are put in between the two grooves, one beside the next, and are kept in place by the compression the very same pieces apply on each other while restrained vertically by the grooves.

A motor located behind the setup rotates the bottom-left roller, which has a geared wheel that pushes the POM pieces between the grooves. Half of the pieces have two bolts beneath them so that the dented wheel pushes them, hence moving the belt. Bolted and non-bolted pieces are arranged alternatively to avoid the rupture of the dented wheel, the roller, or the POM pieces. The motor speed is controlled with a dimmer switch that can set a continuous range of values for the belt velocity u_b . However, the belt's velocity value is not directly given by the analog controller, so for our experiments we measured it with a sensor that captures the motor axis revolutions as a function of time. These measurements were used to calculate u_b with the radius of the dented wheel.

As the reader can infer from the previous description, the setup is quite complex and has intricated mechanisms. Multiple difficulties arose during the construction and testing stages. While many of these were successfully solved, other are pending challenges.

4.5 Experimental dataset

Exp. number	d^s	d^l	Φ^s (%)	θ (°)	u_b (cms ⁻¹)
1 (monodisperse)	6	-	100	15	8.16
2 (bidisperse)	6	14	90	15	7.74
3 (bidisperse)	6	14	80	15	7.76
4 (bidisperse)	6	14	70	15	8.24
5 (bidisperse)	6	14	60	15	7.62
6 (monodisperse)	8	-	100	15	7.94
7 (bidisperse)	8	14	90	15	7.69
8 (bidisperse)	8	14	80	15	8.09
9 (bidisperse)	8	14	70	15	7.82
10 (bidisperse)	8	14	60	15	8.16

Table 4.2 – Parameters of the experimental dataset. Φ^s is the overall small particle partial concentration over the bulk, the slope θ and the measured speed of the conveyor belt u_b .

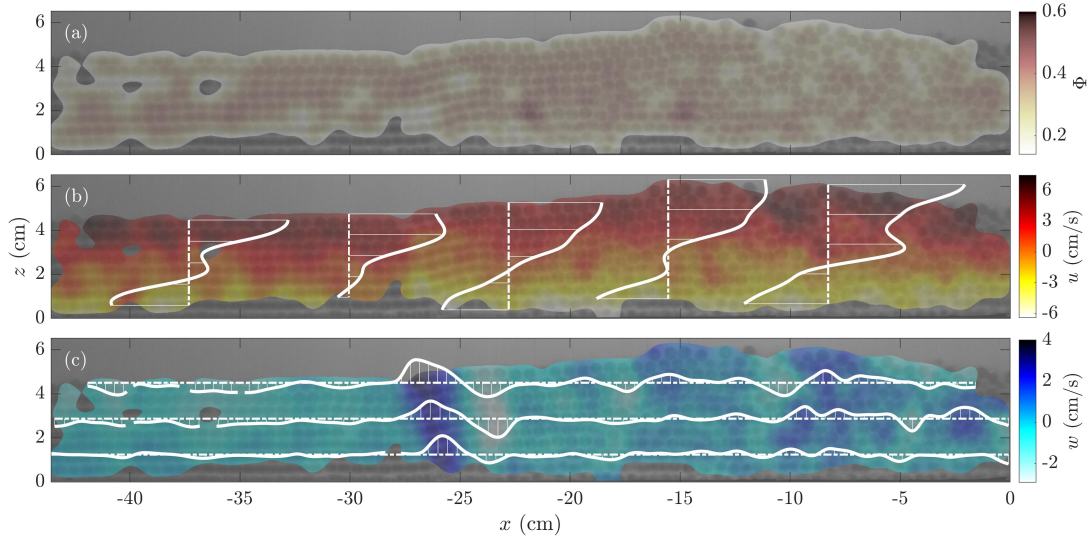


Figure 4.2 – (a) Bulk volumetric concentration Φ , (b) longitudinal u and (c) vertical w velocity fields at $t = 229.25$ s for Exp. 1 (see Tab. 4.2). Longitudinal distances are measured from the right-end of the flume’s horizontal part. Two differing flow sections can be distinguished from the images and separated at $x \approx -25$ cm: (i) $x \lesssim -25$ cm, a well-arranged particle flow flowing in layers, and; (ii) $x \gtrsim -25$ cm, a convective-bulged front where particles recirculate. The discontinuous lines correspond to (a) vertical or (b) horizontal profiles of the respective velocity field, with values plotted with continuous white lines. These values are only shown to illustrate relative fluctuations along the profiles and visualize their shape.

The presented conveyor belt was used to study the internal dynamics of granular flows under two cases, mono- and bidisperse flows. Due to the particular flow configuration imposed by the experimental setup, the granular flows were studied as stationary granular avalanches. The experiments were characterized by their slope θ and belt velocity u_b . Both were manually set and controlled using the analog-electronic controls shown in Fig. 4.1. These controls were not capable to set θ and u_b to predetermined values, so we measured both parameters for each experiment. θ was measured directly with an inclinometer over the flume, so we could set it to the desired value beforehand. All the experiments were carried out with an inclination of 15° . u_b was measured with a sensor that captured the motor axis revolutions during the experiment, so we could not adjust u_b to a precise or default value. This restriction meant that velocity was a result, measured from the experimental conditions and not a parameter that we were able to set in advance. However, we could set a u_b condition for all experiments using the values marked in the analog u_b control-knob. We set the knob approximately at a middle speed in all experiments.

Two monodisperse experiments were initially carried out to determine a base state for later comparison with bidisperse experiments. The granular materials used for these two runs was a 6 kg bulk formed of borosilicate beads of either $d^s = 6$ or 8 mm diameter (see Exps. 1 and 6 in Tab. 4.2). For these experiments, we determined bulk concentrations, velocity fields as

functions of time. Afterwards, we time-averaged these fields to obtain general trends and capture averaged processes that individual frames were not able to show.

The main body of experimental work consisted in eight quasi-stationary bidisperse granular avalanches. To include large particles into the bulk, we replaced a partial weight of small particles with large particles to keep the same weight for all experiments and only change Φ^s . Therefore, general small particle concentration Φ^s ranged from 90 to 60%, with large particle concentration varying complementarily, i.e., $\Phi^l = 100 - \Phi^s$. Since both species have the same intrinsic material density ρ_* , the bulk general volume concentration remained the same for all experiments. In addition to bulk concentrations and velocity fields, for bidisperse experiments, local volume concentrations of small ϕ^s and large particles $\phi^l = 1 - \phi^s$ were determined from the images using the coarse-graining technique (see §4.3.3).

Before data acquisition the experiment was set to meet a uniform and, if possible, stationary flow condition. To set an experiment, we first prepared the granular bulk. Small and large particles, in the case of a bidisperse experiment, were added in the desired proportion. After the particles were weighted and added in the right proportion, they were put and mixed inside the flume that rested horizontally. A horizontal position created no particle flow, that could alter our mixed bulk, and facilitated the filling process. We were inclined to mix the bulk before each experience to have an homogeneous and easily repeatable initial condition. The fluid pump shown in Fig. 4.1 was used to fill the flume with the already refractive index matched fluid. Only when we finished the filling process we inclined the flume and turned on the belt. Once the quasi-stationary flow condition was achieved, we started the image acquisition. Such flow condition was met when the flow height profile and the avalanche front did not vary notably for several minutes. Image acquisition was performed for precisely 5 minutes, capturing 12000 frames per run. An experiment was considered finished after the recording, and then the flume was brought back to an horizontal position where we emptied it for the next experiment preparation.

Due to the length of the flume and the selected d^s for the experiments, the length of the region of interest (ROI) for the image acquisition did not coincide to the flume's length. Our experimental images only captured ~ 44 of the flume's 104 cm length. We decided to focus our acquisition on the flow's front, at the right-end of the flume. Therefore, our experimental results only present 42% of the whole bulk. A full-extension acquisition would have only reduced our resolution, without gaining much knowledge on the front flow dynamics, since in most experiments, recirculation of large particles was restricted to the frontmost third part of the flume and the rest of the flow exhibited a similar behaviour to that of the ROI left boundary. Despite this decision, we were still able to capture various phenomena.

4.5.1 Belt velocity

Ambiguously, u_b could be interpreted as a parameter or a measurement. Although u_b was set analogously before the recording of the experiment, we saw that the value varied with θ , the

load of the belt and the friction imposed by the pieces. As we described in §4.4, there were many effects that could increase the motor's exertion. Even if the conveyor belt ran smoothly, we were not able to differentiate the degree of exertion between experiments. Instead of doing a calibration of u_b , that could led us to incorrect results if the exertion of the motor varied after various experiments, we decided to measure the velocity directly after the desired stationary regime was achieved.

The experimental dataset for this article is summarized in Table 4.2 and the measured u_b values are shown in its last column. Despite they were manually set, they did not vary immensely ($> 3\%$) with a mean value of 7.922 cm s^{-1} and a standard deviation of 0.225 cm s^{-1} .

4.6 Results

4.6.1 Monodisperse experiments

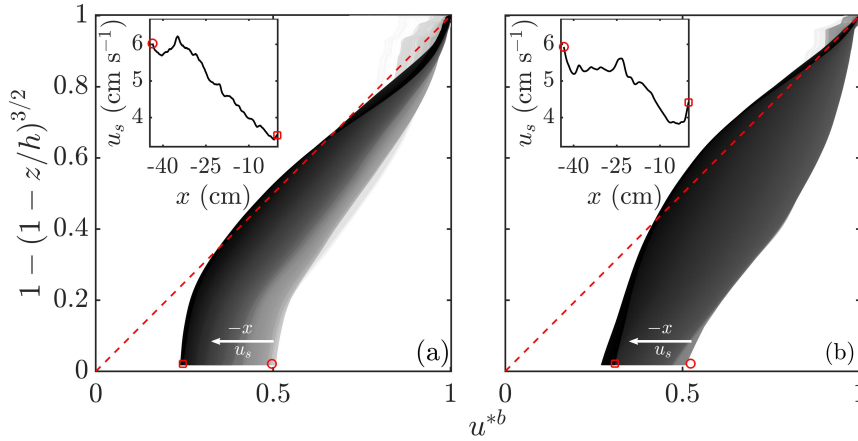


Figure 4.3 – Normalized velocity profiles u^{*b} (Eq. 4.20) for 6 mm (a) and 8 mm (b) monodisperse experiments (Exps. 1 and 6 in Tab. 4.2). The profiles are plotted in grayscale from white to black, from left to right of the captured region of the flow, respectively. In both plots, the identity line is plotted using a segmented red line. To emphasize the change in basal slip, the slip velocity u_{slip} is plotted in the inset of each subplot. The basal condition at the left- and right-ends of the flow are plotted with a red circle and square, respectively, to show the changes on basal slip conditions shown in the insets.

The monodisperse avalanches showed two distinctive flow sections. Towards the slope direction, at the right-end of the flume, the flow exhibited a convective bulged region where particles recirculated. Henceforth, this region will be addressed as the flow's convective or dilated front. Towards the other end of the flume, particle flow transitioned into a well-arranged structure of particle layers that moved on top of each other (layered flow). To illustrate these flow regions, we show an experimental image taken at $t = 229.25 \text{ s}$ in Fig. 4.2. We plotted on top of the experimental image: the bulk volumetric concentration, the longitudinal (in the direction of the flow) velocity and vertical velocity fields. In Fig. 4.2 we can see in the back-

ground the particle structures and a glimpse of the described flow sections can be observed. Bulk concentration varies between the described regions in general. The front shows a more diluted flow ($\Phi \approx 0.3$), whereas the tail is more concentrated ($\Phi \approx 0.5$). The flow's height h shows marked differences, height at the front reaches its maximum at $h = 6$ cm ($\sim 10d^s$) while at the back is close to 4 cm ($\sim 7d^s$).

To highlight some sections of the velocity fields, we plotted profiles along the cartesian direction (see continuous white plots in Fig. 4.2(a) and (b)). From the measured velocity fields we observed a quasi-uniform behaviour for u , with particles at the top moving faster than those at the bottom and an important basal-slip condition, which was to be expected. Vertical velocity w profiles were notably less consistent along the flow, where we observed much more vertical movement of particles in the flow's front than in its back, where particle layers barely moved on top of each other. It was possible to separate the two mentioned flow sections at $x \approx -25$ cm, measured from the right-end of the horizontal section of the flume. Sudden changes of $w \sim 4$ cm s⁻¹ marked the transition, a breaking point or barrier, from where particles started to recirculate within the dilated front. Only particles that were tightly attached to the belt managed to escape the convective front and, after reaching the left-end of the flume, were reincorporated to the stationary avalanche.

Due to the quasi-steady nature of the velocity fields and the sufficiently long experimental runtime, averaged fields were calculated to quantify our general observations. When time-averaged, the velocity fields became smoother and the \bar{u} profiles showed a consistent behaviour along the longitudinal direction. In general, the horizontal velocity profiles $\bar{u}(z)$ showed Bagnold-like characteristics but subject to a strong basal slip. In Fig. 4.3 we show a normalized velocity profile u^{*b} defined as

$$u^{*b} = \frac{\bar{u} - u_b}{u_h - u_b} \quad (4.20)$$

where u_h is the surface particle velocity at $z = h$, and u_b is the measured belt velocity (see u_b in Tab. 4.2). Therefore, u^{*b} is the time-averaged velocity field u normalized to the velocity difference between the belt and the surface, and it is plotted as a function of $1 - (1 - z/h)^{3/2}$ (Fig. 4.3). We considered this expression for the normalized velocity to show the influence of basal slip u_s on the overall velocity profile, which declines as we approach $z = h$. Close to the flow surface, most u^{*b} profiles adjust well to $1 - (1 - z/h)^{3/2}$, which is a characteristic of a Bagnold-like profile (Bagnold, 1954; Silbert et al., 2001). In terms of longitudinal variation of the profiles, we see that towards the front, basal friction increased and slip is at its minimum (see Fig. 4.3 (a) and (b) insets). The observation is shown in Fig. 4.3, where darker profiles adjust progressively better to the identity line (segmented red line in Fig. 4.3) as we approach the flume's right-end ($x = 0$).

We determined the strain-rate tensor invariants to quantify how dilated or sheared were the two flow regions. In Fig. 4.4 we show the time-averaged dilation I_D and shear rate II_D fields,

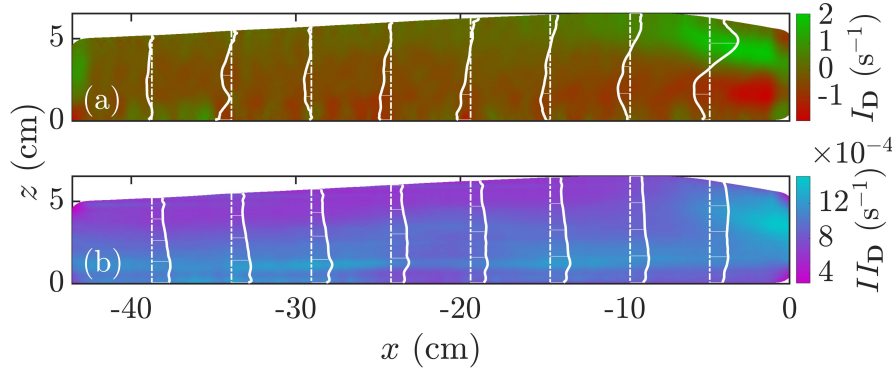


Figure 4.4 – Strain-rate tensor invariants fields: (a) dilation I_D and (b) shear rate II_D . The vertical discontinuous lines corresponds to vertical profiles and the corresponding values of the strain-rate tensor invariants are plotted with continuous white lines.

which corresponds to the averaged first and second invariants of the strain-rate tensor (as detailed in §4.2.3). Our results indicate that the front is highly-sheared and dilated, with a marked vertical gradient for I_D and constant II_D at the very front. To the back of the front, I_D fluctuates around 0 and II_D shows a negative gradient towards the flow surface, with higher values at the bottom as we would expect from the imposed boundary condition. Qualitatively, dilation and shear are particularly higher in regions where flow height is high as well and Φ is low, right at the convective-front. These observations are also related to low u_s values, as seen in Fig. 4.3. A decrease on the basal slip could explain the front bluntness and dilation, due to a more effective shear transmission from the belt to the bulk.

4.6.2 Bidisperse experiments

Despite the relative inclusion of more large particles, in terms of Φ^l , the avalanches maintained consistent bulk dynamics to those of monodisperse experiments, especially for low large particle concentration experiments ($\Phi^l = 10\text{-}20\%$, i.e., $\Phi^s = 90\text{-}80\%$). In low Φ^l experiments, the flow's convective-front confines large particles within itself, restraining particle recirculation. However, in experiments with higher Φ^l , the well-defined regions observed at low concentrations and monodisperse experiments become less evident and other structures emerge. Large particles are often dragged upstream, past the transition between the dilated-front and well-arranged regions, and alter the structures before detailed. Nonetheless, when we time-average the velocity and concentration fields, we observe the convective-front more clearly. Large particle are still found predominantly at the surface and the front of the flow, as a result of strong segregation flux in the middle of the bulk.

Figure 4.5 shows the time-averaged small particle concentration fields of our experiments. As expected from size segregation, the time-averaged concentration fields show an inversely-graded bulk towards the downstream-end of the flume. We can infer from Fig. 4.5 that experiments with smaller d^s , i.e., larger R , are more effective to confine large particles to the

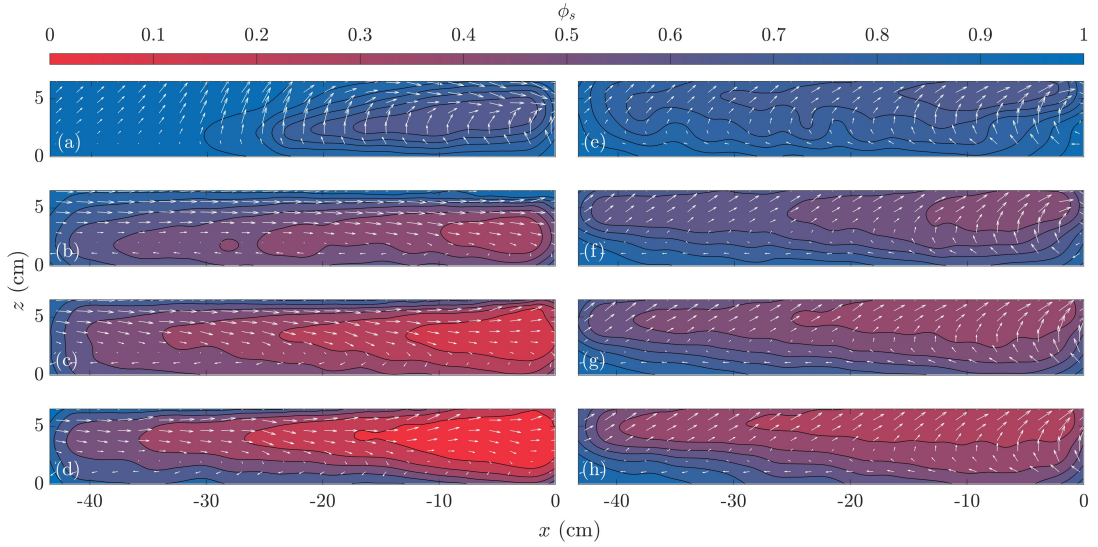


Figure 4.5 – Small particle concentration ϕ^s fields for: (a)-(d) Exps. 2-5 and (e)-(h) Exps. 7-10, respectively. The small particle general weight concentration decreases from 90, (a) and (e), to 60%, (d) and (h). The white arrows represent the normalized velocity fields $\bar{u}/\max_{\forall x,z} \bar{u}$ and $\bar{w}/\max_{\forall x,z} \bar{w}$.

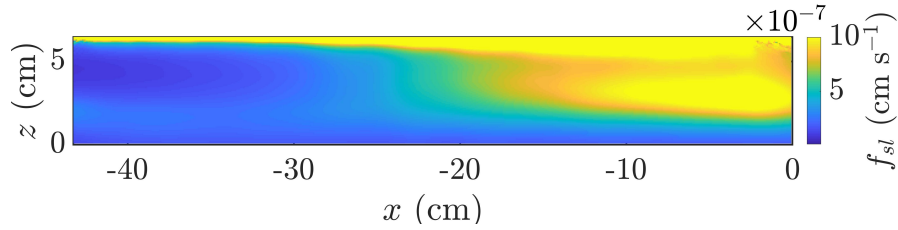


Figure 4.6 – Segregation flux f_{sl} for the $\Phi = 90\%$ experiment (Exp. 2, Tab. 4.2). f_{sl} was calculated using the scaling suggested by Trehwela et al. (2020a) and simplified in Eq. 4.14.

front of the flow. This confinement is due to a relatively faster segregation f_{sl} for larger R . To confirm this supposition we determined the segregation flux f_{sl} with the scaling presented in Eq. 4.14 (Fig. 4.6). For this calculation we supposed a hydrostatic pressure distribution, the concentration and $\dot{\gamma} = 2I\mathbf{D}$ fields determined from coarse-grained experimental data. Results presented in Fig. 4.6 indicate that segregation flux is highest in the convective-front region. This result is strongly tied to the shear-rate distribution shown in Fig. 4.4 for the monodisperse case, since $f_{sl} \sim \dot{\gamma}$. The high values of f_{sl} at the front are still smaller compared to the w values at the transition between flow regions, presented in Fig. 4.2 ($w \approx 4 \text{ cm s}^{-1}$). Nonetheless, w values at the front are of the same order of magnitude or close to those of f_{sl} , an indication that segregation could influence general flow dynamics, a result also evident in particle distribution and large particle recirculation (Fig. 4.5).

Large particle recirculation is observed in all the experiments, shown via normalized velocities, $\bar{u}_j/\max_{\forall x,z} \bar{u}$ and $\bar{w}/\max_{\forall x,z} \bar{w}$, in the form of white arrows (see Fig. 4.5). For $R > 2$, dilation

has been found to be related to more efficient, hence faster segregation (Trehwela et al., 2020b), resulting in large particles recirculating at the front of the flow. Our results for $d^s = 6$ mm, i.e., $R = 2.33$, show that large particles are likely to be constrained to the dilated-front, seen in Fig. 4.5 (a)-(d). For the experiments with $R = 1.66$ in Fig. 4.5 (e)-(h), we observed a less marked segregated state at the front, with lower large particle concentration a sign that large particles were more homogeneously distributed.

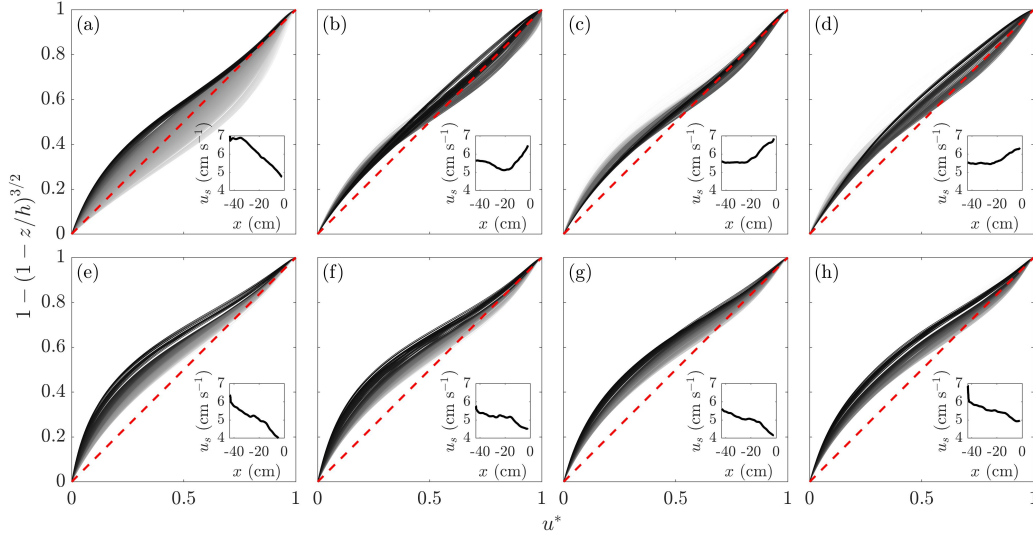


Figure 4.7 – Normalized velocity profiles u^* (see Eq. 4.21) for 6 mm (a)-(d) and 8 mm (e)-(h) bidisperse experiments at different Φ^s . From Tab. 4.2, Exps. 2 through 5 correspond to subplots (a) through (d), and Exps. 7 through 10 correspond to subplots (e) through (h). The profiles are plotted in grayscale from white to black, from the left- to the right-end of the captured flow region. In each plot, an identity line is plotted (dashed red line). All subplots have an inset plot, where the u_s progression in the longitudinal direction of the flow is plotted.

Breaking size segregation waves were observed in all bidisperse experiments. We can infer from Fig. 4.5 the breaking size segregation wave structure, similar to that observed by van der Vaart et al. (2018a). Large particles at the surface and right-end of the flow, fell onto the very front of the avalanche where they are overran by the flow and dragged back into the bulk. Eventually, these large particles segregated and rose back to the surface onto the front. The lens region (Gray and Ancy, 2009; Johnson et al., 2012; van der Vaart et al., 2018a), where large and small particles were interchanged by the action of shear-induced segregation, is seen in the middle part of the avalanche, between $-40 < x < -10$ cm for all cases. Concentration gradients in this region indicate an apparent mixing, where large particles rise and small particles percolate as a result of segregation. Our results also show that changes in the overall particle concentration between different experiments induced variations in the characteristics of the breaking size segregation waves. As we increased the overall large particle concentration, the layer of large particles at the front became thicker and the lens region extended to the left of the flow, disrupting the layered region described in §4.6.1.

Normalized velocity profiles u^* are shown in Fig. 4.7. These profiles are defined as

$$u^* = \frac{\bar{u} - u_0}{u_h - u_0}, \quad (4.21)$$

where u_0 is the basal particle velocity at $z = 0$. This time, the profiles are normalized to the vertical velocity difference $u_h - u_0$. This normalization is different than the one used in Fig. 4.3, where we used u_b instead of u_0 to highlight slip influence close to the belt. Despite this difference in the normalization, the results shown in Fig. 4.7 follow the trend observed in the monodisperse experiments. Slip is still substantial, with values that change along the flow direction and that range from 40 to 80% of u_b (see Fig. 4.7 insets). From Fig. 4.7 insets, we infer that large particle concentration regularizes slip by reducing its longitudinal gradient. Surprisingly, the experiments with $d^s = 6$ mm show an inversion of the u_s profile when Φ^l is incremented, a higher u_s was measured at the front of the flow for $\Phi^l > 10\%$ experiments. This result is not consistent with $d^s = 8$ mm, which suggests that bed roughness has an important role in shear transmission and should be considered for scalings.

A ratifying result is presented in Fig. 4.7, u^* scales to $h^{3/2}$, an indication of a Bagnold-like velocity profile (Eq. 4.9) (Bagnold, 1954; Mitarai and Nakanishi, 2005). Even if this result could have been expected, we found that profiles were consistent through the longitudinal direction independent of flow height. Basal-slip tends to deviate the profiles, particularly close to the belt, but far from the bottom the profiles are in agreement with the Bagnold-scaling. Average particle concentration influences the results in terms of consistency, as discussed, when Φ^l was increased the slip throughout the base becomes less variable and the velocity profiles aligned better to $1 - (1 - z/h)^{3/2}$.

4.7 Conclusions

We presented an enclosed conveyor-belt setup to study stationary granular avalanches. A set of ten mono- and bidisperse experiments were carried out in the aforementioned conveyor-belt setup. All the experiments exhibited a quasi-stationary behavior characterized by a convective-front, at the right-end of the inclined flume, and a particle-layered region towards the flume's left-end. Our experimental results presented relevant granular flow characteristics and structures, already discussed in the literature, such as: blunt fronts (Denissen et al., 2019), breaking-size-segregation waves (Thornton and Gray, 2008; Gray and Ancy, 2009; Johnson et al., 2012; van der Vaart et al., 2018a) and crystallization (Tsai and Gollub, 2004). Their simultaneous appearance in our experiments entices to study their interplay and coupling. Future studies could be supported by the fact that in our experiments, and despite of partial particle concentration ϕ^v and size-ratio R , time-averaged velocity profiles scaled to $h^{3/2}$. This scaling is an indication of the Bagnold scaling, a characteristic of granular flows down an incline (Silbert et al., 2001; Mitarai and Nakanishi, 2005), and could allow the usage of the $\mu(I)$ rheology to model our experiment dynamics (e.g., Jop et al., 2005). In that direction,

the consistency of the velocity profiles suggests that an equivalent diameter, dependent on d^v and ϕ^v can be established to characterize the flow, as detailed in Eq. 4.15 (Tripathi and Khakhar, 2011). Finally, this velocity scaling found in our experiments could serve as input for a size segregation and granular avalanche coupled model as suggested by Gray and Ancey (2009). We pointed in that direction with the calculation of the segregation flux f_{sl} using the recent scaling of Trewthell et al. (2020a). We found that f_{sl} was high at the dilated-front region, which was in agreement with the observed large particle recirculation and the appearance of a breaking size segregation wave structure within the bulk. Further theoretical analysis must be done to better understand how recent findings on particle-size segregation can explain the observed phenomena.

Various velocity and slope conditions should be explored to identify similarities and differences with the presented results. The influence of the belt's roughness and the vertical boundaries, created by the upper rollers, could be addressed but to eliminate their influence on the flow is impractical for the moment and out of this article's scope. We think that further work in that direction would not change the significance of the presented experiments. Nonetheless, this conveyor belt experimental setup has proven to be useful to visualize and study the internal dynamics of granular flows.

Supplementary information: Setup-related difficulties

Plastic-fluid interactions

An important goal of this setup was to minimize, as much as possible, the fluid volume and the exposure to harmful flammable vapors, hence the enclosed flume was devised. To achieve this goal, the flume required proficient sealing to avoid leaks and spillage, which with flammable fluids can be potentially dangerous. Although this goal seemed trivial, the usage of non-conventional fluids created interactions with the setup's components. Sealing had to be done with plastics, but many of them chemically reacted when exposed to the ethanol and benzyl-alcohol mixture. For example, acrylics like PMMA were rapidly dissolved and most rubbers lost some of their elastic properties, fundamental for sealing, within a couple of hours or days of exposure to the fluid.

Amid plastics, the already mentioned POM and polyvinyl chloride (PVC) resisted well the long exposure to the fluid. We observed no important changes in their material properties. However, and in general, these plastics are slightly porous and tend to absorb small amounts of fluid when submersed for a long time. Even if absorption was very small, we noticed that after long usage, friction between the belt and the sides increased to a point where it jammed the motor. Not only friction was incremented, the compression between the POM pieces was notably higher, which created desynchronization between pieces and wheel. To determine how large was the fluid absorption, we measured length changes in two identical pieces of differing materials.

Figure 4.8 shows measurements of two submersed pieces: one made of POM and the other of PVC. The measurements were made at different fluid-exposure times, reaching 600 hours of submergence. To quantify the expansion, a relative dilation was calculated as

$$\text{Relative dilation (\%)} = \frac{|L^i - L_0^i|}{L_0^i}, \quad (4.22)$$

where $L^i(t)$ is the measured dimension in mm ($i = 1, 2, 3$ for length, width or height, respectively) and L_0^i is the initially measured dimension in mm. We observed that the POM piece swelled much more, and steadily, than its PVC counterpart. This swelling was sufficient to explain the problems created to the experimental setup. An expansion of $\sim 1\%$ in depth or length, may seem harmless, but such expansion in all 300 pieces was equivalent to add three extra pieces to the system. More than one extra piece was enough to desynchronize the dented wheel, which ended up blocked by the bolts arriving on top of its teeth. Regarding side-friction, it was consistently incremented by the extra compression, as a result of pieces expansion in an already compressed belt system. As observed after long experiments, such friction was large enough to gradually bring the motor to a halt.

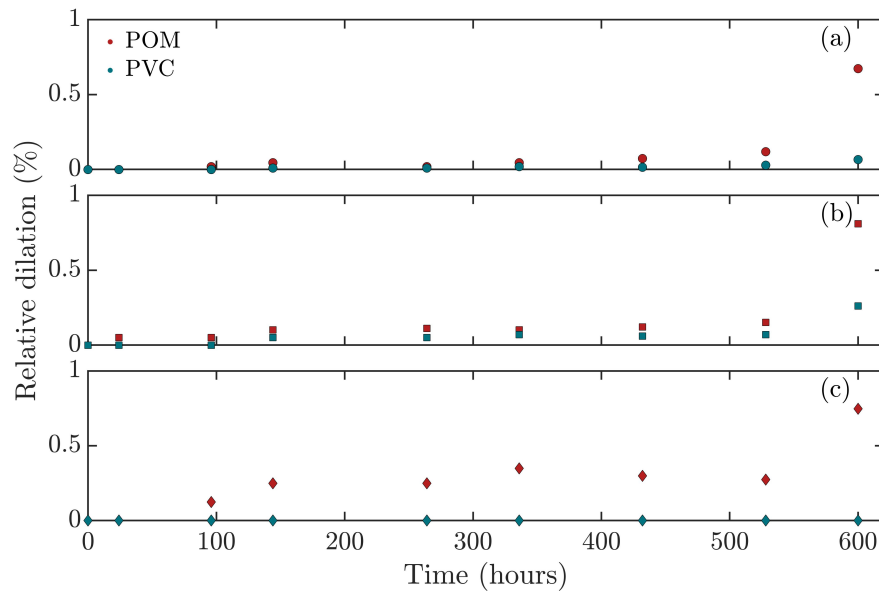


Figure 4.8 – Measurements of relative dilation at different fluid-exposure times for identical POM (red) and PVC (turquoise) belt pieces. Dimensions L^i corresponds to $i := 1$ for length, (a); 2 for width, (b); and 3 for height, (c). There were no stresses applied to the pieces.

In general, PVC expansion was less than half of the POM expansion. This difference, with such serious consequences, prompted a change of the pieces' material to PVC. This change is not reflected in our results, since the whole experimental set for this article was carried out with the POM pieces. Another feature of the used PVC is that it is more opaque than POM. Its opaqueness reduced laser reflection close to the belt, hence improving image definition

during acquisition.

Rubbers and silicones were required to seal joints and screwed pieces that needed to be routinely retired between experiments. When exposed to the RIM fluid, normal rubber rapidly loses elasticity and after long exposure it is partially dissolved. This dissolution bifolds into leakage and fluid pollution, both prejudicial in terms of safety and costs. We essayed many different types of rubbers and silicones with little to no success. To our knowledge, only Viton, a fluoroelastomer, is adequate for o-rings or other rubber pieces. To seal the setup, common silicone could not retain the fluid and was rapidly dissolved. The silicone LOCTITE SI 5910 proved to sustain the fluid exposure effectively for long periods without leakage.

Pollutants and filtering system

The conveyed pieces inevitably produces friction between them, the grooves and the rollers. Most of the friction is against aluminium and the scraping releases a very fine black dust that scatters around. Long running experiments are able to accumulate enough dust to visibly detriment the transparency of the fluid, the laser is then obstructed and images loose quality. To regain image definition and increase light intensity, we changed acquisition parameters such as the gain, and/or reduced the lens' focal ratio. Yet, the black dust would still increase to a point where these improvements became futile.

A filtering system was devised to remove the dust from the fluid. We could have used a wet sieving/filtering system, such as an available Retsch AS200, but we did not know the whole composition of this system, and to not compromise it due to the fluid exposure, we decided to try a simpler setup. A large reservoir would drip the fluid into a funnel with filtering paper of 40 μm . We were able to filter the fluid in approximately one day, which was a reasonable amount of time to prepare the next experiment. With twice the amount of fluid, we could rotate the fluid batches and maintain a controlled amount of dust that did not harm image quality. The reduction of dust production, via improvements like stainless steel grooves, could certainly enhance the setup performance and image quality but were not devised for this work.

5 Conclusions and outlook

5.1 Summary of this thesis

In this thesis, I shed light on the coupling of flow rheology and grain sorting in dense granular flows. I studied this connection through experiments in three different facilities: (i) a two-dimensional shear cell (Chap. 2), (ii) a three-dimensional shear box (Chap. 3), and (iii) an inclined conveyor belt (Chap. 4). Each setup gave me insights on how the particles' size ratio, dilation, shear rate, local concentrations and velocity profiles affected size segregation, and vice versa. These variables and parameters were studied with the help of Refractive Index Matching (RIM), Particle Tracking Velocimetry (PTV) and Coarse-Graining (CG) techniques, which allowed me to visualize and determine the particles' local concentrations and velocity fields. The experimental facilities, techniques and methods used for this dissertation proved to be reliable, robust and well-suited for my objectives.

In Chap. 2, we gave insights about the role of size ratio, defined in that chapter as the ratio between the small particles' and the large particle's diameters d^s/d^l , and the strain rate on large particles segregation. The Hele-Shaw configuration of the two-dimensional shear cell facilitated a direct observation of the squeeze expulsion mechanism acting on a large intruder (as introduced in §1.3 and referenced to Savage and Lun, 1988). Besides the intruder's vertical movement, its rotation Ω_i was measured and found to be dominant factor leading to segregation when the intruder was slightly larger than the surrounding particles. This finding was made through the calculation of conditional probabilities, i.e., the probability that the intruder segregated given that it rotated $P(w_i|\Omega_i)$. In parallel, the time-averaged strain-rate tensor's invariants around the intruder varied from one intruder size to another, but for the same surrounding medium. While dilation I_D was markedly high for an intruder with a large size difference, shear rate II_D was low. Contrarily, for an intruder with a small size difference, dilation I_D was low and shear rate II_D was high. These results backed up the initial direct observations made and suggested that the squeeze expulsion micromechanical origin must be dependent on the size ratio. Two submechanisms were proposed: (i) a dilation-, and (ii) a rotation-based mechanism for size ratio values (i) larger, and (ii) smaller than $d^s/d^l = 0.5$.

Chapter 5. Conclusions and outlook

A functional form for the segregation flux function f_{sl} was obtained from simple shear experiments in an oscillatory three-dimensional shear box. We carried out four experimental sets that consisted in an opaque borosilicate glass intruder segregating through a RIM bulk made of transparent beads of the same glass. These sets were defined by various shear rates $\dot{\gamma}$ and size ratios $R = d^l/d^s$ conditions for two segregation cases: (i) a large intruder being squeezed by smaller particles towards the surface, and (ii) a small intruder percolating through a matrix of larger particles towards the bottom. Four key experimental observations were made to determine the functional form of f_{sl} :

- i all intruders showed curved trajectories and were well-fitted by a quadratic law,
- ii the segregation rate scaled linearly with $\dot{\gamma}$ for both large and small intruders,
- iii the segregation rate for large intruders scaled linearly with $R - 1$,
- iv the segregation rate for small intruders is affected by spontaneous percolation when R becomes larger than 1.5, therefore it initially scaled linearly but tended to be a quadratic function of $R - 1$.

The efforts to collapse all small and large segregation rates gave us a final key observation: the size ratio R was enough to explain the segregation asymmetry in our experiments, via a concentration-averaged diameter $\bar{d} = d^s\phi^s + d^l\phi^l$. We used dimensional analysis to determine that the small particle segregation flux can be expressed, unifying the definitions made in Chaps. 1 and 3, as

$$F^s = f_{sl}\phi^s\phi^l = \frac{\mathcal{B}\rho_*\dot{\gamma}\bar{d}^2}{\mathcal{C}\rho_*g\bar{d} + p} \left[(R - 1) + \mathcal{E}\phi^l(R - 1)^2 \right] \phi^s\phi^l, \quad (5.1)$$

whose coefficients $\mathcal{B} = 0.3744$, $\mathcal{C} = 0.2712$ and $\mathcal{E} = 2.0957$ were determined with our experimental results.

Our functional form was used to successfully reproduce the results of van der Vaart et al. (2015) for intermediate concentrations, which proves the scaling validity under other experimental conditions. The proposed function is versatile enough to provide a physical parametrization of particle-size segregation in terms of flow variables and parameters, while still capturing the segregation asymmetry and previously-made formulations (i.e., the functions of: Bridgwater et al., 1985; Dolgunin and Ukolov, 1995; Gajjar and Gray, 2014).

To study granular avalanches in steady and uniform conditions, I carried out RIM experiments in an enclosed and inclined conveyor belt. To relate flow and bulk variables, I used particle tracking velocimetry and coarse-graining to calculate the velocity and concentration fields of mono and bidisperse experiments. These experiments were differentiated by their general small particle concentration $\Phi^s = 1 - \Phi^l$ and small particle diameter d^s , hence their size ratio R . Nonetheless, all the experiments were quasi-stationary and exhibited two clear regions:

- i a convective-bulged front, characterized by high dilation and high shear rate that confined large particles within the region,
- ii a layered tail, composed mostly of well-arranged layers of small particles that moved on top of each other.

A transition between these regions was also observed: they were found to have a similar structure than that of a breaking size segregation wave (Thornton and Gray, 2008; Johnson et al., 2012; van der Vaart et al., 2018a).

In general, and despite the fact that the steady flows showed variable local species concentrations, their time-averaged velocity profiles were found to be Bagnold-like, i.e., $u \sim h^{3/2}$. This scaling is a characteristic of monodisperse dense granular flows over inclined surfaces that has been associated to the $\mu(I)$ rheology (Silbert et al., 2001; MiDi, 2004; Mitarai and Nakanishi, 2005). Finally, in Chap. 4, we were able to use the segregation flux scaling of Chap. 3 in a different flow configuration. The functional dependence on $\dot{\gamma}$, ϕ^s and p , through a hydrostatic pressure distribution, allowed the segregation flux direct calculation from the analyzed particles' images. f_{sl} experimental results confirmed other remarks made on large particle recirculation and the relation between high-dilation and high-segregation rate (raised in Chap. 2).

5.2 Future perspectives

5.2.1 Outcomes

At a microscopic scale, I studied the size ratio and local strain-rate roles on large particle segregation. These findings could provide a better understanding at the contact level and could be useful for discrete numerical models of size segregation processes. A tangent outcome of the strain-rate influence on large particle segregation is the friction role for small size differences. In this case, frictionless large particles will struggle to segregate, since their segregation mechanism relies more on a friction-induced rotation (Jing et al., 2017). This point may have an application on mixing processes whose goal is to restrain segregation and achieve homogeneous mixtures.

We developed a segregation scaling that has a wide range of applications for segregation processes in nature and the industry. Even if the formulation is not complete, our proposed functional form determined a clear dependence on a variety of physical variables that were known to play a role but with no well-defined scales. This functional form also depends on macroscopic variables or distributions that can be easily determined or set externally, a fact that could be directly translated to industrial applications or natural flows. For instance, in a gravity-driven debris flow, pressure and shear-rate distribution are usually assumed to have well-known distributions, that are direct functional inputs to f_{sl} .

A conveyor belt facility was constructed and although it is undergoing modifications, it is operational and could serve for further experimentation. Already a substantial amount of experimental data was obtained and is also available for further use. This data can be used for model validation and for the development of segregation-coupled flow models. Specifically, the fact that the measured experimental velocity profiles were Bagnold-like promotes the idea that a concentration-averaged diameter \bar{d} could be used to determine a bidisperse inertial number.

5.2.2 Open challenges

Even if in this dissertation I provided relevant research on size segregation, there are plenty of topics and challenges that are open for further developments. Here, I detail some propositions that could be worth studying in the short- and long-term.

For shear cell experiments

As probably noted by the reader, the developments I made for the two-dimensional cell were barely related to the segregation flux scaling proposed in Chap. 3. An analysis of the two-dimensional intruders' data could be done to validate the proposed scaling in this shear cell configuration. For that purpose, three considerations must be taken into account: (i) the appearance of artifacts due to the restrictive flow configuration, (ii) the bulk had no interstitial fluid, and (iii) the particles' material properties. These three aspects could affect the values of \mathcal{B} , \mathcal{C} and \mathcal{E} , but they should not affect the key experimental observations in Chap. 3.

I did not present any theoretical developments or models on the squeeze expulsion mechanism. Recently, buoyancy-analog scalings have gained relevance in the literature (Guillard et al., 2016; van der Vaart et al., 2018b; Jing et al., 2020), however, there is not much experimental data that sustains these scalings. Perhaps, a brief validation of these scalings could be done with the available data presented in this dissertation.

To continue on the topic of large particle segregation, in this thesis I did not explore huge size ratio values and their effect on size segregation. Reverse or restrained segregation has been observed mostly in discrete elements method simulations (Thomas, 2000; Thomas and D'Ortona, 2018; Jing et al., 2020). Besides the fact that my experiments did not show a decrease in the segregation rates for very large size ratios, it seems simple to extend my experimental results to a wider range of size ratios.

An intriguing, yet irrelevant result for the main body of this thesis, was found in the initial experiments in the three-dimensional shear box. When I used a RIM mixture of acrylic beads and Triton X-100, no particle-size segregation was observed for large intruders. In Appx. A.2, I hypothesize that a combined effect of viscosity and buoyancy restrained segregation, which could be a result of lubrication and the loss of friction. In that direction, experiments exploring the role of the interstitial fluid on particle-size segregation could provide more functional

dependencies to the scaling presented in this thesis.

For other experimental configurations

The conveyor belt setup creates a very particular flow condition, a steady-uniform flow. Experiments carried out under these flow conditions could motivate and validate a coupled model that considers the mass and momentum conservation equations for the bulk, and the convective-diffusive segregation equation with the proposed flux function. This proposition could follow and extend the work of Gray and Ancey (2009). Conveniently to our experimental flow condition, Gray and Ancey (2009) provided a traveling-wave solution that could now include a generally-defined bidisperse inertial number I fed back by species redistribution due to particle-size segregation. This feedback is given by the functional dependence of f_{sl} which reciprocally depends implicitly on the inertial number I .

The experiments made in the conveyor belt also showed an interesting phenomenon: a stationary granular hydraulic jump or bore (Savage, 1979; Boudet et al., 2007; Johnson and Gray, 2011; Edwards and Vriend, 2016), for experiments with a slope $\theta > 16^\circ$. The conveyor belt's configuration eases the jump visualization and analysis, which could elucidate its role on segregation and motivate further theoretical developments.

Although it was not used for this thesis, we designed and developed an annular shear cell that recently became operational. An explanation on the design and construction of this setup is presented in Appx. B. RIM experiments in this annular shear cell could provide further validation of the presented segregation scaling. In this setup, an upper pressure condition can be imposed simultaneously to the flow, which has the particularity that the imposed shear rate is continuous rather than oscillatory. For instance, a pressure-imposed flow condition could provide better data to calibrate the \mathcal{C} constant, which sets a condition for the segregation rate close to the surface in Eq. 5.1.

A Notes on experiments with restrained particle-size segregation

A.1 Absence of the kinetic sieving mechanism in two-dimensional experiments

In Chapter 2, I presented experiments that consisted in a large particle squeezed upwards through a matrix of smaller particles. As mentioned in §2.3.1 I did not show results about small particles' segregation through a matrix of larger particles. In this section I elaborate on the reasons why this may have happened and the consequences on similar two-dimensional studies.

In a two-dimensional flow configuration, particles are basically disks that move in the plane. In a dense particle flow configuration, disks are necessarily sustained by contacts with neighbors or boundaries. Close contacts in a two-dimensional configuration are inherently different than those in a three-dimensional configuration. In a tridimensional configuration a particle can be supported by particles below that are slightly at the front or the back in the transverse direction of the volume. This transverse offset creates additional gap possibilities for a small particle to fall that are non-existent in a two-dimensional configuration. For a small disk to percolate through two larger disks, separation must be created, hence for a moment the support must shift from one neighbor to another. Percolation does not depend on existent gaps but on the creation of them, which is more similar to the *squeeze expulsion* mechanism rather than the *kinetic sieving*.

This artifact, particular for two-dimensional flow configurations, could present difficulties when analyzing size segregation. First, the asymmetric behavior detailed by van der Vaart et al.'s (2015) and further developed in chapter 3 may not be evidenced. Despite the experiments in the 2D shear cell are under dry conditions, for which we should expect a higher value for \mathcal{B} , we also expect the parameter \mathcal{E} to decrease or be null, since its appearance was purely related to the case of a small intruder with $R > 2$ segregating through a matrix of large particles. Second, this absence of kinetic sieving may only be observed for extreme concentration cases where $\phi^s = 0^+$ and could be less relevant for higher concentrations.

Appendix A. Notes on experiments with restrained particle-size segregation

Material	n_r	ρ (g cm ⁻³)	η (cP)	Supplier
PMMA	1.4912	1.18	NA	The Plastic Ball Company
Triton X-100	1.492	1.07	270	Fisher Scientific

Table A.1 – Refractive indexes n_r , densities ρ , viscosities η and suppliers for the PMMA - Triton X-100 experiments.

Further research should be made in this matter to determine how valid is the extrapolation of two-dimensional results to tridimensional ones. In addition this note could be important for sorting or mixing processes that are transversally restrained, such as cigarette making or coin sorting processes, for example.

A.2 Poly(methyl methacrylate) (PMMA) - Triton X-100 experiments

Initially, the experiments on the three dimensional shear box that served for Chapter 3 of this dissertation were envisioned with a different RIM mixture. I saw many difficulties associated to the ethanol and benzyl-alcohol mixture that did not exist with another available fluid: Triton X-100. This fluid is not flammable and since its refractive index was very close to that of Poly(methyl methacrylate) (PMMA), no index adjustment was required. In Table A.2 I present the properties of PMMA and Triton X-100 for the RIM experiments in the three dimensional shear box.

Under dry-conditions, an opaque PMMA intruder of $d_i = 11.1$ mm was able to segregate to the top of a $d_m = 4.8$ mm bulk after an approximate of 10 minutes. In such conditions, I was unable to measure its position, so a refractive index matched fluid was fundamental to visualize the intruder and measure segregation.

d_i (mm)	d_m (mm)	$R = d^l / d^s$	$\dot{\gamma}_m$ (s ⁻¹)	fps
6.4	11.1	1.75	0.26	40
4.8	11.1	2.33	0.26	40
3.2	11.1	3.25	0.26	40
11.1	4.8	2.33	0.26	40

Table A.2 – Experimental parameters for PMMA - Triton X-100 experiments. Intruder d_i and media d_m diameters, size ratios R , external shear rates $\dot{\gamma}_m$ and image acquisition frame rate per second (fps).

Unexpectedly, with Triton X-100 as the interstitial fluid, the intruder could not rise to the top. I recorded images for more than an hour without substantial vertical movement of the intruder. Intra-cycle vertical movement was observed but it was just the result of the periodic cell movement, as expected. Inter-layer movement was not observed. Despite this result, I

completed the experimental set (Tab. A.2), whose remaining experiments were for a small intruder segregating through a matrix of large particles. Segregation was observed but only for large size ratios, $R = d^l/d^s > 2$. For experiments with a size ratio $R < 3$, partial- to null-segregation was observed. In Figure A.1 I show that as the size ratio was decreased, segregation became restrained. The intruder segregated completely to the bottom of the cell only for $R = 3.5$, for $R = 2.3$ segregation was partial and the larger intruder did not segregate at all, $R = 1.8$ in Fig. A.1.

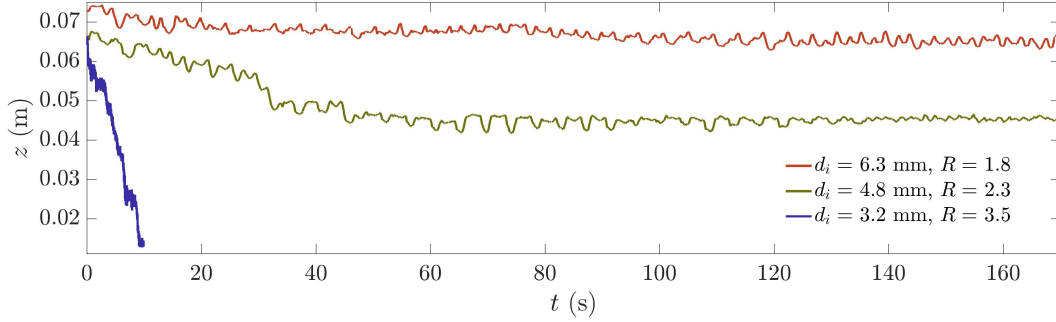


Figure A.1 – Vertical positions of small intruders of diameter $d_i = \{3.2, 4.8, 6.3\}$ mm segregating through large particles of diameter $d_m = 11.1$ mm. For these experiments, the granular material was formed by an opaque PMMA intruder immersed in a bath of transparent PMMA beads and Triton X-100.

Based on the opposite results obtained for the experiments under dry and wet conditions, I hypothesized on the role of the interstitial fluid. The surrounding fluid may introduce two effects that restrain the segregation process: (i) viscous and (ii) buoyant.

Viscosity lubricates frictional contacts and as I presented in this dissertation, grain-grain friction is needed for the segregation of large particles (Chap. 2). One hypothesis is that Triton X-100, with its high viscosity, lubricated the frictional contacts existent under dry-conditions. With no strong friction between grains, it was impossible for the small particles to squeeze up the large intruder.

The densities of PMMA and Triton X-100 are quite similar. In fact, these materials have been used with other fluids for density- and refractive index-matched experiments (Wiederseiner et al., 2011a; Andreini et al., 2013). Just a single particle immersed in Triton X-100 by itself showed a weak negative buoyancy, sedimenting slowly to the bottom of the container. In the small intruder experiments, the particle sedimentation was now inevitably obstructed by the larger particles. When the size ratio was large, the particle could still percolate through the matrix, but for size ratios closer to 1, the small intruder is subjected to the contact network. Then, its segregation depends on the grain frictional contacts, which I said, were weak.

These observations give the viscous effects the initial upperhand to explain why segregation was restrained in these experiments. Nonetheless, this is just an initial guess, far from definitive.

Appendix A. Notes on experiments with restrained particle-size segregation

Further experiments could be made to shed light on the effect of gravity-reduced environments and high-viscosity fluids on particle-size segregation.

B Annular shear cell setup

B.1 Conception

Annular shear cells are commonly used to study granular flows (Carr and Walker, 1968; Stephens and Bridgwater, 1978a; Savage and Sayed, 1984; Jasti and Higgs III, 2008; Koval et al., 2009; Golick and Daniels, 2009; Guo and Campbell, 2016). These cells create a flow condition that is quite appealing to study granular flows. Due to the cell radial symmetry and under a constant shear rate, the flow is uniform and steady. However, this geometry may present some disadvantages: (i) shear-banding and depth-dependent velocity decay (Tsai and Gollub, 2005), and (ii) secondary-radial currents for high curvatures (Savage and Sayed, 1984).

Together with Prof. Christophe Ancey, we conceived the construction of an annular shear cell to be used in my thesis. The initial design was based on previous studies that used this geometry to study dense granular flows (in particular the shear cells of Tsai and Gollub, 2005; May et al., 2010b; Boyer et al., 2011). We considered most of this setup's associated advantages and difficulties, and adapted them to the fact that the setup had to be used for RIM experiments. Therefore, the setup was envisioned to be a traditional cell, where the shear would be imposed by an upper annular plate, as done by the cell of Tsai and Gollub (2005).

Another appealing feature of annular shear cells is the possibility to apply normal stresses by pressing down with the upper annular plate, as shown by Boyer et al. (2011). Experiments at different confining pressures could explore on the role of pressure in particle-size segregation, therefore we defined that the upper annular plate would fulfill that role. With the upper-boundary functionality well-defined, the lower boundary needed to ease the RIM technique application. A large glass pane could serve as the cell's bottom boundary and at the same time, could allow the passage of a laser sheet or the image acquisition of the whole cell's bottom. Finally, and due to our interest to study particle-size segregation on this cell, windows needed to be placed at the sides of the cell. A full-depth window allows the determination of segregation fluxes and concentrations using the Refractive Index Matching Scanning technique, already used for the experiments of van der Vaart et al. (2015).

B.2 Construction

The construction of the annular shear cell was carried out by the ENAC Technical Platform, under the supervision of Mr. Michel Teuscher, Mr. Bob de Graffenried, Prof. Christophe Ancey and myself. A diagram of the constructed annular shear cell is presented in Figure B.1.

The constructed annular shear cell consists in two separate poly-vinyl chloride (PVC) pieces that are firmly screwed on top of a 60 cm large, 60 cm width and 2 cm thick glass pane. The central PVC piece is a cylinder of $R_i = 15$ cm radius and $H_s = 15$ cm height. The external PVC piece is a large block with a cylindrical space within of $R_e = 25$ cm radius and H_s height as well. Both pieces create a cross-section of 150 cm^2 and a volume of 28745.64 cc (cubic centimeters).

As conceived, the shear is exerted by the rotation of an upper annular plate. This rotation is controlled by a Beckhoff servomotor¹ which has a gear-box that sets the rotational speed to a range of 0-100 rpm. The upper annular plate's vertical position is set by a 500-mm-step Zaber linear stage².

Three lateral acrylic-PVC windows were framed at the front and sides of the annular shear cell (see Fig. B.1(a) dashed-dot green line). Due to the fact that the RIM fluid dissolves acrylic components, the windows were built with two pieces: (i) an exterior acrylic piece attached to a (ii) curved interior piece made of semi transparent PVC. This window design maximized transparency without exposing the acrylic to the RIM fluid.

¹Model: Beckhoff AM8131-0F02-0000

²Model: Zaber X-LRT0500BL-E08C-KX14N

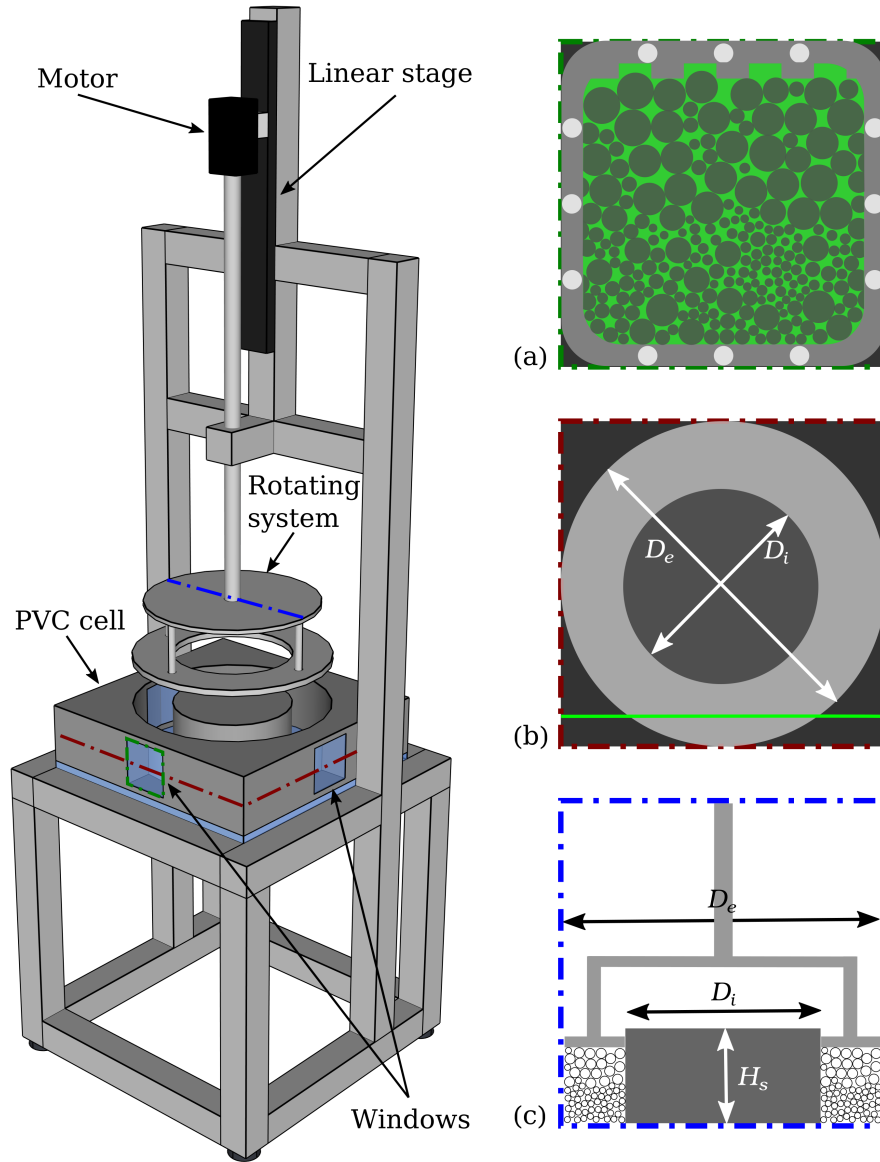


Figure B.1 – Diagram of the annular shear cell setup (rheometer). The setup is composed by two separate pieces that form the annular cell (PVC cell in the diagram): a cylinder of $D_i = 30$ cm diameter, and a PVC block with an inner cylindrical basin of $D_e = 50$ cm diameter. The height of both pieces is $H_s = 15$ cm and they are on top of an horizontal glass pane through which the grains can be observed or illuminated via lasers. Three lateral windows are placed at each side of the PVC cell to visualize the flow within the cell. An idealized flow visualization is shown in (a) (green dashed-dot cutline), where a refractive index matched granular material is observed as black circles due to laser induced fluorescence. The windows were devised so that their lower boundaries correspond precisely to the bottom of the cell. In (b) (red dashed-dot cutline), a top view of the annular shear cell is shown, with a green line representing a laser passing perpendicularly through the cell. Finally, a cross-section of the entire annular cell is presented in (c) (blue dashed-dot cutline). In this last view, we see the rotating system which is placed vertically by a linear stage and rotated by a motor.

Bibliography

- (2019). *Matlab (R2019a)*. The Mathworks Inc., Natick, Massachusetts.
- Adrian, R. J. (1991). Particle-imaging techniques for experimental fluid mechanics. *Annual review of fluid mechanics*, 23(1):261–304.
- Álvarez-Valero, A. M., Sáez, R., Pérez-López, R., Delgado, J., and Nieto, J. M. (2009). Evaluation of heavy metal bio-availability from almagrera pyrite-rich tailings dam (iberian pyrite belt, sw spain) based on a sequential extraction procedure. *Journal of Geochemical Exploration*, 102(2):87–94.
- Ancey, C. (2007). Plasticity and geophysical flow: A review. *Journal of Non-Newtonian Fluid Mechanics*, 142:4–35.
- Ancey, C., Coussot, P., and Evesque, P. (1999). A theoretical framework for granular suspensions in a steady simple shear flow. *Journal of Rheology*, 43(6):1673–1699.
- Ancey, C. and Evesque, P. (2000). Frictional-collisional regime for granular suspension flows down an inclined channel. *Physical Review E*, 62(6):8349.
- Andreini, N., Ancey, C., and Epely-Chauvin, G. (2013). Granular suspension avalanches. ii. plastic regime. *Physics of Fluids*, 25(3):033302.
- Andreotti, B., Forterre, Y., and Pouliquen, O. (2013). *Granular media: between fluid and solid*. Cambridge University Press.
- Armanini, A., Capart, H., Fraccarollo, L., and Larcher, M. (2005). Rheological stratification in experimental free-surface flows of granular–liquid mixtures. *Journal of Fluid Mechanics*, 532:269–319.
- Atherton, T. J. and Kerbyson, D. J. (1999). Size invariant circle detection. *Image and Vision computing*, 17(11):795–803.
- Azanza, E., Chevoir, F., and Moucheron, P. (1999). Experimental study of collisional granular flows down an inclined plane. *Journal of Fluid Mechanics*, 400:199–227.
- Baek, S. and Lee, S. (1996). A new two-frame particle tracking algorithm using match probability. *Experiments in Fluids*, 22(1):23–32.

Bibliography

- Bagnold, R. A. (1954). Experiments on a gravity-free dispersion of large solid spheres in a newtonian fluid under shear. In *Proceedings of the Royal Society of London A: Mathematical, Physical and Engineering Sciences*, volume 225, pages 49–63. The Royal Society.
- Bai, K. and Katz, J. (2014). On the refractive index of sodium iodide solutions for index matching in piv. *Experiments in fluids*, 55(4):1704.
- Baker, J., Johnson, C., and Gray, J. M. N. T. (2016). Segregation-induced finger formation in granular free-surface flows. *Journal of Fluid Mechanics*, 809:168–212.
- Barker, T. and Gray, J. M. N. T. (2017). Partial regularisation of the incompressible $\mu(i)$ -rheology for granular flow. *J. Fluid Mech.*, 828:5–32.
- Barker, T., Schaeffer, D., Bohorquez, P., and Gray, J. M. N. T. (2015). Well-posed and ill-posed behaviour of the-rheology for granular flow. *Journal of Fluid Mechanics*, 779:794–818.
- Bates, L. (1997). *User guide to segregation*. British Materials Handling Board.
- Baxter, J., Tüzün, U., Heyes, D., Hayati, I., and Fredlund, P. (1998). Stratification in poured granular heaps. *Nature*, 391:136.
- Bertho, Y., Giorgiutti-Dauphiné, F., and Hulin, J.-P. (2003). Dynamical janssen effect on granular packing with moving walls. *Physical review letters*, 90(14):144301.
- Berzi, D. (2014). Extended kinetic theory applied to dense, granular, simple shear flows. *Acta Mechanica*, 225(8):2191–2198.
- Berzi, D., Jenkins, J. T., and Richard, P. (2020). Extended kinetic theory for granular flow over and within an inclined erodible bed. *Journal of Fluid Mechanics*, 885:A27.
- Boudet, J., Amarouchene, Y., Bonnier, B., and Kellay, H. (2007). The granular jump. *Journal of Fluid Mechanics*, 572:413–431.
- Boyer, F., Guazzelli, É., and Pouliquen, O. (2011). Unifying suspension and granular rheology. *Physical Review Letters*, 107(18):188301.
- Bridgwater, J. (1976). Fundamental powder mixing mechanisms. *Powder Technology*, 15(2):215–236.
- Bridgwater, J., Foo, W., and Stephens, D. (1985). Particle mixing and segregation in failure zones – theory and experiment. *Powder Technol.*, 41:147.
- Budwig, R. (1994). Refractive index matching methods for liquid flow investigations. *Experiments in fluids*, 17(5):350–355.
- Campbell, C. S. (1990). Rapid granular flows. *Annual Review of Fluid Mechanics*, 22(1):57–90.
- Campbell, C. S. (2006). Granular material flows—an overview. *Powder Technology*, 162(3):208–229.

- Capart, H., Young, D., and Zech, Y. (2002). Voronoï imaging methods for the measurement of granular flows. *Experiments in fluids*, 32(1):121–135.
- Carr, J. and Walker, D. (1968). An annular shear cell for granular materials. *Powder Technology*, 1(6):369–373.
- Chassagne, R., Maurin, R., Chauchat, J., Gray, J. M. N. T., and Frey, P. (2020). Discrete and continuum modelling of grain size segregation during bedload transport. *J. Fluid Mech.*, 895:A30.
- Chen, K. D., Lin, Y. F., and Tu, C. H. (2012). Densities, viscosities, refractive indexes, and surface tensions for mixtures of ethanol, benzyl acetate, and benzyl alcohol. *Journal of Chemical & Engineering Data*, 57(4):1118–1127.
- Chen, R. and Fan, L.-S. (1992). Particle image velocimetry for characterizing the flow structure in three-dimensional gas-liquid-solid fluidized beds. *Chemical Engineering Science*, 47(13-14):3615–3622.
- Chialvo, S. and Sundaresan, S. (2013). A modified kinetic theory for frictional granular flows in dense and dilute regimes. *Physics of Fluids*, 25(7):070603.
- Clément, S. A., Guillemain, A., McCleney, A. B., and Bardet, P. M. (2018). Options for refractive index and viscosity matching to study variable density flows. *Experiments in Fluids*, 59(2):32.
- Coulomb, C.-A. d. (1773). In memories de mathematique et de physique. *Acad. R. Sci. Divers Sans*, 7:343–382.
- Crocker, J. C. and Grier, D. G. (1996). Methods of digital video microscopy for colloidal studies. *Journal of colloid and interface science*, 179(1):298–310.
- Davies, E. R. (2004). *Machine vision: theory, algorithms, practicalities*. Elsevier.
- Davies, T. R. (1990). Debris-flow surges—experimental simulation. *Journal of Hydrology (New Zealand)*, pages 18–46.
- Delannay, R., Valance, A., Mangeney, A., Roche, O., and Richard, P. (2017). Granular and particle-laden flows: from laboratory experiments to field observations. *Journal of Physics D: Applied Physics*, 50(5):053001.
- Denissen, I. F., Weinhart, T., Te Voortwis, A., Luding, S., Gray, J., and Thornton, A. (2019). Bulbous head formation in bidisperse shallow granular flow over an inclined plane. *Journal of Fluid Mechanics*, 866:263–297.
- Dhont, B. and Ancey, C. (2018). Are bedload transport pulses in gravel bed rivers created by bar migration or sediment waves? *Geophysical Research Letters*, 45(11):5501–5508.
- Dijksman, J. A., Rietz, F., Lőrincz, K. A., van Hecke, M., and Losert, W. (2012). Invited article: Refractive index matched scanning of dense granular materials. *Review of Scientific Instruments*, 83(1):011301.

Bibliography

- Dijksman, J. A. and van Hecke, M. (2010). Granular flows in split-bottom geometries. *Soft Matter*, 6(13):2901–2907.
- Ding, Y., Gravish, N., and Goldman, D. I. (2011). Drag induced lift in granular media. *Physical Review Letters*, 106(2):028001.
- Dolgunin, V. and Ukolov, A. (1995). Segregation modeling of particle rapid gravity flow. *Powder Technology*, 83(2):95–103.
- Drescher, A. and De Jong, G. D. J. (1972). Photoelastic verification of a mechanical model for the flow of a granular material. *Journal of the Mechanics and Physics of Solids*, 20(5):337–340.
- Edwards, A. and Vriend, N. (2016). Size segregation in a granular bore. *Physical Review Fluids*, 1(6):064201.
- Elkins, C. J. and Alley, M. T. (2007). Magnetic resonance velocimetry: applications of magnetic resonance imaging in the measurement of fluid motion. *Experiments in Fluids*, 43(6):823–858.
- Fan, Y., Boukerkour, Y., Blanc, T., Umbanhowar, P. B., Ottino, J. M., and Lueptow, R. M. (2012). Stratification, segregation, and mixing of granular materials in quasi-two-dimensional bounded heaps. *Phys. Rev. E*, 86:051305.
- Fan, Y., Schlick, C. P., Umbanhowar, P. B., Ottino, J. M., and Lueptow, R. M. (2014). Modelling size segregation of granular materials: the roles of segregation, advection and diffusion. *Journal of Fluid Mechanics*, 741:252–279.
- Félix, G. and Thomas, N. (2004). Relation between dry granular flow regimes and morphology of deposits: formation of levées in pyroclastic deposits. *Earth and Planetary Science Letters*, 221(1):197 – 213.
- Forterre, Y. and Pouliquen, O. (2008). Flows of dense granular media. *Annu. Rev. Fluid Mech.*, 40:1–24.
- Fry, A. M., Umbanhowar, P. B., Ottino, J. M., and Lueptow, R. M. (2019). Diffusion, mixing, and segregation in confined granular flows. *AIChE Journal*, 65:875–881.
- Furukawa, R., Shiosaka, Y., Kadota, K., Takagaki, K., Noguchi, T., Shimosaka, A., and Shirakawa, Y. (2016). Size-induced segregation during pharmaceutical particle die filling assessed by response surface methodology using discrete element method. *Journal of Drug Delivery Science and Technology*, 35:284–293.
- Gajjar, P. and Gray, J. M. N. T. (2014). Asymmetric flux models for particle-size segregation in granular avalanches. *Journal of Fluid Mechanics*, 757:297–329.
- Gilberg, D. and Steiner, K. (2020). Size segregation in compressible granular shear flows of binary particle systems. *Granular Matter*, 22:45.

- Goddard, J. D. and Lee, J. (2018). Regularization by compressibility of the $\mu(i)$ model of dense granular flow. *Phys. Fluids*, 30:073302.
- Goldhirsch, I. (2003). Rapid granular flows. *Annual review of fluid mechanics*, 35(1):267–293.
- Goldhirsch, I. (2010). Stress, stress asymmetry and couple stress: from discrete particles to continuous fields. *Granular Matter*, 12(3):239–252.
- Golick, L. A. and Daniels, K. E. (2009). Mixing and segregation rates in sheared granular materials. *Physical Review E*, 80(4):042301.
- Gollin, D., Brevis, W., Bowman, E. T., and Shepley, P. (2017). Performance of piv and ptv for granular flow measurements. *Granular Matter*, 19(3):42.
- Gray, J. M. N. T. (2001). Granular flow in partially filled slowly rotating drums. *Journal of Fluid Mechanics*, 441:1–29.
- Gray, J. M. N. T. (2018). Particle segregation in dense granular flows. *Annual Review of Fluid Mechanics*, (0).
- Gray, J. M. N. T. and Ancey, C. (2009). Segregation, recirculation and deposition of coarse particles near two-dimensional avalanche fronts. *Journal of Fluid Mechanics*, 629:387–423.
- Gray, J. M. N. T. and Ancey, C. (2011). Multi-component particle-size segregation in shallow granular avalanches. *Journal of Fluid Mechanics*, 678:535–588.
- Gray, J. M. N. T. and Ancey, C. (2015). Particle-size and-density segregation in granular free-surface flows. *Journal of Fluid Mechanics*, 779:622–668.
- Gray, J. M. N. T. and Chugunov, V. (2006). Particle-size segregation and diffusive remixing in shallow granular avalanches. *Journal of Fluid Mechanics*, 569:365–398.
- Gray, J. M. N. T. and Hutter, K. (1997). Pattern formation in granular avalanches. *Continuum Mech. & Thermodyn.*, 9:341–345.
- Gray, J. M. N. T. and Kokelaar, B. (2010). Large particle segregation, transport and accumulation in granular free-surface flows. *Journal of Fluid Mechanics*, 652:105–137.
- Gray, J. M. N. T., Shearer, M., and Thornton, A. (2006). Time-dependent solutions for particle-size segregation in shallow granular avalanches. In *Proceedings of the Royal Society of London A: Mathematical, Physical and Engineering Sciences*, volume 462, pages 947–972. The Royal Society.
- Gray, J. M. N. T. and Thornton, A. (2005). A theory for particle size segregation in shallow granular free-surface flows. In *Proceedings of the Royal Society of London A: Mathematical, Physical and Engineering Sciences*, volume 461, pages 1447–1473. The Royal Society.
- Gray, J. M. N. T., Wieland, M., and Hutter, K. (1999). Free surface flow of cohesionless granular avalanches over complex basal topography. *Proc. Roy. Soc. A*, 455:1841–1874.

Bibliography

- Guillard, F., Forterre, Y., and Pouliquen, O. (2014). Lift forces in granular media. *Physics of Fluids*, 26(4):043301.
- Guillard, F., Forterre, Y., and Pouliquen, O. (2016). Scaling laws for segregation forces in dense sheared granular flows. *Journal of Fluid Mechanics*, 807.
- Guillard, F., Marks, B., and Einav, I. (2017). Dynamic x-ray radiography reveals particle size and shape orientation fields during granular flow. *Scientific reports*, 7(1):1–11.
- Guo, T. and Campbell, C. S. (2016). An experimental study of the elastic theory for granular flows. *Physics of Fluids*, 28(8):083303.
- Heyman, J., Delannay, R., Tabuteau, H., and Valance, A. (2017). Compressibility regularizes the (i)-rheology for dense granular flows. *Journal of Fluid Mechanics*, 830:553–568.
- Hill, G., Yeung, S., and Koehler, S. A. (2005). Scaling vertical drag forces in granular media. *EPL (Europhysics Letters)*, 72(1):137.
- Hill, K. M. and Fan, Y. (2016). Granular temperature and segregation in dense sheared particulate mixtures. *KONA Powder and Particle Journal*, 33:150–168.
- Hill, K. M., Gioia, G., and Tota, V. V. (2003). Structure and kinematics in dense free-surface granular flow. *Phys. Rev. Lett.*, 91:064302.
- Hill, K. M., Kharkar, D. V., Gilchrist, J. F., McCarthy, J. J., and Ottino, J. M. (1999). Segregation driven organization in chaotic granular flows. *Proc. Natl Acad. Sci. USA*, 96:11701–11706.
- Hill, K. M. and Tan, D. S. (2014). Segregation in dense sheared flows: gravity, temperature gradients, and stress partitioning. *Journal of Fluid Mechanics*, 756:54–88.
- Isner, A. B., Umbanhowar, P. B., Ottino, J. M., and Lueptow, R. M. (2020). Axisymmetric granular flow on a bounded conical heap: Kinematics and size segregation. *Chemical Engineering Science*, 217:115505.
- Iverson, R. M. (1997). The physics of debris flows. *Reviews of geophysics*, 35(3):245–296.
- Iverson, R. M. and Vallance, J. W. (2001). New views of granular mass flows. *Geology*, 29(2):115–118.
- Jaeger, H. M., Nagel, S. R., and Behringer, R. P. (1996). Granular solids, liquids, and gases. *Reviews of modern physics*, 68(4):1259.
- Janssen, H. (1895). Versuche uber getreidedruck in silozellen. *Z. Ver. Dtsch. Ing.*, 39(35):1045–1049.
- Jasti, V. and Higgs III, C. F. (2008). Experimental study of granular flows in a rough annular shear cell. *Physical Review E*, 78(4):041306.

- Jenkins, J. and Richman, M. (1985). Kinetic theory for plane flows of a dense gas of identical, rough, inelastic, circular disks. *The Physics of fluids*, 28(12):3485–3494.
- Jesuthasan, N., Baliga, B. R., and Savage, S. B. (2006). Use of particle tracking velocimetry for measurements of granular flows: review and application. *KONA Powder and Particle Journal*, 24:15–26.
- Jing, L., Kwok, C., and Leung, Y. (2017). Micromechanical origin of particle size segregation. *Physical review letters*, 118(11):118001.
- Jing, L., Ottino, J. M., Lueptow, R. M., and Umbanhowar, P. B. (2020). Rising and sinking intruders in dense granular flows. *Physical Review Research*, 2(2):022069.
- Johanson, J. R. (1978). Particle segregation ... and what to do about it. *Chem. Eng.*, pages 183–188.
- Johnson, C. and Gray, J. (2011). Granular jets and hydraulic jumps on an inclined plane. *Journal of Fluid Mechanics*, 675:87–116.
- Johnson, C., Kokelaar, B., Iverson, R., Logan, M., LaHusen, R., and Gray, J. M. N. T. (2012). Grain-size segregation and levee formation in geophysical mass flows. *Journal of Geophysical Research: Earth Surface*, 117(F1).
- Jones, R. P., Isner, A. B., Xiao, H., Ottino, J. M., Umbanhowar, P. B., and Lueptow, R. M. (2018). Asymmetric concentration dependence of segregation fluxes in granular flows. *Physical Review Fluids*, 3(9):094304.
- Jop, P., Forterre, Y., and Pouliquen, O. (2005). Crucial role of sidewalls in granular surface flows: consequences for the rheology. *Journal of Fluid Mechanics*, 541:167–192.
- Jop, P., Forterre, Y., and Pouliquen, O. (2006). A constitutive law for dense granular flows. *Nature*, 441(7094):727–730.
- Kapoor, B. and Acrivos, A. (1995). Sedimentation and sediment flow in settling tanks with inclined walls. *Journal of Fluid Mechanics*, 290:39–66.
- Khakhar, D. V., Orpe, A. V., and Hajra, S. K. (2003). Segregation of granular materials in rotating cylinders. *Physica A*, 318:129–136.
- Kokelaar, B., Graham, R., Gray, J. M. N. T., and Vallance, J. (2014). Fine-grained linings of leveed channels facilitate runout of granular flows. *Earth and Planetary Science Letters*, 385:172–180.
- Koval, G., Roux, J.-N., Corfdir, A., and Chevoir, F. (2009). Annular shear of cohesionless granular materials: From the inertial to quasistatic regime. *Physical Review E*, 79(2):021306.
- Landau, L. D. and Lifšic, E. M. (1999). *Theory of elasticity*, volume 7. Butterworth-Heinemann, Oxford, 3 edition.

Bibliography

- Leucippus and Democritus (1999). *The atomists: Leucippus and Democritus : fragments : a text and translation with a commentary*, volume 36 of *Phoenix. Supplementary volume*. University of Toronto Press, Toronto.
- Li, J., Baird, G., Lin, Y.-H., Ren, H., and Wu, S.-T. (2005). Refractive-index matching between liquid crystals and photopolymers. *Journal of the Society for Information Display*, 13(12):1017–1026.
- Liu, Y., Gonzalez, M., and Wassgren, C. (2019). Modeling granular material segregation using a combined finite element method and advection-diffusion-segregation equation model. *Powder Tech.*, 346:38–48.
- Lucy, L. B. (1977). A numerical approach to the testing of the fission hypothesis. *The astronomical journal*, 82:1013–1024.
- Lun, C., Savage, S. B., Jeffrey, D., and Chepurniy, N. (1984). Kinetic theories for granular flow: inelastic particles in couette flow and slightly inelastic particles in a general flowfield. *Journal of fluid mechanics*, 140:223–256.
- Makse, H. A. (2000). Grain segregation mechanism in aeolian sand ripples. *The European Physical Journal E*, 1(2-3):127–135.
- Makse, H. A., Havlin, S., King, P. R., and Stanley, H. E. (1997). Spontaneous stratification in granular mixtures. *Nature*, 386(6623):379–382.
- Mangeney, A., Bouchut, F., Thomas, N., Vilotte, J.-P., and Bristeau, M. (2007). Numerical modeling of self-channeling granular flows and of their levee-channel deposits. *Journal of Geophysical Research: Earth Surface*, 112(F2).
- Mangeney, A., Roche, O., Hungr, O., Mangold, N., Faccanoni, G., and Lucas, A. (2010). Erosion and mobility in granular collapse over sloping beds. *Journal of Geophysical Research: Earth Surface*, 115(F3).
- Marks, B., Eriksen, J. A., Dumazer, G., Sandnes, B., and Måløy, K. J. (2017). Size segregation of intruders in perpetual granular avalanches. *Journal of Fluid Mechanics*, 825:502–514.
- Martínez, F. J. (2008). Estudio experimental de flujos granulares densos. Master’s thesis.
- May, L. B., Golick, L. A., Phillips, K. C., Shearer, M., and Daniels, K. E. (2010a). Shear-driven size segregation of granular materials: Modeling and experiment. *Physical Review E*, 81(5):051301.
- May, L. B., Shearer, M., and Daniels, K. E. (2010b). Scalar conservation laws with nonconstant coefficients with application to particle size segregation in granular flow. *Journal of nonlinear science*, 20(6):689–707.
- McCarthy, J. (2009). Turning the corner in segregation. *Powder Technology*, 192(2):137–142.

- Middleton, G. V. (1970). Experimental studies related to problems of flysch sedimentation. *Flysch sedimentology in North America.*, pages 253–272.
- MiDi, G. D. R. (2004). On dense granular flows. *The European Physical Journal E*, 14(4):341–365.
- Mitarai, N. and Nakanishi, H. (2005). Bagnold scaling, density plateau, and kinetic theory analysis of dense granular flow. *Physical review letters*, 94(12):128001.
- Muzzio, F., Goodridge, C., Alexander, A., Arratia, P., Yang, H., Sudah, O., and Mergen, G. (2003). Sampling and characterization of pharmaceutical powders and granular blends. *International Journal of Pharmaceutics*, 250(1):51 – 64.
- Narrow, T., Yoda, M., and Abdel-Khalik, S. (2000). A simple model for the refractive index of sodium iodide aqueous solutions. *Experiments in fluids*, 28(3):282–283.
- Ogawa, S. (1978). Multitemperature theory of granular materials. In *Proc. of the US-Japan Seminar on Continuum Mechanical and Statistical Approaches in the Mechanics of Granular Materials*, 1978, pages 208–217. Gakajutsu Bunken Fukyu-Kai.
- Ohmi, K. and Li, H.-Y. (2000). Particle-tracking velocimetry with new algorithms. *Measurement Science and Technology*, 11(6):603.
- Ottino, J. and Khakhar, D. (2000). Mixing and segregation of granular materials. *Annual Review of Fluid Mechanics*, 32(1):55–91.
- Pane, S. F., Awangga, R. M., Azhari, B. R., and Tartila, G. R. (2019). Rfid-based conveyor belt for improve warehouse operations. *Telkomnika*, 17(2):794–800.
- Park, J. T., Mannheimer, R. J., Grimley, T. A., and Morrow, T. B. (1989). Pipe flow measurements of a transparent non-newtonian slurry.
- Perng, A., Capart, H., and Chou, H. (2006). Granular configurations, motions, and correlations in slow uniform flows driven by an inclined conveyor belt. *Granular Matter*, 8(1):5–17.
- Pierson, T. C. (1986). Flow behavior of channelized debris flows, Mount St. Helens, Washington. In Abrahams, A. D., editor, *Hillslope Processes*, pages 269–296, Winchester, Mass. Allen and Unwin.
- Pouliquen, O. (1999). Scaling laws in granular flows down rough inclined planes. *Physics of fluids*, 11(3):542–548.
- Pouliquen, O., Delour, J., and Savage, S. B. (1997). Fingering in granular flows. *Nature*, 386(6627):816.
- Pouliquen, O. and Vallance, J. (1999). Segregation induced instabilities of granular fronts. *Chaos: An Interdisciplinary Journal of Nonlinear Science*, 9(3):621–630.
- Rocha, F. M., Johnson, C. G., and Gray, J. M. N. T. (2019). Self-channelisation and levee formation in monodisperse granular flows. *J. Fluid Mech.*, 876:591–641.

Bibliography

- Roche, O., Montserrat, S., Niño, Y., and Tamburrino, A. (2008). Experimental observations of water-like behavior of initially fluidized, dam break granular flows and their relevance for the propagation of ash-rich pyroclastic flows. *Journal of Geophysical Research: Solid Earth*, 113(B12).
- Rognon, P. G., Roux, J.-N., Naaïm, M., and Chevoir, F. (2007). Dense flows of bidisperse assemblies of disks down an inclined plane. *Physics of Fluids*, 19(5):058101.
- Rosato, A., Strandburg, K. J., Prinz, F., and Swendsen, R. H. (1987). Why the brazil nuts are on top: Size segregation of particulate matter by shaking. *Physical Review Letters*, 58(10):1038.
- Rousseau, G. and Ancey, C. (2020). Scanning piv of turbulent flows over and through rough porous beds using refractive index matching. *Experiments in Fluids*, 61(8):1–24.
- Russell, A., Johnson, C., Edwards, A., Viroulet, S., Rocha, F., and Gray, J. (2019). Retrogressive failure of a static granular layer on an inclined plane. *Journal of Fluid Mechanics*, 869:313–340.
- Sanvitale, N. and Bowman, E. T. (2012). Internal imaging of saturated granular free-surface flows. *International Journal of Physical Modelling in Geotechnics*, 12(4):129–142.
- Sanvitale, N. and Bowman, E. T. (2016). Using piv to measure granular temperature in saturated unsteady polydisperse granular flows. *Granular Matter*, 18(3):57.
- Sarno, L., Papa, M. N., Villani, P., and Tai, Y.-C. (2016). An optical method for measuring the near-wall volume fraction in granular dispersions. *Granular Matter*, 18(4):80.
- Savage, S. (1998). Analyses of slow high-concentration flows of granular materials. *Journal of Fluid Mechanics*, 377:1–26.
- Savage, S. B. (1979). Gravity flow of cohesionless granular materials in chutes and channels. *Journal of Fluid Mechanics*, 92(1):53–96.
- Savage, S. B. (1984). The mechanics of rapid granular flows. *Advances in applied mechanics*, 24:289–366.
- Savage, S. B. and Hutter, K. (1989). The motion of a finite mass of granular material down a rough incline. *J. Fluid Mech.*, 199:177–215.
- Savage, S. B. and Lun, C. (1988). Particle size segregation in inclined chute flow of dry cohesionless granular solids. *Journal of Fluid Mechanics*, 189:311–335.
- Savage, S. B. and Sayed, M. (1984). Stresses developed by dry cohesionless granular materials sheared in an annular shear cell. *Journal of Fluid Mechanics*, 142:391–430.
- Schaeffer, D. G., Barker, T., Tsuji, D., Gremaud, P., Shearer, M., and Gray, J. M. N. T. (2019). Constitutive relations for compressible granular flow in the inertial regime. *J. Fluid Mech.*, 874:926–951.

- Schlick, C. P., Fan, Y., Umbanhowar, P. B., Ottino, J. M., and Lueptow, R. M. (2015). Granular segregation in circular tumblers: theoretical model and scaling laws. *Journal of Fluid Mechanics*, 765:632–652.
- Schulze, D. (2008). *Powders and Bulk Solids*. Springer Berlin Heidelberg.
- Scott, A. and Bridgwater, J. (1976). Self-diffusion of spherical particles in a simple shear apparatus. *Powder Technology*, 14(1):177–183.
- Seguin, A., Coulais, C., Martinez, F., Bertho, Y., and Gondret, P. (2016). Local rheological measurements in the granular flow around an intruder. *Physical Review E*, 93(1):012904.
- Shinbrot, T. (2004). Granular materials: The brazil nut effect—in reverse. *Nature*, 429(6990):352.
- Silbert, L. E., Ertas, D., Grest, G. S., Halsey, T. C., and Levine, D. (2002). Analogies between granular jamming and the liquid-glass transition. *Phys. Rev. E*, 65:051307.
- Silbert, L. E., Ertas, D., Grest, G. S., Halsey, T. C., Levine, D., and Plimpton, S. J. (2001). Granular flow down an inclined plane: Bagnold scaling and rheology. *Physical Review E*, 64(5):051302.
- Skeel, R. D. and Berzins, M. (1990). A method for the spatial discretization of parabolic equations in one space variable. *SIAM J. Sci. Statist. Comput.*, 11(1):1–32.
- Standish, N., Yu, A., and He, Q. (1991). An experimental study of the packing of a coal heap. *Powder technology*, 68(2):187–193.
- Staron, L. (2018). Rising dynamics and lift effect in dense segregating granular flows. *Physics of Fluids*, 30(12):123303.
- Stephens, D. and Bridgwater, J. (1978a). The mixing and segregation of cohesionless particulate materials part i. failure zone formation. *Powder Technology*, 21(1):17–28.
- Stephens, D. and Bridgwater, J. (1978b). The mixing and segregation of cohesionless particulate materials part ii. microscopic mechanisms for particles differing in size. *Powder Technology*, 21(1):29–44.
- Stoffel, M., Mendlik, T., Schneuwly-Bollschweiler, M., and Gobiet, A. (2014). Possible impacts of climate change on debris-flow activity in the swiss alps. *Climatic Change*, 122(1):141–155.
- Takahashi, T. (1981). Debris flow. *Annual Review of Fluid Mechanics*, 13(1):57–77.
- Thomas, A. and Vriend, N. (2019). Photoelastic study of dense granular free-surface flows. *Physical Review E*, 100(1):012902.
- Thomas, N. (2000). Reverse and intermediate segregation of large beads in dry granular media. *Physical Review E*, 62(1):961.

Bibliography

- Thomas, N. and D'Ortona, U. (2018). Evidence of reverse and intermediate size segregation in dry granular flows down a rough incline. *Physical Review E*, 97(2):022903.
- Thornton, A. and Gray, J. M. N. T. (2008). Breaking size segregation waves and particle recirculation in granular avalanches. *Journal of Fluid Mechanics*, 596:261–284.
- Thornton, A., Weinhart, T., Luding, S., and Bokhove, O. (2012). Modeling of particle size segregation: calibration using the discrete particle method. *International journal of modern physics C*, 23(08):1240014.
- Thornton, A. R., Gray, J. M. N. T., and Hogg, A. (2006). A three-phase mixture theory for particle size segregation in shallow granular free-surface flows. *Journal of Fluid Mechanics*, 550:1–25.
- Timošenko, S. P. and Goodier, J. (1988). *Theory of elasticity*. McGraw-Hill international editions. Engineering mechanics series. McGraw-Hill Book, Auckland, third ed., 23rd print., [international ed.] edition.
- To, K., Lai, P.-Y., and Pak, H. (2001). Jamming of granular flow in a two-dimensional hopper. *Physical review letters*, 86(1):71.
- Trehwela, T., Gray, J. M. N. T., and Ancey, C. (2020a). An experimental scaling law for particle-size segregation in dense granular flows. *Manuscript under review in Journal of Fluid Mechanics*.
- Trehwela, T., Gray, J. M. N. T., and Ancey, C. (2020b). Large particle segregation in sheared dense granular flows. *Manuscript under review in Physical Review Fluids*.
- Tripathi, A. and Khakhar, D. (2011). Rheology of binary granular mixtures in the dense flow regime. *Physics of Fluids*, 23(11):113302.
- Tripathi, A. and Khakhar, D. V. (2013). Density difference-driven segregation in a dense granular flow. *J. Fluid Mech.*, 717:643–669.
- Tsai, J.-C. and Gollub, J. P. (2004). Slowly sheared dense granular flows: Crystallization and nonunique final states. *Physical Review E*, 70(3):031303.
- Tsai, J.-C. and Gollub, J. P. (2005). Granular packings sheared in an annular channel: Flow localization and grain size dependence. *Physical Review E*, 72(5):051304.
- Tunuguntla, D. R., Bokhove, O., and Thornton, A. R. (2014). A mixture theory for size and density segregation in shallow granular free-surface flows. *J. Fluid Mech.*, 749:99–112.
- Tunuguntla, D. R., Thornton, A. R., and Weinhart, T. (2016). From discrete elements to continuum fields: Extension to bidisperse systems. *Computational particle mechanics*, 3(3):349–365.
- Utter, B. and Behringer, R. P. (2004). Self-diffusion in dense granular shear flows. *Phys. Rev. E*, 69:031308.

- Vallance, J. W. and Savage, S. B. (2000). Particle segregation in granular flows down chutes. In *IUTAM Symposium on Segregation in Granular flows*, pages 31–51. Springer.
- van der Vaart, K., Gajjar, P., Epely-Chauvin, G., Andreini, N., Gray, J. M. N. T., and Ancey, C. (2015). Underlying asymmetry within particle size segregation. *Physical Review Letters*, 114(23):238001.
- van der Vaart, K., Thornton, A. R., Johnson, C. G., Weinhart, T., Jing, L., Gajjar, P., Gray, J. M. N. T., and Ancey, C. (2018a). Breaking size-segregation waves and mobility feedback in dense granular avalanches. *Granular Matter*, 20(3):46.
- van der Vaart, K., van Schrojenstein Lantman, M., Weinhart, T., Luding, S., Ancey, C., and Thornton, A. (2018b). Segregation of large particles in dense granular flows suggests a granular saffman effect. *Physical review fluids*, 3(7):074303.
- Vaziri, M., Stott, F., and Spurr, R. (1988). Studies of the friction of polymeric materials. *Wear*, 122(3):313–327.
- Virčíková, E. and Molnar, L. (1992). Recovery of copper from dump slag by a segregation process. *Resources, conservation and recycling*, 6(2):133–138.
- Weinhart, T., Thornton, A. R., Luding, S., and Bokhove, O. (2012). From discrete particles to continuum fields near a boundary. *Granular Matter*, 14(2):289–294.
- Wiederseiner, S., Andreini, N., Epely-Chauvin, G., and Ancey, C. (2011a). Refractive-index and density matching in concentrated particle suspensions: a review. *Experiments in fluids*, 50(5):1183–1206.
- Wiederseiner, S., Andreini, N., Epely-Chauvin, G., Moser, G., Monnereau, M., Gray, J. M. N. T., and Ancey, C. (2011b). Experimental investigation into segregating granular flows down chutes. *Physics of Fluids*, 23(1):013301.
- Williams, J. C. (1976). The segregation of particulate materials. a review. *Powder technology*, 15(2):245–251.
- Williams, S. C. (1968). The mixing of dry powders. *Powder Technol.*, 2:13–20.
- Wills, B. A. (1979). *Mineral Processing Technology*. Pergamon.
- Windows-Yule, C., Seville, J., Ingram, A., and Parker, D. (2020). Positron emission particle tracking of granular flows. *Annual Review of Chemical and Biomolecular Engineering*, 11(1):367–396. PMID: 32228041.
- Woodhouse, M., Thornton, A., Johnson, C., Kokelaar, B., and Gray, J. M. N. T. (2012). Segregation-induced fingering instabilities in granular free-surface flows. *Journal of fluid mechanics*, 709:543–580.

Bibliography

- Xiao, H., Umbanhowar, P. B., Ottino, J. M., and Lueptow, R. M. (2016). Modelling density segregation in flowing bidisperse granular materials. In *Proc. R. Soc. A*, volume 472, page 20150856. The Royal Society.
- Zhu, K., Rao, S. M., Wang, C.-H., and Sundaresan, S. (2003). Electrical capacitance tomography measurements on vertical and inclined pneumatic conveying of granular solids. *Chemical Engineering Science*, 58(18):4225–4245.

Education

- Ph.D. in Mechanics**, École Polytechnique Fédérale de Lausanne (EPFL), Switzerland. October 2020
Thesis title: *Particle-size segregation and rheology coupling in dense granular flows*.
Advisor: Prof. Christophe Ancey.
Perform granular flows experiments. Design of an annular shear cell.
- M.Sc. in Water Resources and Environment** (GPA 6.4/7.0), University of Chile, Chile. January 2015
Civil Engineer (GPA 7.0/7.0), University of Chile, Chile.
Thesis title: *Numerical model for non-Newtonian fluid flow over complex topographies*.
Advisor: Prof. Aldo Tamburrino and Prof. Christian Ihle
Development of an original code for viscoplastic fluid flow.
- B.Eng. in Civil Engineering** (GPA 5.0/7.0), University of Chile, Chile. December 2011
Advisor: Prof. Aldo Tamburrino
Perform experiments on sediment transport and viscoplastic fluids.

Employment history

- École Polytechnique Fédérale de Lausanne, Switzerland (EPFL)** October 2016 - September 2020
Position: Doctoral student.
Responsibilities: Design and operation of experimental setups. Analysis of results. Writing of articles.
Advisor: Prof. Christophe Ancey.
- Advanced Mining Technology Center, University of Chile, Chile** June 2014 - September 2016
Position: Project engineer.
Responsibilities: Numerical modeling and field work leader for snow measurements.
Supervisors: Prof. James McPhee and Dr. Santiago Montserrat
- University of Chile, Chile** March 2016 - July 2016
Position: Lecturer in undergraduate and graduate courses.
Responsibilities: Prepare lectures, coursebooks, exams and evaluations.
Supervisors: Prof. Yarko Niño and Hector Augusto
- University of Chile, Chile** December 2009 - December 2011
Position: Research assistant.
Responsibilities: Experimental assistance to master and doctoral students.
Advisors: Prof. Aldo Tamburrino and Prof. Yarko Niño

Approved research projects

- SNSF Project 200020_175750** December 2017 - November 2020
Title: *Experimental investigation into the coupling between particle segregation and rheology in dense granular flows*
Project leader: Prof. Christophe Ancey
Responsibility: Writing of first draft. Co-designer of an annular shear cell.
- CODEV Seed Money Grant** February 2018 - February 2019
Title: *Monitoring geomorphological changes due to debris flows in mountain rivers using UAV: exploiting*

similarities between Alpine and Andean regions

In collaboration with Dr. Santiago Montserrat, AMTC, University of Chile.

Responsibility: Writing of proposal. Project coordinator and main responsible.

Scientific publications in indexed journals

1. Ancey, C., Bardou, E., Funk, M., Huss, M., Werder, M. A., and **Trewhela, T.** (2019). Hydraulic reconstruction of the 1818 Giétro glacial lake outburst flood. *Water Resources Research*, 55(11), 8840-8863.
2. **Trewhela, T.**, Ihle, C., and Tamburrino, A. (2014). Numerical simulations of comminution slurries over complex topographies: Putting together CFD and pipeline integrity. *Minerals Engineering*, 63, 139-148.

Scientific publications under preparation/revision

1. **Trewhela, T.**, Gray, J. M. N. T., and Ancey, C. (2020). Large particle segregation in sheared dense granular flows. (*under revision in Physical Review Fluids*).
2. **Trewhela, T.**, Ancey, C., and Gray, J. M. N. T. (2020). An experimental scaling law for particle-size segregation in dense granular flows. (*under revision in Journal of Fluid Mechanics*).

Conference presentations (only oral presentations)

1. **Trewhela, T.**, Gray, J. M. N. T., van der Vaart, K., and Ancey C. (2018). Particle size-segregation in granular flows driven by a conveyor belt. *The 12th European Fluid Mechanics Conference. 9-13 September, 2018. Vienna, Austria.*
2. **Trewhela, T.**, Ancey, C., and Gray, J. M. N. T. (2018). Size segregating intruders in oscillating shear cells. *Annual European Rheology Conference. 17-20 April, 2018. Sorrento, Italy.*
3. **Trewhela, T.**, Gray, J. M. N. T., and Ancey C. (2018). Size segregation fluxes in oscillating shear cells. *10th European Solid Mechanics Conference. 2-6 July, 2018. Bologna, Italy.*
4. **Trewhela, T.**, Ihle, C., y Tamburrino, A. (2014). Efecto de la curva de descarga en las características de derrames de fluidos no-Newtonianos sobre topografías reales. *XXVI Congreso Latinoamericano de Hidráulica. 25-29 de Agosto, 2014. Santiago, Chile.*
5. **Trewhela, T.**, Ihle, C., and Tamburrino, A. (2013). Run-out of a non-newtonian fluid over complex topographies due to pipeline leaks. *IBP, Rio Pipeline 2013 Conference and Exposition. 24-26 September, 2013. Rio de Janeiro, Brazil.*

Knowledge transfer events

1. **Colloquium on debris flows monitoring in mountain regions.** 27 November 2018

Chilean government institutions and research agencies were invited to discuss on prospective monitoring and collaboration for debris flow risk assessments. I organized the seminar in collaboration with Dr. Santiago Montserrat.

2. **ICES Annual Meeting** 2017, 2018

Chilean and Swiss researchers were invited to a seminar on climate change and gender equality on research. Invitation was extended to the Chilean Embassy and the Equal Opportunities office of EPFL.

Supervision of students

M.Sc. and B.Sc. students (12)

- | | |
|--|-------------|
| 1. Basil Wietlisbach (1)
<i>Snow reptation monitoring.</i> | Autumn 2018 |
| 2. Gaëtan Gindrat, Stéphane Hartmann, Qazim Llabjani and Mohamed Nadeem (4)
<i>Instrumentation for snow reptation measurements.</i> | Spring 2018 |
| 3. Félix Besson and Daniel Pace (2)
<i>Numerical simulations for the 1818 Giétro disaster.</i> | Spring 2018 |
| 4. Barthélémy Catteau, Vincent Mayoraz and Martin Praz (3)
<i>Dam break numerical simulations.</i> | Autumn 2017 |
| 5. Thibault Roch and Isaac Thury (2)
<i>Algorithm for snow reptation monitoring.</i> | Autumn 2016 |

Internships (2)

- | | |
|--|-------------|
| 1. Valentina Martinez (1)
<i>Orthophoto analysis for geomorphological changes in an Alpine bassin.</i> | Summer 2019 |
| 2. Florian Rein (1)
<i>Design and construction of an experimental setup for levee visualization using refractive index match.</i> | Summer 2019 |

Teaching experience

Lecturer University of Chile, Chile	Autumn 2016
Hydraulic transients, ~10 students, 5 ECTS. Oral lectures, homeworks, and final exam.	1 semester
Project workshop, ~20 students, 3 ECTS. Oral lectures, practical work and final exam.	1 semester
Teaching assistant EPFL, Switzerland	Autumn 2016 - Spring 2020
Hydrological risks, ~20 students, 3 ECTS. Exercise assistance and exam correction.	4 semesters
Fluid mechanics, ~60 students, 5 ECTS. Exercise assistance and exams correction.	4 semesters
Hydraulics, ~20 students, 3 ECTS. Lectures and exams correction.	3 semesters
Teaching assistant University of Chile, Chile	Autumn 2010 - Autumn 2015
Transport phenomena, ~10 students, 3 ECTS. Lectures and project correction.	1 semester
Fluid mechanics, ~80 students, 5 ECTS. Assistant lectures and exams correction.	4 semesters
Hydraulics, ~80 students, 5 ECTS. Lectures and exams correction.	4 semesters
Sediment transport, ~20 students, 5 ECTS. Homework preparation and exam correction.	1 semester
Water quality, ~20 students, 5 ECTS. Laboratory work preparation and exam correction.	3 semesters

Memberships and peer reviewing

Memberships

European Mechanics Society	2018 - 2020
European Geoscience Union	2018, 2020

Article reviewing

Journal of Fluid Mechanics, Physics of Fluids, Experiments in Fluids, Journal of Geophysical Research - Earth Surface, Earth Surface Processes and Landforms, and Earth Surface Dynamics.

Awards and scholarships

Swiss Government Excellence Scholarship 15% retention rate, ~100000 CHF.	2016
CONICYT Doctoral Scholarship 45% retention rate, ~40000 CHF.	2016
CONICYT National Master Scholarship 33% retention rate ~40000 CHF.	2013
Water Resources Division Master Scholarship Awarded for exceptional grades. ~5000 CHF	2012

Personal skills

Languages Spanish (native speaker), English (C1, IELTS Band Score 8.0), German (A1/A2), French (B2).
Programming languages Fortran, C, C++, VisualBasic, Latex, Python.
Softwares HEC-RAS, OpenFOAM, GRASS, QGIS, Phreeqc, Geoclaw, Matlab, Iber.
Operating systems Windows, macOS, Linux (preferred).

Others

Techo para Chile

Leader of 100 volunteers that built houses for the homeless after the 2010 earthquake. March - July 2010
District responsible of 5 Campamentos. 2008-2011
Responsibility: provide financial capacitation to socially vulnerable families.

ICES (Spanish for Chilean Researchers in Switzerland)

Vice-president. 2017 - 2018
Annual Meeting Organizer. 2018